

Synthesis, Crystal Structure and
Performance of Solid Electrolytes for
Lithium and Sodium Solid-State Batteries

by

Parvin Adeli

A thesis
presented to the University of Waterloo
in fulfillment of the
thesis requirement for the degree of
Doctor of Philosophy
in
Chemical Engineering (Nanotechnology)

Waterloo, Ontario, Canada, 2022

© Parvin Adeli 2022

Examining Committee Membership

The following served on the Examining Committee for this thesis. The decision of the Examining Committee is by majority vote.

External Examiner

Mickael Dollé

Professor

Supervisor(s)

Linda F. Nazar

Professor

Internal Member

Yuning Li

Professor

Internal Member

Michael Pope

Associate Professor

Internal-external Member

Vivek Maheshwari

Associate Professor

Author's Declaration

I hereby declare that I am the sole author of this thesis. This is a true copy of the thesis, including any required final revisions, as accepted by examiners.

I understand that my thesis may be made electronically available to the public.

Abstract

The world is realizing the significance of clean energy technologies for green house gas emission reduction. To pave the path to electrification across multiple sectors including transportation, quality energy storage materials must be developed for supplying global market clean energy demands. All-solid-state batteries (ASSBs) have garnered immense attention as a potential avenue for improving the safety and energy density of battery platforms. Large-scale application of ASSBs in electric and hybrid vehicle technologies requires new electrode materials especially solid electrolytes with excellent Li-ion transport properties. This thesis presents an in-depth study of novel solid electrolytes for lithium and sodium solid-state batteries, their crystal structure, and methods to modify their composition and enhance their electrochemical performance. In chapter 1, a brief introduction of batteries and different kinds of solid electrolytes are described in detail. In chapter 2, the various characterization techniques that were applied throughout this thesis are described. In chapter 3, the synthesis, structure, and electrochemical performance of new halide-rich solid solution phases in the argyrodite $\text{Li}_6\text{PS}_5\text{Cl}$ family, $\text{Li}_{6-x}\text{PS}_{5-x}\text{Cl}_{1+x}$, are reported. The limit of the solid solution range, $\text{Li}_{5.5}\text{PS}_{4.5}\text{Cl}_{1.5}$, exhibits quadrupled ionic conductivity (compared to $\text{Li}_6\text{PS}_5\text{Cl}$) of $9.4 \pm 0.1 \text{ mS}\cdot\text{cm}^{-1}$ at room temperature. The ionic conductivity goes up to $12 \text{ mS}\cdot\text{cm}^{-1}$ for sintered materials, approaching the best benchmarks in the field. The structure of single-phase $\text{Li}_{5.5}\text{PS}_{4.5}\text{Cl}_{1.5}$ argyrodite was elucidated by neutron diffraction and refinement results suggest that only one Li ($48h$) site is present, with no Li present on the $24g$ site. In chapter 4, synthesis, and characterization of solid solution series $\text{Li}_6\text{PS}_{5-x}\text{Se}_x\text{Cl}$ electrolytes are discussed. Single crystals of chalcogenohalides were grown and systematically studied via single-crystal X-ray diffraction to understand the effect of Se substitution. Material transport properties were studied via electrochemical impedance spectroscopy and correlated to the underlying structure. In

chapter 5, the synthesis procedure for argyrodites were optimized and novel series of highly conductive sulfide-based compounds, $\text{Li}_{6+2*n-x-m*y}\text{M}_y\text{PS}_{5+n-x}\text{X}_{1+x}$ ($m = 1,2$; $M = \text{Ca, Ga, Al}$) which were prepared by a rapid method are presented. The “super Cl-rich” composition $\text{Li}_{5.35}\text{Ca}_{0.1}\text{PS}_{4.5}\text{Cl}_{1.55}$ was reported for the first time. This material possesses a high room temperature ionic conductivity of 10.2 mS cm^{-1} in the cold-pressed state. Rietveld refinement of the “super Cl-rich” phase was performed against neutron diffraction data and the results show a refined composition of $\text{Li}_{5.36}\text{Ca}_{0.08}\text{PS}_{4.47}\text{Cl}_{1.54}$ that is almost identical to targeted $\text{Li}_{5.35}\text{Ca}_{0.1}\text{PS}_{4.5}\text{Cl}_{1.55}$. Furthermore, an adaptable approach for designing future solid electrolytes is provided. Finally, in chapter 6, novel glassy materials including $\text{LiAl}_{0.33}\text{S}$ ($\sigma = 0.08 \text{ mS.cm}^{-1}$) are presented.

Acknowledgments

I would like to extend my utmost gratitude to my supervisor, Prof. Linda F. Nazar for her continuous guidance, support, and the excellent opportunity to grow as a scientist. It was indeed a life changing experience. I would like to express my sincere gratitude to my PhD committee members: Professors Michael Pope, Vivek Maheshwari and Yuning Li for their valuable time and advice. I am very grateful to my external committee member, Professor Mickael Dollé, for his precious time and insightful comments. I also thank Chem. Eng. Grad. Manager, Ms. Judy Caron.

I would like to thank Dr. Momo Safari, Dr. Robert Black and Dr. Dipan Kundu for their generous help and suggestions at the early stage of my graduate career. I have been very fortunate to work with great collaborators: I thank my coauthors Prof. Gillian Goward and David Bazak for fruitful discussions and their contributions to the NMR part of this research. I also thank Dr. Jalil Assoud, Dr. Ashfia Huq, Dr. Kern-Ho Park, Kavish Kaup, Abhi Shyamsunder, Agnieszka Starobrat for their help with measurements or experiments. I thank my colleagues Ivan Kochetkov and Diane Houtarde for their companionship. I thank *BASF International Scientific Network for Electrochemistry and Batteries* for the financial support and their help with my patent application. A portion of this research used resources at the Spallation Neutron Source, a DOE Office of Science User Facility operated by the *Oak Ridge National Laboratory*.

To my wonderful brothers, Professor Hassan Adeli and Dr. Hossein Adeli: I would have not made it this far without you by my side. I am forever grateful for what you have done for me!

To my amazing parents, Ali and Homa: Words fail to express my gratitude. Thank you for the constant love, care, encouragement, and support. This thesis is dedicated to you!

Table of Contents

Examining Committee Membership.....	ii
Author’s Declaration.....	iii
Abstract.....	iv
Acknowledgments.....	vi
List of Figures.....	xi
List of Tables.....	xix
List of Abbreviations.....	xxiii
Chapter 1 Introduction.....	1
1.1 Overview.....	1
1.2 LIB Electrochemistry.....	2
1.3 Solid State Battery (SSB) and Solid Electrolytes.....	3
1.3.1 Solid-State Battery Challenges.....	5
1.4 Solid Electrolyte Categories (Oxide, Solid Polymer, Sulfide).....	5
1.4.1 Oxides.....	6
1.4.2 Solid Polymer electrolyte (SPE).....	10
1.4.3 Sulfides.....	11
1.5 Argyrodites.....	13
1.6 Mechanism of Ion Transport in Solid Ion Conductors.....	15

1.7 Performance Reporting and Parameters Interplay	16
1.8 Scope of Thesis	17
Chapter 2 Characterization Techniques, Theory and Methods.....	21
2.1 Optical Microscopy (OM) and Scanning Electron Microscopy (SEM)	21
2.2 Energy Dispersive X-ray Analysis.....	22
2.3 Diffraction Techniques	23
2.3.1 Powder X-Ray Diffraction.....	23
2.3.2 Single Crystal X-ray Diffraction.....	25
2.3.3 Neutron Powder Diffraction (NPD).....	25
2.3.4 Synchrotron X-ray Powder Diffraction	26
2.3.5 Rietveld Refinement	26
2.4 Electrochemical Impedance Spectroscopy	28
2.5 Raman Spectroscopy.....	29
Chapter 3 Halide-Rich Lithium Argyrodites	31
3.1 Introduction.....	32
3.2 Material Synthesis and Characterization	35
3.2.1 Electrochemical Impedance Spectroscopy	36
3.2.2 Electrochemical Measurements	37
3.3 Results and Discussion	38
3.4 Conclusion	54

Chapter 4 Chalcogenide Substituted Argyrodites	56
4.1 Introduction.....	57
4.2 Material Synthesis and Characterization	59
4.2.1 Single Crystal Characterization and Structure Refinement	60
4.2.2 Powder X-ray Diffraction	61
4.2.3 Raman Spectroscopy.....	62
4.3 Results and Discussion	63
4.3.1 Structural Properties.....	63
4.3.2 Transport Properties.....	69
4.3.3 ³¹ P MAS-NMR.....	75
4.4 Conclusion	75
Chapter 5 Cation Doped and Dual Modified Argyrodites	77
5.1 Calcium and Other Aliovalent Cation Doped Argyrodites.....	78
5.1.1 Introduction.....	78
5.1.2 Material Synthesis and Characterization	79
5.1.3 Results and Discussion	81
5.1.4 Summary and Conclusion	108
5.2 Sodium Argyrodites	109
5.2.1 Introduction.....	109
5.2.2 Material Synthesis and Characterization	110

5.2.3 Results and Discussion	110
Chapter 6 Discovering New Solid Electrolytes	116
6.1 Li-based System: Li-Al-S Glass	116
6.1.1 Introduction.....	116
6.1.2 Material Synthesis and Results	117
6.2 Na-based Systems: Na-Zr-P-S, Na-Al-P-S and Na-Y-P-S	119
6.2.1 Introduction.....	119
6.2.2 Material Synthesis and Characterization	120
6.2.3 Results and Discussion	123
6.2.4 Summary.....	129
Thesis Perspective.....	130
Future Perspective for the ASSB Field.....	132
References.....	133
Appendix A - Data Use Permissions	146
Appendix B - Supplementary Information for Chapter 5	147
Appendix C - Supplementary Information for Chapter 6	148

List of Figures

Figure 1.1 Schematic illustration of the first Li-ion battery ($\text{LiCoO}_2/\text{Li}^+$ electrolyte/graphite). Reproduced with permission from ACS [3].	2
Figure 1.2 Schematic diagram of an ASSB depicting the working electrode (active material + solid electrolyte + conductive additive), solid electrolyte and counter/reference electrode layers (Li or Li-metal alloy). Modified from [9] with permission from John Wiley and Sons.....	4
Figure 1.3 Reported total ionic conductivity of solid-state lithium-ion conductors at room temperature. Reproduced with permission from ACS [29].	6
Figure 1.4 a) $\text{Na}_3\text{Zr}_2\text{Si}_2\text{PO}_{12}$ phase at 300°C . Black circles denote Na(1) sites and open circles denote Na(2) sites. Na(1) atom can be seen between two Zr octahedra and surrounded octahedrally by the six Na(2) atoms to which wide conduction paths are available. Each Na(2) atom in turn has two Na(1) neighbors, therefore establishing a three-dimensional framework of conduction paths. b) The lantern unit in the NASICON structure [45].	9
Figure 1.5. NASICON structure in rhombohedral symmetry, showing ZrO_6 and $(\text{Si,P})\text{O}_4$ polyhedra. Curved arrow represents the conduction path of Na^+ ions [47]. Reproduced by permission of Royal Society of Chemistry.	10
Figure 1.6 a) Crystal structure of $\text{Li}_6\text{PS}_5\text{X}$ ($\text{X} = \text{Cl, Br, I}$). b) Frank-kasper polyhedra formed from free S^{2-} anions and the corner of PS_4^{3-} tetrahedra. The polyhedra encloses two different Li positions ($48h$ and $24g$). These Li positions form localized cages in which multiple hopping processes are feasible [75]. With permission from ACS Publications.....	14
Figure 1.7 Jump statistics from MD simulations at 450 K for $\text{Li}_6\text{PS}_5\text{Cl}$. The lines represent the three different types of jumps; green for doublet, blue for intracage, and red for intercage. Thicker lines represent larger jump rates. Reproduced with permission from ACS [76].	15

Figure 2.1 The interaction of electron beam with the analyzed sample and the emitted signal from the sample. Secondary electrons generally escape from the depth of approximately 5–50 nm. With permission from Springer. 22

Figure 2.2 *Ray-2* travels an extra path as compared to *Ray-1* (= ABC). The path difference between *Ray-1* and *Ray-2* = ABC = (d Sinθ + d Sinθ) = (2d.Sinθ). For parallel planes of atoms, with a space d_{hkl} between the planes, constructive interference only occurs when Bragg’s law is satisfied. ... 23

Figure 3.1 Rietveld fit of $\text{Li}_{5.5}\text{PS}_{4.5}\text{Cl}_{1.5}$, refined against time-of-flight (TOF) neutron powder diffraction data collected at 298 K (GOF = 3.37, R_{wp} = 4.88%). The black circles denote the observed pattern, and the red solid line indicates the calculated pattern. The difference map is in blue. Calculated positions of the Bragg reflections are represented by the vertical tick marks in green, and the ticks for the minority LiCl phase (1.7 wt%) are shown in pink. 38

Figure 3.2 Crystal structure of $\text{Li}_{5.5}\text{PS}_{4.5}\text{Cl}_{1.5}$ showing the PS_4^{3-} tetrahedra, lithium-ion cages, free $\text{S}^{2-}/\text{Cl}^-$ anions, and comparison of occupancies (SOF) on the 4a and 4c sites between $\text{Li}_6\text{PS}_5\text{Cl}$ (from ref 75) and $\text{Li}_{5.5}\text{PS}_{4.5}\text{Cl}_{1.5}$ 39

Figure 3.3 EDS mapping of the heat-treated $\text{Li}_{5.5}\text{PS}_{4.5}\text{Cl}_{1.5}$ sample, which indicates a homogenous distribution of P, S and Cl at the micron scale. 40

Figure 3.4 XRD patterns of $\text{Li}_{6-x}\text{PS}_{5-x}\text{Cl}_{1+x}$ ($x = 0, 0.25, 0.375$ and 0.55) showing the identified impurities. Calculated positions of the Bragg reflections are represented by the vertical tick marks in green. 42

Figure 3.5 a) Lattice parameter of $\text{Li}_{6-x}\text{PS}_{5-x}\text{Cl}_{1+x}$ vs x showing that Vegard’s law for a solid solution is obeyed; b) room temperature complex impedance plots of the cold-pressed pellets of $\text{Li}_6\text{PS}_5\text{Cl}$, $\text{Li}_{5.75}\text{PS}_{4.75}\text{Cl}_{1.25}$, $\text{Li}_{5.5}\text{PS}_{4.5}\text{Cl}_{1.5}$, and a sintered pellet of $\text{Li}_{5.5}\text{PS}_{4.5}\text{Cl}_{1.5}$ (550°C for 10

min). Inset = magnified view at high frequencies, where the impedance is normalized to the respective pellet thickness (d) for better comparison of different compositions. 44

Figure 3.6 XRD patterns of $\text{Li}_{6-x}\text{PS}_{5-x}\text{Br}_{1+x}$ ($x = 0, 0.5$). $\text{Li}_6\text{PS}_5\text{Br}$ was obtained as pure phase. LiBr impurity peaks are identified with red circles for $\text{Li}_{5.5}\text{PS}_{4.5}\text{Br}_{1.5}$ 44

Figure 3.7 Full temperature range Arrhenius plot for $\text{Li}_{5.5}\text{PS}_{4.5}\text{Cl}_{1.5}$ phase and corresponding Nyquist plot at 195K (inset). The apex frequency is 1.11×10^5 Hz, which corresponds to a capacitance of 1.7×10^{-9} F; the α -value is about 0.9, indicating the ideality of the CPE. 47

Figure 3.8 Conductivity and activation energy (from EIS) for $\text{Li}_{6-x}\text{PS}_{5-x}\text{Cl}_{1+x}$ ($x = 0, 0.25, 0.375$ and 0.5). 48

Figure 3.9 Direct current (DC) polarisation data for electronic conductivity determination for $\text{Li}_{5.5}\text{PS}_{4.5}\text{Cl}_{1.5}$. The DC polarisation curve was fitted with a decay function, and the steady current value at the end of the curve was extrapolated. The electronic conductivity of $3 \times 10^{-9} \text{ S.cm}^{-1}$ was calculated by using Ohm's law. 49

Figure 3.10 Temperature dependence of the ionic conductivity for $x = 0.25$ and $x = 0.375$ 50

Figure 3.11 Arrhenius plots of the diffusivity and conductivity values for $x = 0$ and $x = 0.5$ from PFG and EIS. 52

Figure 3.12 a) Cyclic voltammogram using a $\text{Li}/\text{Li}_{5.5}\text{PS}_{4.5}\text{Cl}_{1.5}/\text{stainless steel}$ cell with a scan rate of 1 mV s^{-1} in the voltage window of $5.0 - 0.1 \text{ V}$. b) Comparison of cyclic voltammogram using $\text{Li}/\text{Li}_{5.5}\text{PS}_{4.5}\text{Cl}_{1.5}/\text{stainless steel}$ (red line) and $\text{Li}/\text{Li}_6\text{PS}_5\text{Cl}/\text{stainless steel}$ (blue line) cells with a scan rate of 1 mV s^{-1} in the voltage window of $5.0 - 0.1 \text{ V}$ 53

Figure 3.13 a) Cyclic voltammogram of a $\text{Li}/\text{SE}/\text{stainless steel}$ cell using $\text{Li}_6\text{PS}_5\text{Cl}$ or $\text{Li}_{5.5}\text{PS}_{4.5}\text{Cl}_{1.5}$ as a solid electrolyte layer with scan rate of 1 mV s^{-1} . The first (solid) and second (dashed) scans are shown. 54

Figure 4.1 a) Lattice parameter of solid solution series $\text{Li}_6\text{PS}_{5-x}\text{Se}_x\text{Cl}$ vs x . The black points represent data extracted from refinement of single crystal X-ray diffraction. The red dotted line denotes the linear fit. b) Se occupancies on Wyckoff 16e site. c) Raman spectra for $x = 0.5, 1, 2$ and 5. $\text{P}(\text{S}_{4-x}\text{Se}_x)^{3-}$ peaks are identified with different colors of dashed lines..... 63

Figure 4.2 a) Crystal structure of $\text{Li}_6\text{PS}_4\text{SeCl}$ obtained from refinement against the single crystal X-ray diffraction data. b) Li cages formed by Li1(48h) (grey) and Li2(48h) (turquoise) sites, Li2(48h) sites introduce a new Li2(48h)-Li2(48h) intercage jump pathway. 64

Figure 4.3 a) Rietveld refinement for $\text{Li}_6\text{PS}_{4.25}\text{Se}_{0.75}\text{Cl}$ refined against synchrotron data. The hollow black circles show the observed pattern, and the red solid line denotes the calculated pattern. The difference map is depicted in blue, and the Bragg reflections are displayed in green. b) XRD pattern (flat stage) of $\text{Li}_6\text{PS}_4\text{SeCl}$. Minority LiCl was observed which is indicated with red triangle. 67

Figure 4.4 XRD pattern (overnight capillary) of $\text{Li}_6\text{PS}_3\text{Se}_2\text{Cl}$ phase. Minority impurity peaks are shown with red triangle (LiCl) and purple stars (not identified). 68

Figure 4.5. XRD pattern (flat stage) of pure $\text{Li}_6\text{PS}_{2.5}\text{Se}_{2.5}\text{Cl}$ phase. 68

Figure 4.6. a) Room temperature (RT) ionic conductivity values for $\text{Li}_6\text{PS}_{5-x}\text{Se}_x\text{Cl}$ ($x = 0, 0.5, 1, 2, 2.5, 4, 5$); b) Impedance plots for ($x = 0.5, 1, 2, 2.5$), inset denotes enlarged view at high frequencies where the RT impedance values are normalized to the cold-pressed pellet thickness; c) Nyquist impedance plot and corresponding fit for $x = 4$ with the respective equivalent circuit. Fit parameters are detailed in **Table 4.4**; d) Nyquist impedance plot and fit for $x = 5$ with the corresponding equivalent circuit. Fit parameters are presented in **Table 4.3**..... 70

Figure 4.7 ^7Li MAS-NMR for $\text{Li}_6\text{PS}_4\text{SeCl}$ and $\text{Li}_6\text{PS}_{2.5}\text{Se}_{2.5}\text{Cl}$ at 25 kHz and 25°C , demonstrating a two-component fit for the former, while the latter is well-fit by a single Gaussian-Lorentzian line shape.	73
Figure 4.8 DC polarization for $x = 1$ material at 0.25, 0.5 and 0.75 V.	74
Figure 4.9 ^{31}P MAS-NMR for the $\text{Li}_6\text{PS}_4\text{SeCl}$ and $\text{Li}_6\text{PS}_{2.5}\text{Se}_{2.5}\text{Cl}$ compositions at 25 kHz and 25°C . The lineshapes exhibit a cascading pattern indicative of differing levels of Se substitution on the PS_4^{3-} tetrahedra, with PS_4^{3-} being the dominant coordination for $x = 1$, whereas $\text{PS}_3\text{Se}^{3-}$ is the most-represented coordination for $x = 2.5$	75
Figure 5.1 XRD (capillary) patterns of ($y = 0, 0.1, 0.15$) and ($x = 0.25, y = 0.1; x = 0.375, y = 0.1$) representing the identified impurities. Vertical tick marks in green represent the calculated positions of the Bragg reflections.	82
Figure 5.2 Rietveld refinement of XRD patterns of a) $\text{Li}_{5.8}\text{Ca}_{0.1}\text{PS}_5\text{Cl}$, GOF = 3.39, $R_{\text{wp}} = 5.95$ (minority Li_3PS_4 phase: 0.9 wt%) b) $\text{Li}_{5.425}\text{Ca}_{0.1}\text{PS}_{4.625}\text{Cl}_{1.375}$, GOF = 5.77, $R_{\text{wp}} = 7.59$ (minority Li_3PO_4 phase: 2.7 wt%). Experimental data are shown in black, calculated data in red and difference profile in blue. Vertical ticks for Bragg reflections are shown in green and minority impurity phases are illustrated in magenta.	83
Figure 5.3 XRD pattern of $y = 0.2$ with illustrated impurity. peaks.	83
Figure 5.4 Time-of-flight (TOF) neutron powder diffraction pattern of the targeted $\text{Li}_{5.7}\text{Ca}_{0.15}\text{PS}_5\text{Cl}$ after heat-treatment at 550°C for 5 h. Ticks for the minority Li_3PO_4 phase (<1.5 wt%) are in purple.	85
Figure 5.5 Raman spectra for (a) $\text{Li}_{5.3}\text{Ca}_{0.1}\text{PS}_{4.5}\text{Cl}_{1.5}$ and (b) $\text{Li}_{5.55}\text{Ga}_{0.15}\text{PS}_5\text{Cl}$ exhibiting the peaks corresponding to PS_4^{3-} moiety.	87

Figure 5.6 TOF neutron powder diffraction pattern of $\text{Li}_{5.55}\text{Ca}_{0.1}\text{PS}_{4.75}\text{Cl}_{1.25}$. Bragg reflections are shown in green; ticks for the minority Li_3PO_4 phase (0.63 wt%) are illustrated in purple. 89

Figure 5.7 TOF neutron powder diffraction pattern of $\text{Li}_{5.35}\text{Ca}_{0.1}\text{PS}_{4.5}\text{Cl}_{1.55}$ after heat-treatment at 550°C for 5 h. Ticks for the minority LiCl phase (0.6 wt%) are in purple. 90

Figure 5.8 XRD pattern of $\text{Li}_{5.45}\text{Al}_{0.1}\text{PS}_{4.75}\text{Cl}_{1.25}$ heat treated at 550°C for 5 h. 92

Figure 5.9 XRD pattern of $\text{Li}_{5.7}\text{Ga}_{0.1}\text{PS}_5\text{Cl}$, $a = 9.8374(1) \text{ \AA}$ obtained from whole pattern fitting. 92

Figure 5.10 Stack plot of ^7Li MAS spectra for the y-series and dual-doped series, demonstrating the strong chlorine-enrichment shift trend, and no major change in chemical shift associated with Ca^{2+} -doping. The inset reveals the secondary peak associated with a Ca^{2+} dopant..... 95

Figure 5.11 SEM images of a) $y = 0.1$ $x = 0$, (550°C , 5 h) and b) of $y = 0.15$ $x = 0$, (550°C , 5 h). 97

Figure 5.12 a) Cyclic voltammogram curve of the stainless steel/ $y = 0.1$ ($x = 0$)/Li cell with scan rate of 1 mV S^{-1} in the voltage window of 5.0 to -0.1 V , inset shows the magnified view in the voltage range of 0.4 to -0.1 V . b) DC polarisation curve for $y = 0.15$ ($x = 0$) at 0.25 V (black), 0.5 V (red), 0.75 V (blue) (cold-pressed at two tons and 300 K). 98

Figure 5.13 a) Nyquist impedance plots of $y = 0, 0.1, 0.15, (x = 0)$ and $y = 0.1, x = 0.5$ at 298 K. Figure inset illustrates the enlarged view at high frequencies. For the sake of easy comparison, the impedance was normalized to the corresponding pellet thickness d (cm); b) 100

Figure 5.14 Temperature dependence of the ionic conductivity for $y = 0.1$ and $y = 0.15$ 101

Figure 5.15 Temperature dependence of the ionic conductivity for $x = 0.25, 0.375, 0.5$ ($y = 0.1$). 101

Figure 5.16 Nyquist plot of $y = 0.15$ at 195 K. The apex frequency is 1.11×10^4 Hz, which corresponds to a capacitance of 1.78×10^{-9} F; the α -value is almost 0.9, indicating the ideality of the CPE. 102

Figure 5.17 Site disorder and lattice parameter vs x for $\text{Li}_{6-x-2y}\text{Ca}_y\text{PS}_{5-x}\text{Cl}_{1+x}$ 107

Figure 5.18 XRD patterns (flat stage) for sample six and sample seven from **Table 5.11**. Solid black line shows observed pattern for targeted $\text{Na}_6\text{PS}_5\text{Cl}$. Na_3PS_4 , NaCl and Na_2S peaks are identified with red circles, blue triangles, and magenta stars, respectively. 112

Figure 5.19 XRD patterns (flat stage) for sample six and sample seven from **Table 5.11**. Solid black line denotes observed pattern for targeted $\text{Na}_{5.5}\text{PS}_{4.5}\text{Cl}_{1.5}$. Na_3PS_4 , NaCl and Na_2S peaks are identified with red circles, blue triangles, and magenta stars, respectively. 112

Figure 5.20 XRD patterns (flat stage) for sample eight and sample nine from **Table 5.11**. Solid black line shows observed pattern for targeted $\text{Na}_5\text{PS}_4\text{Cl}_2$. Na_3PS_4 and NaCl peaks are identified with red circles and blue triangles, respectively. 113

Figure 5.21 XRD patterns (flat stage) for sample three and sample five from **Table 5.12**. Solid black line shows observed pattern for targeted $\text{Li}_{5.72}\text{Na}_{0.03}\text{PS}_{4.75}\text{Cl}_{1.25}$. LiCl and Li_3PO_4 impurity peaks are identified with blue circles and magenta diamonds, respectively. Bragg reflections are shown by the green vertical ticks. 114

Figure 5.22 Impedance plot of the cold-pressed pellet (2 tons) of $\text{Li}_{5.72}\text{Na}_{0.03}\text{PS}_{4.75}\text{Cl}_{1.25}$ at 298 K. Inset denotes magnified view at high frequencies. Impedance was normalized to the pellet thickness (0.640 mm). 115

Figure 6.1 Room temperature Nyquist plots for $\text{LiAl}_{0.33}\text{S}$ glass and heat-treated $\text{LiAl}_{0.33}\text{S}$. Impedance is normalized to the respective pellet thickness for better comparison. Inset displays magnified view at high frequencies. 118

Figure 6.2 Schematic of experimental procedure carried out for Na-Zr-P-S system.	120
Figure 6.3 Heat treatment procedure of targeted $\text{Na}_{1+4x}\text{Zr}_{2-x}(\text{PS}_4)_3$ synthesized from elements.	122
Figure 6.4 Heat treatment procedure of targeted $\text{Na}_{1+4x}\text{Zr}_{2-x}(\text{PS}_4)_3$ synthesized from elements.	123
Figure 6.5 XRD pattern of the synthesized ZrS_2	124
Figure 6.6 XRD pattern of $\text{NaZr}_2(\text{PS}_4)_3$ glass.	125
Figure 6.7 XRD pattern of $\text{Na}_5\text{Zr}(\text{PS}_4)_3$ glass.	125
Figure 6.8 Nyquist plots of the impedance diagram for $\text{Na}_6\text{Zr}_{0.75}(\text{PS}_4)_3$ in the frequency range 100 mHz to 1 MHz. Inset displays magnified view at high frequencies.	126
Figure 6.9 Comparison of ionic conductivities for the $\text{Na}_{1+4x}\text{Zr}_{2-x}(\text{PS}_4)_3$ ($x = 0, 0.5, 1, 1.25$) synthesized glass materials.	127
Figure B.1 Rietveld refinement of XRD pattern of $\text{Li}_{5.3}\text{Ca}_{0.1}\text{PS}_{4.5}\text{Cl}_{1.5}$, GOF = 1.51, Rwp = 8.88.	147
Figure C.1 Comparison of XRD patterns of $\text{Na}_5\text{Zr}(\text{PS}_4)_3$ for three different heat treatment procedures (500°C, hold 10 h; 500°C, hold 4 days and 600°C, hold 11 h).	148

List of Tables

Table 1.1 Ionic conductivity of various oxide solid electrolytes and their activation energies. Temperature reported in the composition column indicates the annealing temperature of the solid electrolyte pellet prior to Li-ion conductivity measurement.....	8
Table 3.1 Atomic coordinates, occupation factor and isotropic displacement parameters of $\text{Li}_{5.5}\text{PS}_{4.5}\text{Cl}_{1.5}$ obtained from Rietveld refinement of neutron TOF data (space group $F43m$), $a = 9.8061(1)$ Å. The composition from the fit is $\text{Li}_{5.47}\text{PS}_{4.55}\text{Cl}_{1.45}$, very close to the nominal.....	39
Table 3.2 EDX analysis of the $\text{Li}_{6-x}\text{PS}_{5-x}\text{Cl}_{1+x}$ ($x = 0, 0.25, 0.5$). Two measurements per sample are represented. The sulfur content was not quantified due to minor hydrolysis that occurs during the sample transfer into the SEM chamber.	41
Table 3.3 Summary of the ionic conductivity (σ_i , for pellets cold-pressed at 2 tons) at 298 K for the synthesized Li-argyrodites. Error in the ionic conductivities is determined from the span in the measurements for multiple samples of the same composition (extracted values of the impedance analyses are tabulated in Table 3.4).	45
Table 3.4 Room temperature resistance values for $\text{Li}_{6-x}\text{PS}_{5-x}\text{Cl}_{1+x}$ (pellets of 1.0 cm diameter) which were obtained from the fit of the real-axis impedance intercept in the Nyquist plot, illustrating the sampling used to derive the standard deviation in the reported conductivities. Nyquist plots for series A are represented in Figure 3.5b	46
Table 3.5 Fitted EIS parameters for $\text{Li}_{5.5}\text{PS}_{4.5}\text{Cl}_{1.5}$ at 195 K ($r_{\text{electrode}} = 0.45$ cm).	48
Table 3.6 Summary of the activation energy (E_a) values obtained from EIS and PFG Arrhenius plots for the synthesized Li-argyrodites.....	50
Table 3.7 Diffusion coefficient of materials compared to halide-rich phase.	52

Table 4.1 Atomic coordinates, occupation factor, and equivalent isotropic displacement parameters of $\text{Li}_6\text{PS}_4\text{SeCl}$ obtained from single-crystal X-ray diffraction data refinement at 280 K (space group $F43m$). The calculated formula is $\text{Li}_{6.12}\text{PS}_4\text{SeCl}$	65
Table 4.2 Atomic coordinates, occupation factor, and equivalent isotropic displacement parameters of $\text{Li}_6\text{PS}_{2.5}\text{Se}_{2.5}\text{Cl}$ obtained from single-crystal X-ray diffraction data refinement at 280 K (space group $F43m$). The calculated formula is $\text{Li}_{5.76}\text{PS}_{2.5}\text{Se}_{2.5}\text{Cl}$	66
Table 4.3 Fit parameters of the impedance data of $\text{Li}_6\text{PSe}_5\text{Cl}$ at room temperature.	71
Table 4.4 Fit parameters of the impedance data of $\text{Li}_6\text{PS}_4\text{SeCl}$ at room temperature.	71
Table 4.5 Li site distribution extracted from ^7Li NMR and refinement of single crystal X-ray diffraction.	74
Table 5.1 Atomic coordinates, occupation factor and isotropic displacement parameters of $\text{Li}_{5.7}\text{Ca}_{0.15}\text{PS}_5\text{Cl}$ obtained from Rietveld refinement of neutron time of flight data (space group $F43m$) $a = 9.8414$ (1) Å, and volume = 953.20 (2) Å ³ yielding a refined composition of $\text{Li}_{5.71}\text{Ca}_{0.15}\text{PS}_{4.95}\text{Cl}$	85
Table 5.2 EDX analysis of the $\text{Li}_{5.8}\text{Ca}_{0.1}\text{PS}_5\text{Cl}$, $\text{Li}_{5.7}\text{Ca}_{0.15}\text{PS}_5\text{Cl}$ and $\text{Li}_{5.3}\text{Ca}_{0.1}\text{PS}_{4.5}\text{Cl}_{1.5}$. Given the slight amount of hydrolysis that takes place during the material transfer into the SEM chamber, the sulfur content could not be accurately quantified. A minimum of 4 measurements per composition is reported.	86
Table 5.3 Atomic coordinates, occupation factor and isotropic displacement parameters of $\text{Li}_{5.55}\text{Ca}_{0.1}\text{PS}_{4.75}\text{Cl}_{1.25}$ obtained from Rietveld refinement of neutron time of flight data (space group $F43m$) $a = 9.8222$ (1) Å, and volume = 947.59 (2) Å ³ . The calculated composition $\text{Li}_{5.56}\text{Ca}_{0.10}\text{PS}_{4.73}\text{Cl}_{1.27}$ is close to the targeted one.	89

Table 5.4 Atomic coordinates, occupation factor and isotropic displacement parameters of $\text{Li}_{5.35}\text{Ca}_{0.1}\text{PS}_{4.5}\text{Cl}_{1.55}$ obtained from Rietveld refinement of neutron time of flight data (space group $F43m$) $a = 9.7898(1) \text{ \AA}$, and volume = $938.24 (3) \text{ \AA}^3$. The calculated composition $\text{Li}_{5.36}\text{Ca}_{0.08}\text{PS}_{4.47}\text{Cl}_{1.54}$ is very close to targeted.....	90
Table 5.5 EDX analysis of the $\text{Li}_{5.7}\text{Ga}_{0.1}\text{PS}_5\text{Cl}$ and $\text{Li}_{5.45}\text{Al}_{0.1}\text{PS}_{4.75}\text{Cl}_{1.25}$. Given the slight amount of hydrolysis that takes place during the material transfer into the SEM chamber, the sulfur content could not be accurately quantified. A minimum of three measurements per composition are reported.	93
Table 5.6 The relative density of the cold-pressed pellets. This value was calculated using the sample geometry and mass compared to the theoretical density of the argyrodite.	96
Table 5.7 Fitted EIS parameters for $y = 0.15$ at 195 K ($r_{\text{electrode}} = 5 \text{ mm}$, $d_{\text{electrode}} = 1.28 \text{ mm}$).	102
Table 5.8 Conductivity (σ at 25 °C, for cold-pressed pellets at 2 ton) and activation energy (E_a) values obtained from EIS and PFG Arrhenius plots for the prepared Ca-argyrodites. See Table 5.9 for analysis details.....	103
Table 5.9 Room temperature resistance values for $\text{Li}_{6-x-2y}\text{Ca}_y\text{PS}_{5-x}\text{Cl}_{1+x}$ (cold-pressed pellets at 2 ton, 10 mm diameter) obtained from the fit of the real-axis impedance intercept in the Nyquist plot. R , d and σ denote resistance, thickness and total conductivity respectively. Samples A , E , G and K are depicted in Figure 5.13a	104
Table 5.10 Room temperature resistance values for $\text{Li}_{6-x-3y}\text{M}_y\text{PS}_{5-x}\text{Cl}_{1+x}$ (cold-pressed pellets at 2 ton, 10 mm diameter) obtained from the fit of the real-axis impedance intercept in the Nyquist plot. R , d and σ denote resistance, thickness, and total conductivity respectively.	105
Table 5.11 Various preparation methods for targeted sodium argyrodites.	111
Table 5.12 Various preparation methods for $\text{Li}_{5.72}\text{Na}_{0.03}\text{PS}_{4.75}\text{Cl}_{1.25}$ phase.	114

Table 6.1 Summary of room temperature ionic conductivities and preparation methods for targeted compositions. HT stands for heat treated..... 128

Table B.1 Atomic coordinates, occupation factor and isotropic displacement parameters of the targeted $\text{Li}_{5.3}\text{Ca}_{0.1}\text{PS}_{4.5}\text{Cl}_{1.5}$ obtained from Rietveld refinement against X-ray diffraction data (space group $F43m$) $a = 9.8132(1) \text{ \AA}$, and volume = $945.02(4) \text{ \AA}^3$. Since X-rays are not able to resolve the Li occupancy, the Occupancies for the $48h$ site were fixed to the nominal values and occupancies for the $4a$ site were fixed to the values obtained from NDP of $\text{Li}_{5.5}\text{PS}_{4.5}\text{Cl}_{1.5}$ 147

List of Abbreviations

- ASSB** - All-Solid-State battery
- ASSLBs** - All-Solid-State Lithium Batteries
- AC** - Alternating Current
- CLS** - Canadian Light Source
- EDX** - Energy-Dispersive X-ray Spectroscopy
- EIS** - Electrochemical Impedance Spectroscopy
- EV** - Electric Vehicle
- GSAS** - General Structure Analysis System
- LATP** - $\text{Li}_{1+x}\text{Al}_x\text{Ti}_{2-x}(\text{PO}_4)_3$
- LGPS** - $\text{Li}_{10}\text{GeP}_2\text{S}_{12}$
- LIB** - Lithium-Ion Battery
- LISICON** - Lithium Superionic Conductor
- LLZO** - $\text{Li}_7\text{La}_3\text{Zr}_2\text{O}_{12}$
- MAS** - Magic Angle Spinning
- MD** - Molecular Dynamic
- NMR** - Nuclear Magnetic Resonance
- NASICON** - sodium (Na) Super Ionic CONductor
- NPD** - Neutron Powder Diffraction
- OEM** - Original Equipment Manufacturer
- OM** - Optical Microscopy
- ORNL** - Oak Ridge National Laboratory
- PFG** - Pulsed Field Gradient
- SEM** - Scanning Electron Microscopy
- SNS** - Spallation Neutron Source

SPE - Solid Polymer Electrolytes

SSB - Solid-State Battery

TOF - Time-of-Flight

XRD - X-Ray Diffraction

ZBH - Zero-Background Holder

Chapter 1 Introduction

1.1 Overview

The rapidly increasing demand for energy storage stems from our technologically driven society. Fulfilling this demand and the progress in the development of portable electronic equipment and devices appeals ever-increasing energy and power density in power sources. Fossil fuel sources are finite, and their combustion has catastrophic impacts on climate change. Greenhouse gas emissions are a preeminent concern in light of global warming. Fluctuation of oil/gas prices, the alarming outcomes of global warming and air pollution have forced us to seek alternative energy storage and conversion systems. Renewable energy sources such as wind, waves and solar energy are being adopted but no one can determine when the sun shines or whether it is a still or windy day therefore power companies seek options to store the electricity obtained from those sources for use when their output falls behind. The intermittent nature of renewable energy sources further emphasizes the importance of energy storage. Batteries can store electrical energy in the form of chemical energy, and they offer portable energy storage.^[1-3]

Rechargeable Li-ion batteries (LIBs) were first commercialized in 1991 by Sony corporation. The developers of the LIBs, M. Stanley Whittingham (first functional rechargeable lithium battery), John B. Goodenough (cobalt oxide cathode), and Akira Yoshino (carbon-based electrodes) were awarded the Nobel Prize in chemistry in 2019. LIBs enable storing energy from renewable resources and are currently used in many applications ranging from small portable electronic devices such as phones, laptops and digital cameras to large power systems such as hybrid electric vehicles (HEVs), plug-in hybrid electric vehicles (PHEVs) and electric vehicles (EVs).

1.2 LIB Electrochemistry

A battery is an assembly of interconnected electrochemical cells tailored towards a specific application. Each cell consists of a positive electrode (cathode), a negative electrode (anode), and an ionically conductive media (electrolyte) between the electrodes. The ionic species travel through the electrolyte between anode and cathode while the electrons travel through the external circuit. For the purpose of this thesis, the terms battery and cell are used interchangeably. **Figure**

1.1 illustrates a schematic of the first LIB in which below reactions occur:

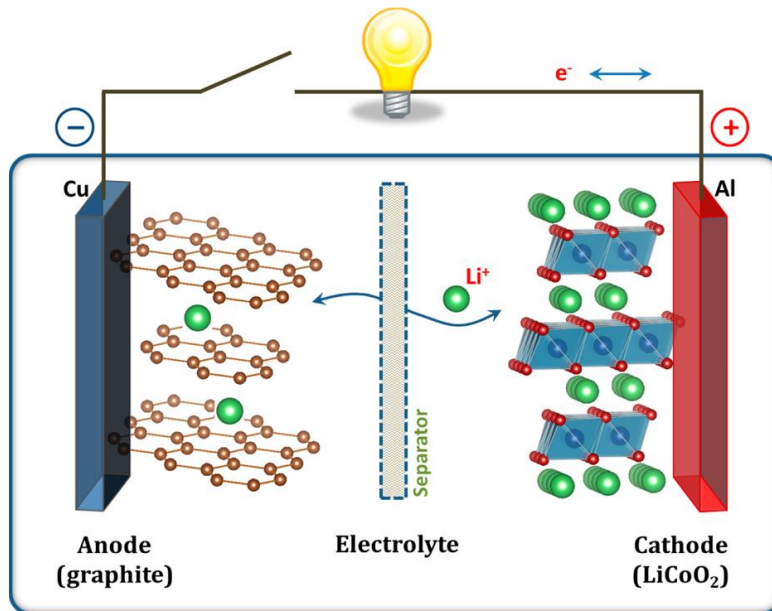
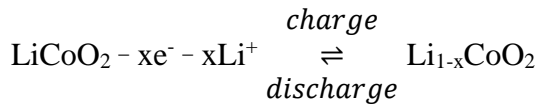
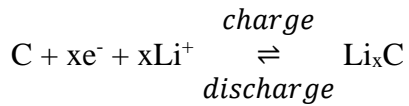


Figure 1.1 Schematic illustration of the first Li-ion battery ($\text{LiCoO}_2/\text{Li}^+$ electrolyte/graphite). Reproduced with permission from ACS [3].

This cell rendered an energy density of 150 Wh kg^{-1} vs today's Li-ion systems which deliver $\sim 260 \text{ Wh kg}^{-1}$. Current day LIBs implement a following generation of LiCoO_2 (LCO) cathode such as $\text{LiNi}_{1-x}\text{M}_x\text{O}_2$ ($\text{M} = \text{Co}, \text{Mn}$ and Al). Other promising cathode materials include but are not limited to $\text{Li}_{1+x}\text{M}_{1-x}\text{O}_2$ ($\text{M} = \text{Co}, \text{Mn}$ and Ni) layered oxide, $\text{LiNi}_{0.5}\text{Mn}_{1.5}\text{O}_4$ spinel oxide and LiVPO_4F polyanionic compounds.^[4] The current common anode material employed for LIBS is graphite with the capacity of 372 mAhg^{-1} . Silicon offers a much higher theoretical capacity of 4200 mAh.g^{-1} but suffers from volume expansion during lithiation. Lithium metal as the negative electrode offers large gravimetric capacity of 3862 mAhg^{-1} along with the low redox potential of -3.04 V vs. the standard hydrogen electrode.^[5]

LIBs have dominated the market due to their advantages. LIBs do not suffer from the memory effect that takes place in nickel-cadmium or nickel-hydride batteries.^[6] They offer a lightweight design, possess higher volumetric and gravimetric energy storage capabilities and lower self-discharge than comparable battery technologies. However, they also have drawbacks such as aging and capacity deterioration which require further improvement.^[3] The most significant challenge for Li rechargeable batteries progress is safety.

1.3 Solid State Battery (SSB) and Solid Electrolytes

The automotive market is considered as the biggest rising opportunity for LIBs in future. One option for decreasing the current anthropogenic global warming particularly those associated with the transportation sector is using battery electric vehicles (BEVs). BEVs offer a means of integrating renewable energy into the transportation sector while significantly reducing emissions compared to gasoline vehicles. However, enlarged battery size required for automotive propulsion exacerbates the safety issues of current Li-ion batteries, therefore, potential mass market for electric and hybrid vehicle technologies demands continued improvement in the safety of battery

platforms to be successful. Lithium all-solid-state batteries (ASSB) are a notable potential avenue for improving both safety and energy density.^[7,8] Schematic diagram of a bulk-type ASSB is displayed in **Figure 1.2**.^[9] ASSBs can also be fabricated in thin films which are employed in microelectronics applications such as implantable medical devices.

One reason Li-ASSB are attracting keen interest is that they could enable the use of a Li metal anode resulting in enhanced energy density. Another reason is that the flammable organic electrolyte used in a conventional Li-ion cell is replaced with a leakage-free, non-flammable solid-electrolyte posing fewer safety concerns. Significant incidents of Li-ion battery fires were caused by ignition of the organic liquid electrolyte.^[10,11] Implementation of solid-electrolyte also benefits from less stringent packaging demands (leading to higher volumetric energy density) and permits transfer of Li ions exclusively, consequently avoiding concentration gradients observed in liquid electrolytes.^[12,13] Furthermore, solid electrolytes possess a comparatively wider electrochemical stability window.

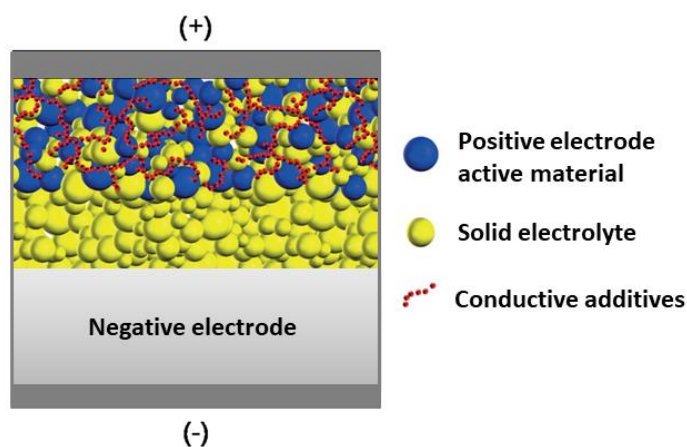


Figure 1.2 Schematic diagram of an ASSB depicting the working electrode (active material + solid electrolyte + conductive additive), solid electrolyte and counter/reference electrode layers (Li or Li-metal alloy). Modified from [9] with permission from John Wiley and Sons.

1.3.1 Solid-State Battery Challenges

Despite these putative advantages for ASSB, there is a long way to large-scale commercialization due to the challenges and materials issues that still remain to be addressed. Contact losses in the composite cathode and degradation at the interface between cathode active material and solid electrolyte interface are among these challenges. Various approaches are applied to form a favourable interface between electrode and electrolyte such as coating active material particles with solid electrolyte thin film (via pulsed laser deposition) or heating a mixture of active material and glass solid electrolyte (where applicable) to T_g followed by supercooling. The latter approach allows the supercooled glass to stick to the active material particles, enhancing the electrode-electrolyte contact area.^[14]

One main challenge which is the focus of this thesis lies in the development of solid electrolytes with high Li^+ ion conductivity at room temperature who also exhibit good electrochemical stability and electrochemical performance. This subject has motivated the emerging R&D efforts for new material families that can compete with the performance of current liquid electrolytes.^[15]

1.4 Solid Electrolyte Categories (Oxide, Solid Polymer, Sulfide)

Extensive research has been dedicated to finding a wide range of solid electrolytes leading to the development of Li-ion conducting oxides, borohydride materials;^[16] solid polymer electrolytes (SPE);^[17] and sulfides as shown in **Figure 1.3**. Some of these electrolytes are explained in more detail in the following subsections.

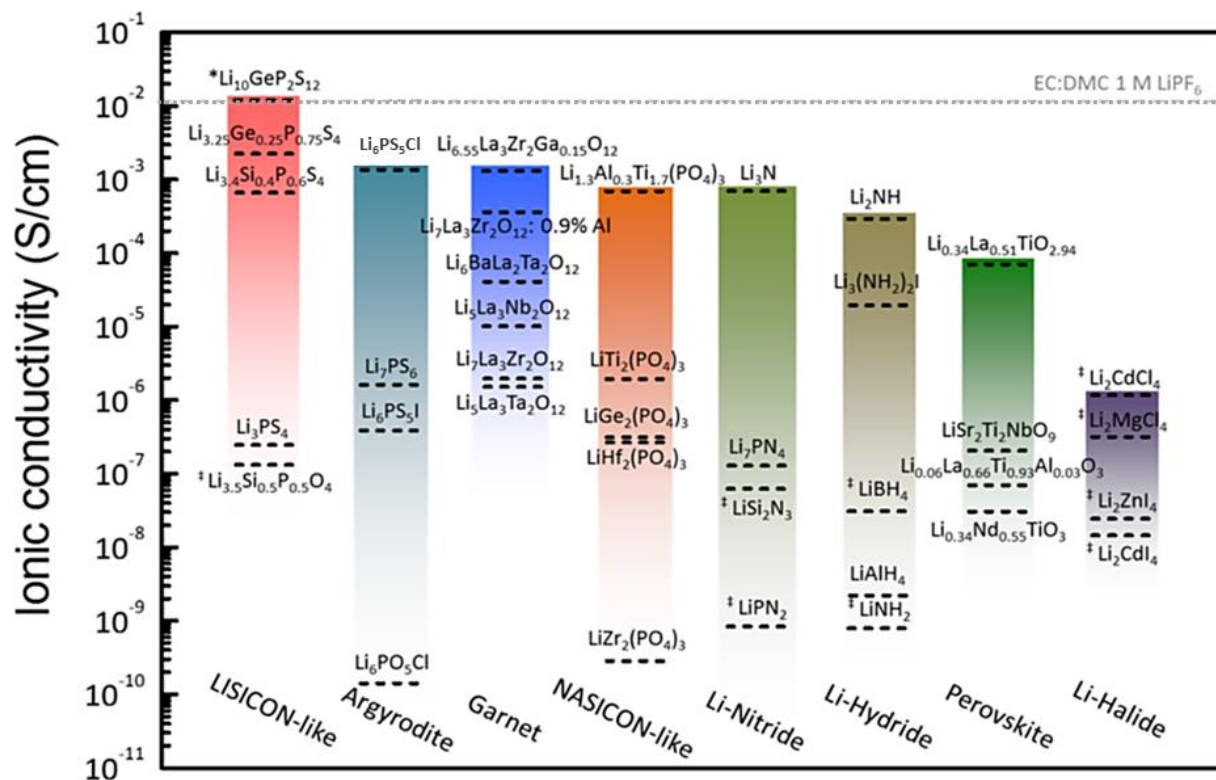


Figure 1.3 Reported total ionic conductivity of solid-state lithium-ion conductors at room temperature. Reproduced with permission from ACS [29].

1.4.1 Oxides

Oxides are more stable in air compared to sulfides but have the detriment of hardness and very low ductility which leads to high interfacial resistances. They usually require high temperature sintering and have high-cost precursors.^[18] Oxides include LISICON;^[19] perovskites,^[20] antiperovskites,^[21] garnets,^[22] and NASICON^[23] families.

In 1978, H. Hong discovered $Li_{14}Zn(GeO_4)_4$ for the first time with the Pnma space group (determined by single crystal X-ray analysis) and reported the ionic conductivity of 1×10^{-4} mS.cm⁻¹. He named the structure LISICON which stands for **Li** super**ionic** **con**ductor. This solid electrolyte is not stable against metallic lithium.^[24,25]

Perovskite structure is represented by the general formula ABO_3 with $Pm\bar{3}m$ space group. Aliovalent doping in the A site has been practiced in this structure and among the studied compositions, $Li_{0.34}La_{0.56}TiO_3$ exhibited the highest Li-ion conductivity (σ_{bulk} : $1.53 \text{ mS}\cdot\text{cm}^{-1}$ at 300 K, $E_a = 0.33 \text{ eV}$).^[26]

Metal oxides in the ideal garnet structure have the general formula $A_3B_2(XO_4)_3$ with Li ions occupying the X-sites or tetrahedral sites. Room temperature ionic conductivity can be enhanced by introducing more Li into the structure. Weppner *et al.* reported garnet-related structures $Li_5La_3M_2O_{12}$ (M: Nb, Ta) and $Li_6BaLa_2Ta_2O_{12}$. The latter exhibits an ionic conductivity of $0.4 \text{ mS}\cdot\text{cm}^{-1}$ (at 295K).^[27] Later, $Li_7La_3Zr_2O_{12}$ (LLZO) and its substituted versions (e.g. $Li_{6.75}La_3Zr_{1.75}Ta_{0.25}O_{12}$) became an attractive and promising subject for several studies owing to their relatively higher ionic conductivity (**Table 1.1**) and chemical stability.^[28,29] Al and Si co-doping also has a positive impact on the total ionic conductivity of LLZO due to amorphous species present at the grain boundaries.^[30] Substitution of Ga^{3+} for Li^+ in $Li_7La_3Zr_2O_{12}$ stabilizes a cubic structure in the space group $I\bar{4}3d$. In the cubic modifications of LLZO structure ($Ia\bar{3}d$ and $I\bar{4}3d$), Li-ions are disordered on the tetrahedral and octahedral sites vs. ordered in the tetragonal structure (space group $I4_1/acd$). Therefore, this substitution ($Li_{7-3x}Ga_xLa_3Zr_2O_{12}$) notably enhanced the ionic conduction, and the corresponding Li-ion transport has been extensively investigated by NMR methods.^[31-36]

Table 1.1 Ionic conductivity of various oxide solid electrolytes and their activation energies. Temperature reported in the composition column indicates the annealing temperature of the solid electrolyte pellet prior to Li-ion conductivity measurement.

Composition (nominal formula)	Conductivity (mS.cm ⁻¹)	T (°C)	E _a	Ref
Li ₇ La ₃ Zr ₂ O ₁₂ (980°C, tetragonal)	0.002	27	0.54	37
Li ₇ La ₃ Zr ₂ O ₁₂ (1230°C, cubic)	0.30	25	0.31	28
Li ₇ La ₃ Zr ₂ O ₁₂ (1125°C, 1.7 wt% Al, 0.1 wt% Si)	0.68	25	-	30
Li ₇ La ₃ Zr _{1.89} Al _{0.15} O ₁₂ (1150°C)	0.34	25	0.33	38
Li _{6.55} La ₃ Zr ₂ Ga _{0.15} O ₁₂ (1085°C)	1.3	24	0.3	31
Li _{1.07} Al _{0.69} Ti _{1.46} (PO ₄) ₃ (950°C)	1.3	25	0.33	39
Li _{1.5} Al _{0.5} Ge _{1.5} (PO ₄) ₃ (560°C, glass-ceramic)	0.4	25	0.37	40

NASICON - sodium (Na) Super Ionic CONductor

NASICON stands for sodium (Na) Super Ionic CONductor. Li_{1+x}Al_xTi_{2-x}(PO₄)₃ (LATP) and Li_{1+x}Al_xGe_{2-x}(PO₄)₃ (LAGP) possess NASICON structure.^[41] Compared to Li₁₄Zn(GeO₄)₄, LATP electrolyte exhibits a better ionic conductivity (**Table 1.1**) but similar to Li₁₄Zn(GeO₄)₄ and Li_{0.5-3x}La_{0.5+x}TiO₃, it is unstable with metallic lithium due to facile Ti⁴⁺ reduction. NASICON compounds with the general formula Na_{1+x}Zr₂Si_xP_{3-x}O₁₂, 0 < x < 3 are among the best tridimensional oxide ionic conductors.^[42] Their composition is derived from NaZr₂P₃O₁₂ by partial replacement of P by Si with Na excess to balance the negatively charged framework to yield the general formula Na_{1+x}Zr₂Si_xP_{3-x}O₁₂. This compound exhibits a rhombohedral crystal structure with space group R3c for all compositions, except in the range 1.8 ≤ x ≤ 2.2 where the structure is monoclinic in the space group C2/c. The conductivity is reported to be high for a phase with

monoclinic crystal lattice attaining maximum at $x = 2$.^[43,44] $\text{Na}_3\text{Zr}_2\text{Si}_2\text{PO}_{12}$ was primarily developed by Hong and Goodenough in 1975.

As shown in **Figure 1.4**, the structural framework of NASICON can be simplified into basic groups of two ZrO_6 octahedra separated by three phosphorous/silicon tetrahedra (PO_4 and SiO_4) with which they share corner oxygen. These primary units $2\text{ZrO}_6\text{-}3(\text{P/Si})\text{O}_4$ are called the lantern units in NASICON structure. They connect by additional corner sharing, that leads to a three-dimensional framework through which this material exhibits fast ion mobility.^[44,45] Sodium ions are spread within the conduction channels with three equilibrium positions as follows:

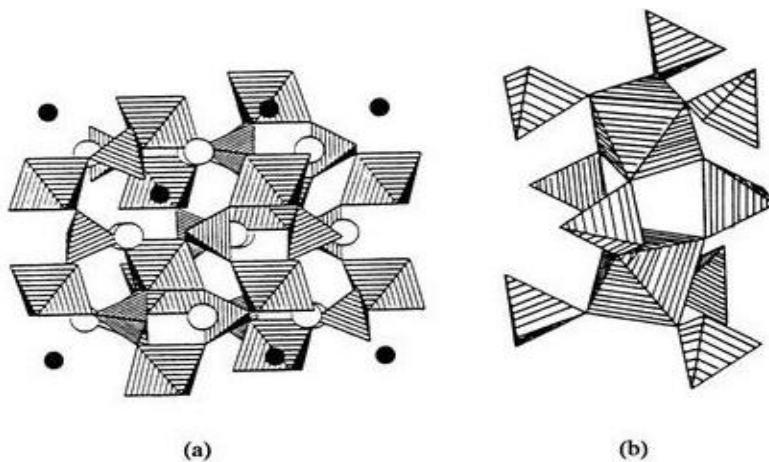


Figure 1.4 a) $\text{Na}_3\text{Zr}_2\text{Si}_2\text{PO}_{12}$ phase at 300°C . Black circles denote Na(1) sites and open circles denote Na(2) sites. Na(1) atom can be seen between two Zr octahedra and surrounded octahedrally by the six Na(2) atoms to which wide conduction paths are available. Each Na(2) atom in turn has two Na(1) neighbors, therefore establishing a three-dimensional framework of conduction paths. b) The lantern unit in the NASICON structure [45].

- 1) Na (1) sites with distorted octahedral coordination, which are situated between two ZrO_6 octahedra along the c axis to produce ribbons of $\text{O}_3\text{ZrO}_3\text{NaO}_3\text{ZrO}_3$. There is one Na (1) per unit formula.
- 2) Na (2) at each bends of the zigzag path in a loose polyhedron with ten neighboring oxygens. Three Na (2) positions exist per unit formula.

- 3) Mid-Na that are just in between Na (1) and Na (2) sites. Six mid-Na positions exist per unit formula in a five-fold coordinated polyhedron.

Evidently, all positions cannot be occupied simultaneously. There are at most four Na ions per unit formula within the conduction channels. In the monoclinic phase, only 20% of the Na (1) positions are populated. The conducting channels in NASICON are of a zigzag shape as represented in **Figure 1.5**.^[46,47] NASICON compounds possess ionic conductivities up to $10^{-3} \text{ S}\cdot\text{cm}^{-1}$.^[48] Gordon *et al.* have reported on a solid-state route for synthesis of $\text{Na}_3\text{Zr}_2\text{Si}_2\text{PO}_{12}$ at temperatures above 1200°C . However, the high temperature reactions introduce unwanted secondary phases such as monoclinic zirconia.^[44]

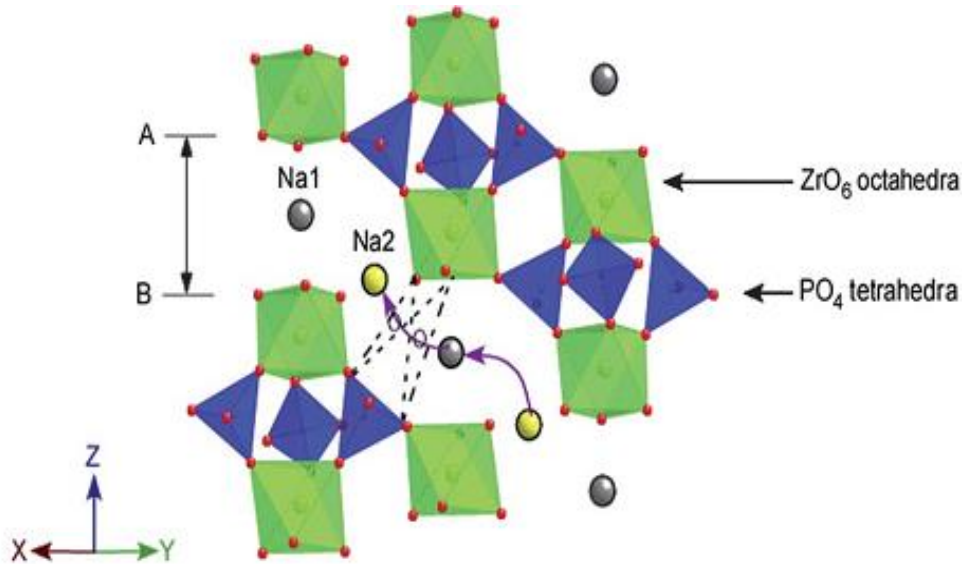


Figure 1.5. NASICON structure in rhombohedral symmetry, showing ZrO_6 and $(\text{Si,P})\text{O}_4$ polyhedra. Curved arrow represents the conduction path of Na^+ ions [47]. Reproduced by permission of Royal Society of Chemistry.

1.4.2 Solid Polymer electrolyte (SPE)

Solid polymer electrolytes (SPE) can be categorized into three groups: dry SPEs, polymer-in-salt electrolytes and single-ion conducting polymer electrolytes. SPEs are soft, operable with Li metal, and can accommodate volume changes of the electrodes during the charge-discharge

process. On the downside, they exhibit low ionic conductivities in the range of 10^{-8} - 10^{-6} S.cm⁻¹ at room temperature due to the restricted local polymer chain motion. In order to enhance the ionic conductivity, inorganic fillers are employed into SPEs.^[17,49,50]

1.4.3 Sulfides

Sulfides encompass a wide range of glassy, glass-ceramic, and ceramic materials. Some of the well-known sulfides include: Li₂S-P₂S₅,^[51] Li_{3.25}Ge_{0.25}P_{0.75}S₄,^[52] Li₇P₃S₁₁,^[53] Li₁₀GeP₂S₁₂,^[54] Li_{9.54}Si_{1.74}P_{1.44}S_{11.7}Cl_{0.3},^[55] and Li-argyrodites.^[56] Sulfides offer high ionic conductivity, and they can be readily consolidated into membranes, which is a crucial factor for making good contact between solid particles for cold-pressed pellets, with no sintering necessary. This also leads to lower electrode-electrolyte interfacial resistance in the ASSB fabrication. Sulfides' drawback is that they should be handled in an inert atmosphere as they are prone to decomposition in the presence of moisture. H₂S gas is generated upon hydrolysis of sulfides by water molecules in air. Investigations of air stability for Li₂S-P₂S₅ glasses revealed that the amount of H₂S generated relies heavily on the glass composition.^[57]

Glassy sulfide ion conductors date back to the 1980s. Several glassy systems were studied in-depth as potential solid electrolytes. Some of those systems are as follow: Li₂S-SiS₂ ($\sigma = 0.1$ mS.cm⁻¹),^[58] Li₂S-SiS₂-LiX (when X = I, $\sigma = 0.7$ - 1.32 mS.cm⁻¹ and when X = Cl, $\sigma = 0.3$ mS.cm⁻¹),^[59] SiS₂-P₂S₅-Li₂S-LiI ($\sigma = 2.1$ mS.cm⁻¹),^[60] Li₂S.P₂S₅.LiI ($\sigma = 1$ mS.cm⁻¹),^[61] Li₂S.GeS₂ ($\sigma = 0.04$ mS.cm⁻¹),^[62] B₂S₃-Li₂S ($\sigma = 0.006$ - 0.03 mS.cm⁻¹),^[63] and B₂S₃-P₂S₅-Li₂S ($\sigma = 0.08$ - 0.1 mS.cm⁻¹).^[63] The room temperature ionic conductivity in the parentheses correspond to the specific compositions reported in each paper.

Glass-ceramics or crystallized glass electrolytes are obtained by heat treatment of an amorphous mixture of mechanically milled precursors at the temperature range of 150 - 300°C. In 2005, Tatsumisago *et al.* developed glass-ceramic $\text{Li}_7\text{P}_3\text{S}_{11}$ by ball milling Li_2S (70 mol%) and P_2S_5 (30 mol%) mixture for 20 h at 370 rpm followed by heat treatment at 240°C for 2 h. The resulting glass-ceramic showed an ionic conductivity of $3.2 \text{ mS}\cdot\text{cm}^{-1}$ at room temperature.^[53] Another example is glass-ceramic Li_3PS_4 obtained by milling the precursors for 10 h at 500 rpm followed by heat treatment at 243°C for 1 h ($\sigma = 1 \text{ mS}\cdot\text{cm}^{-1}$ at 30°C).^[64]

Compared to glass-ceramics, crystalline/ceramic electrolytes are synthesized at a higher temperature range. The premier crystalline sulfide ion conductor, $\text{Li}_{3.25}\text{Ge}_{0.25}\text{P}_{0.75}\text{S}_4$, was developed in 2001 with a reported ionic conductivity of $2.2 \text{ mS}\cdot\text{cm}^{-1}$ at room temperature and was labelled as thio-LISICON. Thio denotes replacing the oxide ions with the more polarizable S^{2-} ions. This results in higher ionic conductivity in the sulfide analogue.^[52] In 2011, $\text{Li}_{10}\text{GeP}_2\text{S}_{12}$ (LGPS) structure was developed by Kanno *et al.* and has the space group (number 137) $\text{P4}_2/\text{nmc}$. LGPS exhibits a superb ionic conductivity of $12 \text{ mS}\cdot\text{cm}^{-1}$ at 300 K comparable to those observed in liquid electrolytes in commercial Li-ion batteries (**Figure 1.3**).^[54] The attractive ionic conductivity of LGPS is overshadowed by high-cost precursor, limited electrochemical stability window and poor interface stability with metallic lithium as demonstrated by computational and experimental studies. Further research into cheaper alternative precursors revealed that the Sn analogue of LGPS which possesses a larger cell volume exhibits only 1/3 of the ionic conductivity ($\sigma_{\text{total}} = 4 \text{ mS}\cdot\text{cm}^{-1}$) due to a higher grain boundary resistance and the Si analogue with a smaller unit cell exhibits $2.3 \text{ mS}\cdot\text{cm}^{-1}$.^[65,66] In 2016, Kanno *et al.* introduced two other new ionic conductors: $\text{Li}_{9.54}\text{Si}_{1.74}\text{P}_{1.44}\text{S}_{11.7}\text{Cl}_{0.3}$ with the marvelous ionic conductivity of $25 \text{ mS}\cdot\text{cm}^{-1}$ and (off-stoichiometric) $\text{Li}_{9.6}\text{P}_3\text{S}_{12}$ exhibiting ionic conductivity of $1.2 \text{ mS}\cdot\text{cm}^{-1}$ at room temperature.^[55]

1.5 Argyrodites

Li-argyrodites are particularly promising candidates for ASSB due to their ease of preparation, comparatively inexpensive precursors, ductility, high ionic conductivities, and reported electrochemical stability.^[67] These advantages have led researchers to employ Li-argyrodite as a promising solid electrolyte with various cathode and anode materials in several innovative ASSB cells.^[68-72]

The argyrodite family spans a wide general composition $A_{(12-n-x)/m}^{m+} B^{n+} L_{6-x}^{2-} M_x^-$ ($A = \text{Ag}^+, \text{Cu}^+, \text{Li}^+$ etc.; $B = \text{Ga}^{3+}, \text{Si}^{4+}, \text{P}^{5+}$; $L = \text{S}, \text{Se}, \text{Te}$; and $M = \text{Cl}, \text{Br}, \text{I}$).^[73] Within this range, Li_7PS_6 , crystallizes in two different high temperature and low temperature phases. Symmetry lowers from cubic to orthorhombic upon formation of the low temperature phase. Partial substitution of the sulfide ions in Li_7PS_6 argyrodite with halides results in the cubic high temperature phase to be stabilized at room temperature: $\text{Li}_6\text{PS}_5\text{X}$ ($X = \text{Cl}, \text{Br}, \text{I}$) were developed in 2008 by Deiseroth *et al.* and has the cubic space group $F\bar{4}3m$ with the space group number 216.^[56,74]

$\text{Li}_6\text{PS}_5\text{X}$ structure is comprised of PS_4^{3-} tetrahedra and isolated S^{2-}/X^- and Li^+ ions in the lattice (unit cell shown in **Figure 1.6a**).^[56,75] There are two possible crystallographic sites for Li^+ ions: Wyckoff $48h$ and $24g$. The latter site serves as an intermediate state through which Li^+ ions can diffuse. The Li sites form localized cages, and each cage hosts twelve $48h$ sites, half of which are occupied. These cages are named Frank-Kasper polyhedra, within and between which various Li^+ -ion jumps are feasible, namely: intracage ($48h$ - $48h$) hops, doublet hops ($48h$ - $24g$ - $48h$) and intercage hops (**Figure 1.6b**).^[75] These three possible jumps build up the 3D diffusion pathway through the crystal. Intercage jumps dominate the macroscopic long-range Li^+ -ion transport and determine the conductivity due to being the slowest jump. Molecular dynamic (MD) simulations

by Wagemaker's group has demonstrated the low jump rate of inter-cage jumps represented in **Figure 1.7**.^[76] Line thickness shows the jump rate quantity.

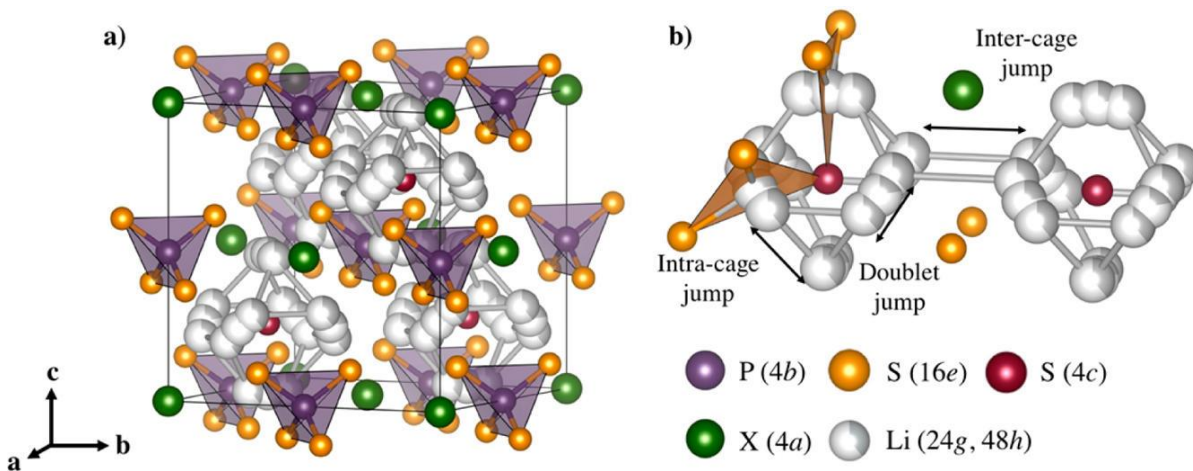


Figure 1.6 a) Crystal structure of $\text{Li}_6\text{PS}_5\text{X}$ (X = Cl, Br, I). b) Frank-kasper polyhedra formed from free S^{2-} anions and the corner of PS_4^{3-} tetrahedra. The polyhedra encloses two different Li positions (48h and 24g). These Li positions form localized cages in which multiple hopping processes are feasible [75]. With permission from ACS Publications.

$\text{Li}_6\text{PS}_5\text{Cl}$ and $\text{Li}_6\text{PS}_5\text{Br}$ phases exhibit fast ion conductivity where S^{2-} and X^- are disordered on two crystallographic positions (4a, 4c) in the cubic lattice. On the other hand, $\text{Li}_6\text{PS}_5\text{I}$ with no S^{2-}/X^- disorder (due to the larger ionic radius of I⁻) shows higher activation energies for Li^+ ion diffusion and lower ionic conductivity ($4.6 \times 10^{-4} \text{ mS}\cdot\text{cm}^{-1}$).^[86,87] This is in accord with prior studies of Deiseroth *et al.*, who observed a two-step narrowing behavior in the Li NMR line-shapes for $\text{Li}_6\text{PS}_5\text{I}$ that suggested a more confined motion.^[56]

The common synthesis method for argyrodites is mechanical milling followed by heat treatment. Adams *et al.* showed that heat treatments above 250°C are necessary on the ball milled precursors in order to achieve a good ionic conductivity for Li₆PS₅Cl argyrodite at room temperature. [69]

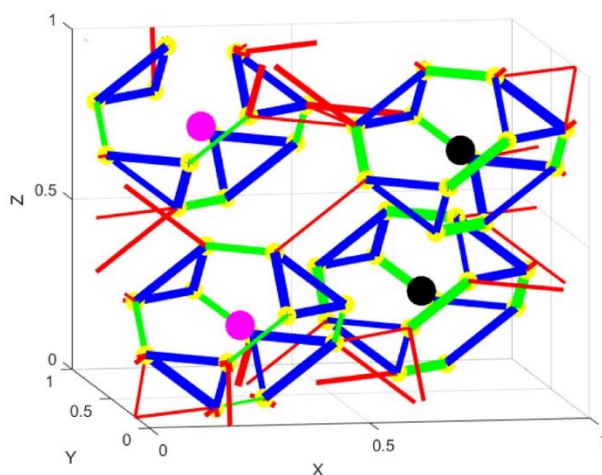


Figure 1.7 Jump statistics from MD simulations at 450 K for Li₆PS₅Cl. The lines represent the three different types of jumps; green for doublet, blue for intracage, and red for intercage. Thicker lines represent larger jump rates. Reproduced with permission from ACS [76].

1.6 Mechanism of Ion Transport in Solid Ion Conductors

In conventional liquid electrolytes, solvated Li-ions migrate in the solvent medium in a flat potential energy profile. On the other hand, in crystalline solid electrolytes, Li-ions jump from one Li site to another empty Li site in the structure along the minimum energy pathway. This jump process is governed by the energy barrier for the jump between the two local minima. Aside from the energy barrier, the ionic conductivity is contingent on the number of vacancies and partial occupancies in the lattice as well as having an open framework and long-range connectivity of Li sites. Therefore, the underlying crystal structure has a direct impact on the overall ionic conductivity. Conductivity can be expressed as:

$$\sigma = \frac{A}{T} n_c \exp\left[-\frac{E_a}{k_b T}\right]$$

Where T represents temperature, A is a constant corresponding to the crystal-structure, n_c denotes carrier concentration, E_a represents activation energy for ion transport and k_b is the Boltzmann constant.^[18] According to this formula, one strategy for improving conductivity is aliovalent doping or substitution for introducing additional carriers. A larger number of mobile ions enhances the conductivity but there is usually an optimum point after which the conductivity decreases. Aside from experimental studies, simulation techniques have been utilized in depth for investigation of diffusion mechanisms in sulfide superionic conductors.^[77] Ab Initio Molecular Dynamic (AIMD) simulations for superionic conductors show that several Li ions diffuse simultaneously via concerted mechanism as opposed to single-ion migration observed in typical solids.^[78]

1.7 Performance Reporting and Parameters Interplay

Considerable effort has gone into developing solid electrolytes that are up to par in performance vis a vis commercial liquid electrolytes. It is essential to note that when comparing reported Li-ion conductivities of solid electrolytes in various groups, one should keep multiple factors in mind that could have impacted the reported measurement. To this point, an accurate description of methodology and measurement conditions is required to make a sound comparison. For example, regarding ionic conductivity, one should pay attention to whether the material has been sintered and at what pressure/exact temperature the measurement was performed. It has been observed that increasing pressure can impact the ionic conductivity to a certain point that the density saturates.^[79] For $\text{Li}_6\text{PS}_5\text{Cl}$, an improved ionic conductivity of $5 \text{ mS}\cdot\text{cm}^{-1}$ at 26°C was recently reported but this value was achieved after direct long-term annealing and upon application

of very high pressure (i.e., eight tons).^[80] Aside from the fact that sintering may not be feasible due to low decomposition temperatures, from a cost perspective in industrial manufacturing, it is not favorable to hot press the solid electrolytes for cell applications.

1.8 Scope of Thesis

This thesis presents an in-depth study of novel lithium and potential sodium solid electrolytes for solid-state batteries (SSBs), their crystal structure, methods to modify their composition, mechanical properties, and methods to enhance their electrochemical performance. This thesis serves as a steppingstone in the path of breaking the material-related barriers that eclipse the all-solid-state battery commercialization path. In chapter 1, a brief introduction of batteries and different kinds of electrolytes is provided. In chapter 2, characterization techniques that were applied throughout this thesis are detailed.

In chapter 3, the synthesis, structure, and electrochemical performance of new halide-rich solid solution phases in the argyrodite $\text{Li}_6\text{PS}_5\text{Cl}$ family, $\text{Li}_{6-x}\text{PS}_{5-x}\text{Cl}_{1+x}$, are reported. Electrochemical impedance spectroscopy and neutron diffraction were combined to determine that increasing the Cl/S^{2-} ratio has a systematic, and exceptional influence on Li-ion mobility in the lattice. The limit of solid solution series was determined to be $\text{Li}_{5.5}\text{PS}_{4.5}\text{Cl}_{1.5}$ which has a low activation energy (E_a) of 0.29 ± 0.01 eV and exhibits an ionic conductivity of 9.4 ± 0.1 $\text{mS}\cdot\text{cm}^{-1}$ at 298 K in a cold-pressed state. This is almost four-fold greater than $\text{Li}_6\text{PS}_5\text{Cl}$ ($\sigma = 2.5 \pm 0.1$ $\text{mS}\cdot\text{cm}^{-1}$) prepared under identical processing conditions. The sintered $\text{Li}_{5.5}\text{PS}_{4.5}\text{Cl}_{1.5}$ phase exhibits even higher conductivity of 12.0 ± 0.2 $\text{mS}\cdot\text{cm}^{-1}$. Substitution of divalent S^{2-} for monovalent Cl^- weakens interactions between the mobile Li-ions and surrounding framework anions. Weakened interactions play a key role in enhancing performance, along with increased site disorder and

higher lithium vacancy population. This work provides guidance for realizing future highly conductive and ductile solid electrolytes and has been published:

Parvin Adeli, J. David Bazak, Kern Ho Park, Ivan Kochetkov, Ashfia Huq, Gillian R. Goward, and Linda F. Nazar. Boosting solid-state diffusivity and conductivity in lithium superionic argyrodites by halide substitution, *Angew. Chem. Int. Ed.* 58, 2019, 8681-8686.

The design optimization of solid electrolytes is critical to realize the practical deployment of ASSBs. One of the structural families that have garnered immense interest as solid electrolytes for foundational studies of ASSBs is Li-argyrodites. In chapter 4, single crystals of chalcogenohalides with cubic argyrodite structure were grown and systematically studied via single-crystal X-ray diffraction to understand the effect of Se substitution in the solid solution series $\text{Li}_6\text{PS}_{5-x}\text{Se}_x\text{Cl}$. Transport properties were investigated via electrochemical impedance spectroscopy and correlated to the underlying structure. Within the explored compositional space, $\text{Li}_6\text{PS}_4\text{SeCl}$ exhibited the highest ionic conductivity of $4.7 \text{ mS}\cdot\text{cm}^{-1}$. Furthermore, the cascading effect of Se substitution indicative of differing levels of substitution on the PS_4^{3-} tetrahedra was elucidated via Raman spectroscopy. This work provides insight on structure-property relationships of selenide-based argyrodite phases which offer an excellent platform for understanding and designing future superionic solid electrolytes. The interplay between the amount of dopant, the number of Li sites and the ensuing impact on the ion transport is a fundamental aspect that can also inform rational design in other promising solid electrolyte families. The manuscript for this work is close to submission:

Parvin Adeli, J. David Bazak, Jalil Assoud, Abhi Shyamsunder, Gillian R. Goward, and Linda F. Nazar. Correlating structural changes and transport properties in chalcogenide substituted Li-argyrodite superionic conductors, 2022.

In chapter 5, the synthesis method for argyrodite-based solid electrolytes was optimized and simplified. A novel array of compounds in the Li-argyrodite family ($\text{Li}_{6-2y}\text{Ca}_y\text{PS}_5\text{Cl}$, $\text{Li}_{6-x-2y}\text{Ca}_y\text{PS}_{5-x}\text{Cl}_{1+x}$, $\text{Li}_{6.1-x-2y}\text{Ca}_y\text{PS}_{5.05-x}\text{Cl}_{1+x}$ and $\text{Li}_{6-x-3y}\text{M}_y\text{PS}_{5-x}\text{Cl}_{1+x}$ (M: Al or Ga)) were introduced with the advantage of a rapid preparation technique and their behaviour as solid electrolytes was monitored through substitution of an aliovalent cation for Li^+ and increasing the Cl^- content. Furthermore, the underlying principles governing fast ion conduction and diffusion in these classes of materials are put forward. ASSB employing thiophosphates often operate with cold-pressed pellets, hence it is essential that a solid electrolyte exhibits high conductivity prior to sintering. The novel super Cl-rich composition $\text{Li}_{5.35}\text{Ca}_{0.1}\text{PS}_{4.5}\text{Cl}_{1.55}$ was reported which possesses a high room temperature ionic conductivity of 10.2 mS cm^{-1} in the cold-pressed state as a promising solid electrolyte candidate for Li-ASSB. The efficacy of aliovalent cation doping in this class of superionic argyrodites was demonstrated as a means of increasing the vacancy population and thereby boosting their performance. This work has been patented:

Parvin Adeli, Linda F. Nazar, Zhizhen Zhang, *Lithium ion conducting solid materials*, filed with number EU 20169037.7 on April 9th, 2020, (Applicant/Proprietor: BASF SE, University of Waterloo).

and the corresponding manuscript was published:

Parvin Adeli, J. David Bazak, Ashfia Huq, Gillian R. Goward, and Linda F. Nazar. Influence of aliovalent cation substitution and mechanical compression on Li-ion conductivity and diffusivity in argyrodite solid electrolytes, *Chem. Mater.* 33, 2021, 146-157.

Sodium's lower cost and natural abundance have prompted researchers to pursue the sodium analogues of lithium-based solid ionic conductors which exhibit attractive ionic conductivity for application in practical sodium solid-state batteries. Feasibility of Na-argyrodites was investigated and is presented in the last section of chapter 5. It was observed that Cl substitution in Na_7PS_6 does not positively impact synthesizability. Additionally, formation of stable competing phases such as Na_3PS_4 in lieu of the targeted $\text{Na}_{7-x}\text{PS}_{6-x}\text{Cl}_x$ ($x = 1, 1.5, 2$) is discussed. In light of the experimental efforts indicating full substitution of lithium for sodium in argyrodites is not possible, a small amount of Na doping was attempted with simultaneous halogen doping in the anion site. The pure single-phase $\text{Li}_{5.72}\text{Na}_{0.03}\text{PS}_{4.75}\text{Cl}_{1.25}$ was synthesized. This composition was characterized by impedance spectroscopy and exhibited an ionic conductivity of $5.4 \text{ mS}\cdot\text{cm}^{-1}$.

In chapter 6, several glass material systems that were investigated are briefly discussed. Among the studied materials, $\text{LiAl}_{0.33}\text{S}$ exhibited the highest ionic conductivity ($\sigma = 0.08 \text{ mS}\cdot\text{cm}^{-1}$) at 298 K. Additionally, sodium glassy materials were prepared as potential solid electrolytes for Na-SSBs such as $\text{Na}_{1+4x}\text{Zr}_{2-x}(\text{PS}_4)_3$ and $\text{Na}_{1+4x+y}\text{Al}_y\text{Zr}_{2-x-y}(\text{PS}_4)_3$ phases. However, these glass phases did not exhibit promising ionic conductivities.

Chapter 2 Characterization Techniques, Theory and Methods

2.1 Optical Microscopy (OM) and Scanning Electron Microscopy (SEM)

A light microscope or an optical microscope uses visible light to give a magnified view of an object and the modern ones possess a maximum magnification of around 1000x.^[81] In this thesis, Wild Heerbrugg M5A OM was implemented to observe and select single crystals of the argyrodite samples. The colorless air-sensitive argyrodite crystals were placed on a glass slide inside the glovebox and protected by Paratone-N oil before transferring to the OM sample stage for picking out a crystal for single crystal X-ray diffraction.

Scanning electron microscopy is an important multipurpose imaging technique applied to obtain information regarding the morphology (shape and size), topological characteristics (texture, roughness) of micro and nano structured materials and their chemical composition. A Scanning electron microscope scans a focused electron beam over the sample surface to produce an image. High energy electrons are accelerated from the source to bombard the sample surface (penetrating depth of a few microns) as a result of which secondary electrons, backscattered electrons, characteristic X-rays and visible light (cathodoluminescence) are generated (**Figure 2.1**). The interaction volume of electrons with the sample and scattering of the electrons is contingent on the atomic number, concentration of atoms and the accelerating voltage. During the measurement backscattered and secondary electrons are commonly applied, and the SEM chamber is held under vacuum.^[82] Air sensitive argyrodite samples were mounted on a SEM stub using carbon tape then

sealed under argon in a container. During the transfer from the container to the SEM chamber, the samples were exposed to air for 30 seconds.

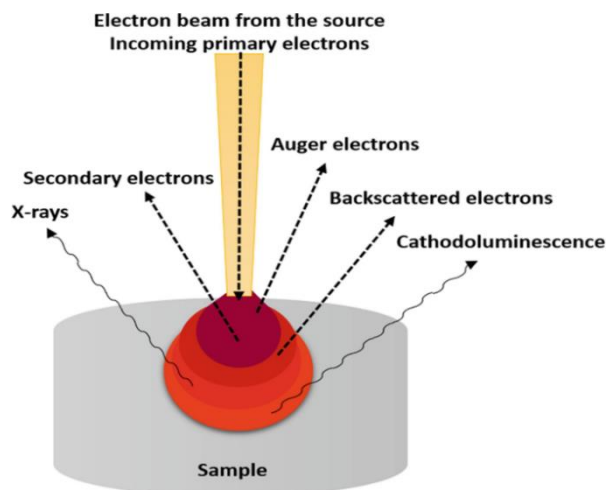


Figure 2.1 The interaction of electron beam with the analyzed sample and the emitted signal from the sample. Secondary electrons generally escape from the depth of approximately 5–50 nm. With permission from Springer.

2.2 Energy Dispersive X-ray Analysis

Energy Dispersive X-ray (EDX) analysis is an analytical technique implemented in conjunction with SEM for the elemental analysis or chemical characterization of the studied sample. When the SEM electron beam hits the sample surface, electrons are ejected from the atoms. Subsequently, electrons from higher states fall to compensate for the holes caused by ejected electrons and characteristic X-ray is emitted. EDX analysis relies on the fact that each element possesses a unique set of peaks on its emission spectrum. This technique is not applicable for detection of light elements.

For halide-rich phases in chapter 3 and anion substituted argyrodites in chapter 4, elemental mapping of the materials was performed with an FEI Quanta Feg 250 ESEM (environmental

scanning electron microscope) equipped with an EDX spectroscopy detector. For the Ca chapter, Zeiss Leo 1530 FESEM (with EDX detector) was utilized for microstructure observation of the samples as well as elemental analysis. All the EDX measurements were carried out using an acceleration voltage of 15 kV, with an acquisition time of 60 s. The studied argyrodite materials were not stable under prolonged electron beam illumination.

2.3 Diffraction Techniques

2.3.1 Powder X-Ray Diffraction

Electromagnetic radiation can be diffracted when its wavelength is of the same order as the grating. Crystal structures have a typical interatomic spacing of 1 - 3 Å which allows them to act as three-dimensional diffraction gratings for X-ray wavelength. Therefore, X-Ray diffraction (XRD) is a great method for studying the crystalline materials. XRD data analysis gives valuable information such as differentiating between crystalline and amorphous materials, identification of unknown

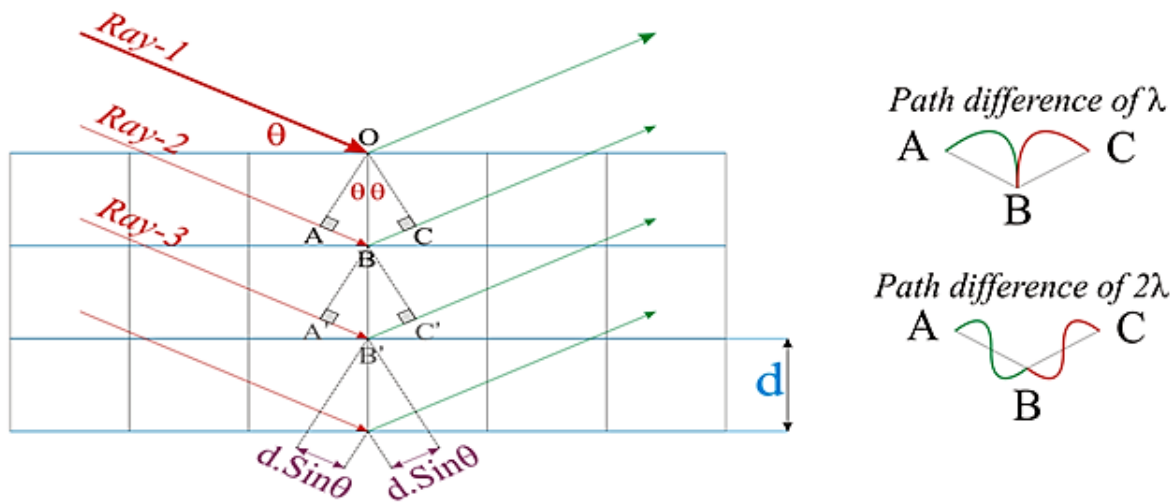


Figure 2.2 Ray-2 travels an extra path as compared to Ray-1 (= ABC). The path difference between Ray-1 and Ray-2 = ABC = ($d \sin\theta + d \sin\theta$) = ($2d \cdot \sin\theta$). For parallel planes of atoms, with a space d_{hkl} between the planes, constructive interference only occurs when Bragg's law is satisfied.

crystalline materials, sample purity, unit cell parameters etc. A fine powder material contains many crystals located at random angles. Certain crystals happen to be oriented so that the x-ray beam, the crystal and the detector satisfy Bragg's law. This causes constructive interference at specific detector angles and diffraction can occur. **Figure 2.2** geometrically illustrates the Bragg's law.

$$\text{Bragg's law: } n\lambda = 2d \sin\theta \quad (\text{Equation 2.1})$$

It is important to have a sufficient number of crystals to have an even distribution at all possible crystal orientations. During a scan, the detector is rotated over a range of angles to detect bands of diffracted x-rays produced by the correctly aligned crystals.^[83]

The concept of reflection from lattice planes merely assists in imagining what occurs in a diffraction experiment while in fact, X-rays are scattered by the atom's electron density. The oscillating electric field of X-rays imposes the same oscillation frequency on the impacted electrons (charged particles) which causes the electron to radiate the scattered X-rays in every direction forming a spherical wave. The net scattered amplitude is determined by the interference of the spherical waves upon going from one single scattering centre to a periodic distribution of scattering centres. The data recorded in XRD is the intensity distribution of scattered radiation as a function of scattering angle.^[84]

The X-rays are produced in an evacuated tube similar to a cathode ray tube. An applied current heats up a tungsten filament which liberates electrons. The liberated electrons are accelerated by a high voltage and hit a copper target where copper x-rays are generated. The x-rays exit the tube and irradiate the sample from which they are diffracted into a detector. The output diffractograms contain three pieces of information that can be used to extract information:

- 1) peak positions (i.e., 2θ values or d-spacings) – unit cell parameters
- 2) peak shapes – crystal size and strain

3) peak intensities – abundance of a material in a mixture, symmetry, space group

For the argyrodite materials, the air sensitive products were ground, loaded and sealed under argon in a 0.3 mm diameter quartz capillary to protect them from ambient air. The XRD patterns were obtained at room temperature over the range of 10° to 90° using Cu $K\alpha$ radiation on PANalytical Empyrean X-ray diffractometer equipped with a PIXcel bidimensional detector. The applied voltage and current were 45 kV and 40 mA respectively. Patterns were recorded in Debye-Scherrer geometry. Prior to running a capillary, samples were scanned for 20 min on flat stage while the sample was being protected under Kapton film. Patterns were recorded in Debye-Scherrer geometry using a parabolic X-ray mirror in the incident beam optics. HighScore Plus software was used to identify the peaks.

2.3.2 Single Crystal X-ray Diffraction

The data was collected on a BRUKER KAPPA diffractometer equipped with a SMART APEX II CCD applying graphite-monochromated Mo- $K\alpha$ radiation. During the measurement, the single crystals were protected by liquid N_2 flow using an OXFORD Cryostream controller 700 at 280 K.

2.3.3 Neutron Powder Diffraction (NPD)

The disadvantage of X-rays is that they do not interact strongly with light elements. Contrary to X-rays, neutrons are scattered by the nuclei as opposed to the electrons. For time-of-flight (TOF) neutron powder diffraction (NPD) measurements, argyrodite samples (1.5 gram) were loaded into a vanadium can, sealed with a copper gasket and aluminum lid in an argon-filled glovebox. NPD data were collected at room temperature on POWGEN at the Spallation Neutron Source (SNS) at the Oak Ridge National Laboratory (center wavelength 1.5\AA , d-spacing range $0.50097 - 13.0087\text{\AA}$).

2.3.4 Synchrotron X-ray Powder Diffraction

Synchrotron XRD provides better resolution and better signal:noise ratio compared to laboratory XRD. For synchrotron measurement, powder sample of $\text{Li}_6\text{PS}_{4.25}\text{Se}_{0.75}\text{Cl}$ was loaded into a 0.3 mm diameter and 0.01 mm wall thickness capillary and sealed with epoxy inside the gloved box under argon. The sample was measured at the Canadian Light Source (CLS) with a wavelength of 0.68954 Å (~18 keV).

2.3.5 Rietveld Refinement

Hugo Rietveld was a crystallographer who developed the Rietveld method in 1960s for neutron diffraction. Later in the 1970s, this method was applied to X-ray diffraction as well. Rietveld structure refinement is a technique that estimates the intensities of Bragg peaks in a powder diffraction pattern under the constraints dictated by a known or assumed space group. This method starts from a structural model of the unit cell and compares the calculated diffraction pattern with the measured pattern point by point. Afterwards, the calculated parameters (atomic coordinates, displacement parameters) are modified by using the least square method in order to achieve a better fit.^[84] The true intensity of Bragg peaks is the area under the peak which is called the integrated intensity. The calculated integrated intensity is demonstrated as below:

$$I_{hkl} = K \times p_{hkl} \times L_{\theta} \times P_{\theta} \times A_{\theta} \times T_{hkl} \times |F_{hkl}|^2 \quad (\text{Equation 2.2})$$

In this equation, K is the scale factor which is a constant for a given phase. This factor is needed to normalize the experimental integrated intensities with calculated ones. In order to achieve the best fit in the refinement, it's significant that the K value is correct. p_{hkl} is the multiplicity factor which is a function of symmetry and represents the number of symmetrically similar points in the reciprocal lattice. L_{θ} is the Lorentz multiplier which comprises of two distinct geometrical

dependent components. The subscript θ implies being a function of the Bragg angle. \mathbf{P}_θ is the polarisation factor representing the partial polarisation of the scattered electromagnetic wave. \mathbf{A}_θ is the absorption factor which changes based on the geometry and specimen properties and accounts for absorption of incident and diffracted beams. \mathbf{T}_{hkl} is the preferred orientation factor which addresses the deviations from a completely random distribution of grain orientations. Last but not least is the structure factor, $|\mathbf{F}_{hkl}|^2$ which is the square of the absolute value of structure amplitude, \mathbf{F}_{hkl} . The structure factor has information on the types (f), locations (u, v, w) and distribution of atoms in a unit cell.^[85] \mathbf{F}_{hkl} is a complex number:

$$\mathbf{F}_{hkl} = \sum_{j=1}^n \mathbf{g}^j \mathbf{t}^j \left(\frac{\sin \theta}{\lambda} \right) \mathbf{f}^j \left(\frac{\sin \theta}{\lambda} \right) \exp[2\pi i(hx^j + ky^j + lz^j)] \quad (\text{Equation 2.3})$$

Where n represents the total number of atoms (including symmetrically equivalent atoms) in the unit cell. \mathbf{g}^j is the occupation of site j thus in the case of full occupancy, \mathbf{g}^j equals one, \mathbf{t}^j is the atomic displacement factor (representing displacements caused by thermal motion¹ etc.), $\mathbf{f}^j \left(\frac{\sin \theta}{\lambda} \right)$ is the atomic scattering factor which in the case of neutron as the incident beam is not a function of $\frac{\sin \theta}{\lambda}$ and (x^j, y^j, z^j) shows the fractional coordinate triplet of the corresponding atom j in the unit cell.

The outcome of the Rietveld refinement should be sensible from physical and chemical aspects. There are parameters to assess the reliability of the refined pattern/least square fits after running the refinement and to check how close Y_j^{obs} (observed intensity) and Y_j^{cal} (calculated intensity) are. Common parameters are goodness of fit:

¹ continuous oscillating motion of atoms above absolute zero

$$\chi^2 = \frac{\sum_{j=1}^n w_j (Y_j^{obs} - Y_j^{cal})^2}{n-p} \quad (\text{Equation 2.4})$$

And

$$R_{wp} = \left[\frac{\sum_{j=1}^n w_j (Y_j^{obs} - Y_j^{cal})^2}{\sum_{j=1}^n (Y_j^{obs})^2} \right]^{\frac{1}{2}} \times 100\% \quad (\text{Equation 2.5})$$

Where n is the total number of points measured in the powder pattern, and w_j is the weight of the data point j and p is the number of free least squares parameters.

In this thesis, Rietveld refinements of the X-ray, neutron and synchrotron powder diffraction data were carried out using the GSAS II (General Structure Analysis System) software which was developed by A.C. Larson and R.B. Von Dreele.

2.4 Electrochemical Impedance Spectroscopy

Impedance is a measure of the ability of a circuit to resist the flow of electrical current. In electrochemical impedance spectroscopy (EIS) analysis, a small alternating current (AC) potential is applied to an electrochemical cell and the current response is measured. The AC voltage is usually applied as a sinusoidal excitation over a frequency range and the AC current response is analyzed as a sum of sinusoidal functions. The excitation signal represented as a function of time can be written as: $E_t = E_0 \sin(\omega t)$ where E_0 is the amplitude of the signal. The relationship between the system properties and response to periodic voltage excitation is very complex in the time domain. Fourier transformation facilitates simplifying of signals from time domain to frequency domain. In the frequency domain voltage/current relations can be reorganized to an ohm's law similar: $I(j\omega) = V(j\omega)/Z(j\omega)$

$$Z(\omega) = Z_0 \exp(j\phi) = Z_0 (\cos\phi + j \sin\phi) \quad (\text{Equation 2.6})$$

Therefore, the impedance can be described by a complex value consisting of a real part and an imaginary part at each frequency measured. Because of this ohm's law like relationship between complex current and voltage, the impedance of a circuit with multiple elements is calculated implementing the same rules as with multiple resistors, which simplifies calculations to a great extent.

Nyquist plots used in this proposal are plotted with imaginary part of the resistance on y-axis and real part on x-axis. In this thesis, EIS measurements on solid electrolytes were carried out on a VMP3 potentiostat/galvanostat station with EIS/Z capabilities (Bio-Logic Science Instruments). The DC voltage was kept at open-circuit voltage and the AC voltage of 100 or 200 mV in amplitude was applied with a frequency of 100 mHz to 1 MHz. Low frequency data are on the right side of the plot and higher frequencies are on the left. Temperature dependent conductivity measurements were carried out from negative temperatures up to 150°C. The specific temperature window for individual samples is mentioned in each chapter. The complex impedance plots are analyzed by fitting with different equivalent circuits, to obtain the resistance and capacitance of different arcs at different temperatures. The conductivity is calculated by converting the resistance to the conductivity, considering sample geometry as shown in below equation:

$$\sigma = \frac{t}{A} \times \frac{1}{R} \quad (\text{Equation 2.7})$$

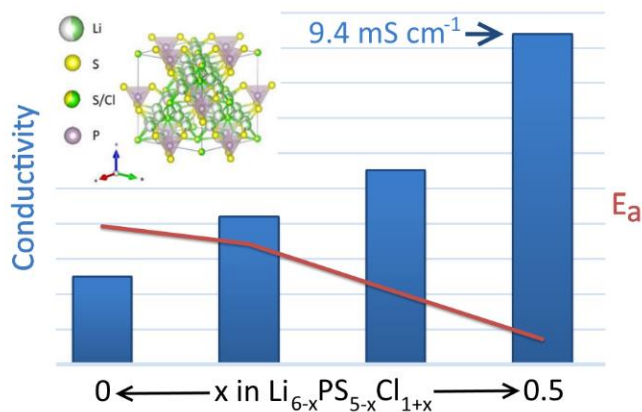
Where t, A and R are the thickness, area, and resistance of the specimen, respectively.

2.5 Raman Spectroscopy

Raman spectroscopy is a technique utilized to obtain details about vibrational and rotational modes in a system. Lasers are used as an excitation light source. When the laser illuminates the sample, elastic and inelastic scattering occurs. The elastically scattered radiation is filtered out and the

inelastically scattered radiation (Raman scattering) gives the chemical and structural information. A Raman spectrum includes a number of peaks displaying the intensity and wavelength of the Raman scattered light. Spectral lines observed in Raman act as fingerprints corresponding to a specific group of atoms within a structure. Raman spectra in this thesis were collected on the pelletized samples using Raman HORIBA HR800 at an excitation of 514 nm. Prior to Raman measurement for air-sensitive samples, they were placed between two glass slides and sealed with epoxy in the argon-filled glovebox.

Chapter 3 Halide-Rich Lithium Argyrodites



This section is reproduced in part with permission from John Wiley and Sons:

Parvin Adeli, J. David Bazak, Kern Ho Park, Ivan Kochetkov, Ashfia Huq, Gillian R. Goward, and Linda F. Nazar. Boosting solid-state diffusivity and conductivity in lithium superionic argyrodites by halide substitution, *Angew. Chem. Int. Ed.* 58, 2019, 8681-8686.

Contribution: In this chapter, CV measurements were carried out by Dr. K-H Park (Postdoc at UWaterloo). The NMR measurements and analysis were performed by D. Bazak in Prof. G. Goward's lab at McMaster University. Only a portion of the NMR data is presented here. For detailed NMR method and results, refer to the corresponding publication. See **Appendix A** - Data Use Permissions.

3.1 Introduction

Oxides are brittle and possess high grain boundary resistance. Contrary to oxides, sulfide-based materials exhibit deformable mechanical properties which is an important consideration in the optimization of solid-solid interfaces. Li-argyrodites, $\text{Li}_6\text{PS}_5\text{X}$ ($\text{X} = \text{Cl}, \text{Br}$), in the sulfide family are easily synthesized using inexpensive precursors. $\text{Li}_6\text{PS}_5\text{X}$ has a cubic crystal structure ($\text{F}\bar{4}3m$) comprised of PS_4^{3-} tetrahedra, with isolated S^{2-} and X^- ions disordered over the 4a and 4c Wyckoff sites in the lattice.^[56]

Adams *et al.* were the first to report room-temperature Li-ion conductivities for $\text{Li}_6\text{PS}_5\text{Cl}$ phase ($1.9 \text{ mS}\cdot\text{cm}^{-1}$)^[86] in 2011 and $\text{Li}_6\text{PS}_5\text{Br}$ phase ($0.7 \text{ mS}\cdot\text{cm}^{-1}$)^[87] in 2012. Viallet *et al.* also prepared $\text{Li}_6\text{PS}_5\text{Cl}$ in 2012 via high-energy ball milling followed by a five-hour heat treatment under argon. They investigated impact of milling length from 1 h to 20 h with a fixed rotation speed at 600 rpm and reported ionic conductivities in the range of $0.2 \text{ mS}\cdot\text{cm}^{-1}$ to $1.33 \text{ mS}\cdot\text{cm}^{-1}$ (10 h milling) for cold-pressed pellets.^[134] In 2017, Yu *et al.* reported that annealing $\text{Li}_6\text{PS}_5\text{Br}$ improves the ionic conductivity from 0.62 to $1.11 \text{ mS}\cdot\text{cm}^{-1}$ by lowering the grain boundary resistance.^[88] In 2018, Janek *et al.* reported $1.9 \text{ mS}\cdot\text{cm}^{-1}$ and $0.19 \text{ mS}\cdot\text{cm}^{-1}$ for $\text{Li}_6\text{PS}_5\text{Cl}$ and $\text{Li}_6\text{PS}_5\text{Br}$ phases respectively.^[105] With the recent efforts for enhancing ionic conductivity, reported values for lithium argyrodites are greater and comparable to those of liquid electrolytes. For example, Nan *et al.* prepared $\text{Li}_6\text{PS}_5\text{Cl}$ by a rapid solid-state route with an ionic conductivity of $3.15 \text{ mS}\cdot\text{cm}^{-1}$ for pellets pressed at 150 MPa.^[89] Total ionic conductivities are impacted by several factors including the synthesis approach (e.g., cooling rate),^[90] fraction of impurities and degree of crystallinity), grain boundary contributions, porosity,^[91] as well as methods that are implemented for conductivity measurements. These methods could comprise of densification techniques such as sintering the cold-pressed pellets,^[92] choice of contact (stainless steel, indium,

and Au sputtering) and carrying out the measurement under high pressure. It is important to consider these factors for developing an understanding of the underlying physiochemical factors responsible for changes in ionic diffusivity. In comparison to the solid-state synthesis, solution-based $\text{Li}_6\text{PS}_5\text{X}$ synthesis routes typically result in lower ion conductivities in the range of 10^{-5} - 10^{-4} $\text{mS}\cdot\text{cm}^{-1}$ due to phase impurities^[93-95] Nevertheless, Hayashi *et al.* recently reported higher room temperature values for $\text{Li}_6\text{PS}_5\text{Br}$ modified pellets which are $1.9 \text{ mS}\cdot\text{cm}^{-1}$ (cold-pressed at 720 MPa, Au contacts) and $3.1 \text{ mS}\cdot\text{cm}^{-1}$ (pressed at 720 MPa and sintered, Au contacts).^[96] Additionally, solution-prepared $\text{Li}_6\text{PS}_5\text{Cl}$ argyrodite (with 9% impurity including Li_3PO_4 , LiCl and Li_2S) exhibiting an ionic conductivity of $2.4 \text{ mS}\cdot\text{cm}^{-1}$ at 300 K was reported for pellets sintered at 550°C .^[97]

Solid electrolytes for practical battery applications should exhibit an ionic conductivity above $1 \text{ mS}\cdot\text{cm}^{-1}$ at room temperature. Considering the above-mentioned improvements and given the low electronic conductivity of $\text{Li}_6\text{PS}_5\text{Cl}$,^[134] it is a promising candidate for all-solid-state Li-ion batteries. Therefore, it has been explored in cells with different electrode materials.^[68,69,72]

The discovery of novel and advanced solid electrolytes is pivotal to solid state battery progress, but it has been hampered by insufficient understanding of the fundamental descriptors that govern ionic mobility. Many elegant studies have been devoted to this topic in $\text{Li}_6\text{PS}_5\text{X}$ (X = Cl, Br, I), including elucidation of the role of anion polarizability,^[75] and halogen disorder which is particularly important in argyrodites. Early studies showed that the very low ionic conductivity of $\text{Li}_6\text{PS}_5\text{I}$ (10^{-4} - $10^{-3} \text{ mS}\cdot\text{cm}^{-1}$), is due to the different distribution of I^- over the 4a and 4c crystallographic sites compared to the Cl^-/Br^- ions:^[87] the smaller halides exhibit disordered sulfide/halide occupation on the two sites, whereas the larger iodide anion only occupies the 4a site.

Wagemaker *et al.* studied $\text{Li}_6\text{PS}_5\text{X}$ using density functional molecular dynamics (MD) simulations to clarify the effect of halogen distribution and identified three types of Li-ion jumps in the cage-like polyhedra formed by Li^+ in the stable 48h Wyckoff site, and 24g transition site: short-range 48h-24g-48h “doublet jumps; short-range 48h-48h intra-cage jumps, and long-range inter-cage jumps.^[76] These studies elucidated that halogen disorder is advantageous for the inter-cage jump that is responsible for long-range Li-ion diffusion. The MD simulations also probed the effect of introducing more halogens (and hence more Li vacancies) into the argyrodite structure to form the theoretical compositions $\text{Li}_5\text{PS}_4\text{X}_2$, where the halides occupy all of the 4a and 4c sites. It was concluded that increasing the halogen content does not significantly alter the conductivity for $\text{Li}_5\text{PS}_4\text{Cl}_2$ and $\text{Li}_5\text{PS}_4\text{Br}_2$ phases which inspired this study to develop halide-rich compositions $\text{Li}_{6-x}\text{PS}_{5-x}\text{Cl}_{1+x}$ ($x \leq 0.5$) where halide/sulfide disorder should be maintained on the 4a and 4c sites. The structure of single-phase $\text{Li}_{5.5}\text{PS}_{4.5}\text{Cl}_{1.5}$ argyrodite was elucidated by neutron diffraction; and ionic mobility in the solid solution series $\text{Li}_{6-x}\text{PS}_{5-x}\text{Cl}_{1+x}$ ($x < 1$) was determined by a combination of electrical impedance spectroscopy (EIS) and pulsed field gradient (PFG) NMR. PFG NMR has seen increasing utility for transport measurements in solid electrolytes recently.^[98-101] The most halide-rich composition $\text{Li}_{5.5}\text{PS}_{4.5}\text{Cl}_{1.5}$ exhibits the highest room temperature Li^+ conductivity of $9.4 \pm 0.1 \text{ mS}\cdot\text{cm}^{-1}$ which is about four-fold above that $\text{Li}_6\text{PS}_5\text{Cl}$ prepared under identical processing conditions and a low activation energy of 0.29 eV. Impact of post-treatment was investigated on $\text{Li}_{5.5}\text{PS}_{4.5}\text{Cl}_{1.5}$. Sintered phase exhibited even better conductivity of $12 \pm 0.2 \text{ mS}\cdot\text{cm}^{-1}$. ^7Li PFG NMR spectroscopy and fast magic-angle spinning (MAS) NMR studies reported for the first time for $\text{Li}_{6-x}\text{PS}_{5-x}\text{Cl}_{1+x}$ shed light on the Li-ion diffusivity and local environment. They reveal heightened Li^+ diffusivity and weakened interactions of the Li^+ cation with the framework owing

to the substitution of the divalent sulfide for the monovalent halide and correlated diffusion of the Li^+ ions.

3.2 Material Synthesis and Characterization

Lithium sulfide (Li_2S , Sigma-Aldrich, 99.98%), phosphorus pentasulfide (P_2S_5 , Sigma-Aldrich, 99%), and lithium chloride (LiCl , Sigma-Aldrich, 99%) powders were used as starting precursors. The stoichiometric amounts of starting precursors (total weight about one gram) were mixed in a mortar for ten minutes in an argon-filled glovebox (H_2O , $\text{O}_2 < 1.5$ ppm) and then ball milled with 133 balls in a sealed zirconia jar using a high energy planetary ball mill (Fritsch PULVERISETTE 7 Premium). The milling speed and duration was 380 rpm and 17 h respectively. The powder was then recovered from the jar and re-mixed in a mortar. The microcrystalline powder was pelletized at two metric tons in a 10 mm (or 9 mm) die, placed in a glassy carbon capped crucible and vacuum-sealed in a quartz tube, and heat treated at 550°C for 5-7 hours leading to the final argyrodite products $\text{Li}_6\text{PS}_5\text{Cl}$, $\text{Li}_{5.75}\text{PS}_{4.75}\text{Cl}_{1.25}$, $\text{Li}_{5.625}\text{PS}_{4.625}\text{Cl}_{1.375}$, $\text{Li}_{5.5}\text{PS}_{4.5}\text{Cl}_{1.5}$ and $\text{Li}_6\text{PS}_5\text{Br}$. The heating and cooling rates were $0.5^\circ\text{C}/\text{min}$. All quartz tubes were preheated for two days at 100°C under vacuum to remove traces of water. For the Rietveld refinement of NPD data, $\text{Li}_6\text{PS}_5\text{Cl}$ structure in the space group $F\bar{4}3m$ was used as a starting point for the refinement.^[87] Refinement constraints that were used were as follows: the atomic coordinates and atomic displacement parameters were fixed to be the same for the shared site S1 and Cl1 (and for S2 and Cl2). The sum of occupancies was fixed at one for the shared sites ($\text{Occ}(\text{S1})+\text{Occ}(\text{Cl1})=1$ and $\text{Occ}(\text{S2})+\text{Occ}(\text{Cl2})=1$). The occupancies on the 4b and 16e sites were fixed at one. The Li-ion occupancy and atomic displacement parameter on the 48h site was fitted without constraints. All parameters were subsequently refined.

3.2.1 Electrochemical Impedance Spectroscopy

Ionic conductivity was measured by ac impedance spectroscopy. Microcrystalline powder samples were cold pressed at 2 tons for 2 minutes in a 10 mm (or 9 mm) diameter die. The experimental density of the cold pressed pellets was $87 \pm 1\%$ of theoretical. The pellets with varying thickness (see **Table 3.4** for thickness values) were placed between two indium foils that served as blocking electrodes in a modified cell for EIS measurements. Impedance spectroscopy was performed on the cold-pressed pellets at 298 K with a VMP3 potentiostat/galvanostat (Bio-logic) in the frequency range from 1 MHz to 0.1 Hz. The ionic conductivity was calculated by the equation $\sigma = t/RA$, where R is the total resistance of the solid electrolyte, t is the sample thickness, and A is the area of the solid electrolyte. For all the materials studied at 298 K, the CPE/R (constant phase element in parallel to resistor) shifted to frequencies that were too high to measure at room temperature with the impedance analyzer; therefore, a semicircle was not observed and only the tail of the Nyquist plot was used for the fit i.e., the resistances values were obtained using the intercept of the linear fit of the Warburg curve with the real axis. For halide-rich $\text{Li}_{5.5}\text{PS}_{4.5}\text{Cl}_{1.5}$ phase, EIS measurements were carried out at 195 K as well.

For activation energy (E_a) measurements, variable temperature EIS was carried out in cells (under a constant 0.5 ton pressure) that were placed in an oven with precise temperature control (Binder, Germany) and an external thermocouple for independent temperature measurement. The cell was connected to a MTZ-35 impedance analyzer (Bio-Logic) controlled by the MT-LAB (Bio-Logic) software, and the impedance was measured from 35 MHz to 0.1 Hz in five degree increments from 298 K to 338 K, with two hours allowed for equilibration at each temperature. The conductivity measurements on $\text{Li}_{5.5}\text{PS}_{4.5}\text{Cl}_{1.5}$ at 286 K and 195 K were carried out by immersing the sealed EIS cell in a cooling bath and allowing it to equilibrate to temperature. The

fit was performed using the EC-Lab software. For all of the materials that were explored in this work, ac impedance measurements were repeated to obtain an error estimate.

3.2.2 Electrochemical Measurements

The electronic conductivity of the $\text{Li}_{5.5}\text{PS}_{4.5}\text{Cl}_{1.5}$ electrolyte was measured according to the DC polarization curve using stainless steel ion blocking electrodes.

The cyclic voltammograms of $\text{Li}/\text{Li}_{5.5}\text{PS}_{4.5}\text{Cl}_{1.5}/\text{SS}$ and $\text{Li}/\text{Li}_6\text{PS}_5\text{Cl}/\text{SS}$ were recorded in a voltage window of 5.0 to -0.1 V at a scan rate of 1 mV s^{-1} at room temperature. The solid electrolyte pellets were pressed at 125 MPa to yield thicknesses of 0.158 cm and 0.155 cm for $\text{Li}_{5.5}\text{PS}_{4.5}\text{Cl}_{1.5}$ and $\text{Li}_6\text{PS}_5\text{Cl}$ respectively with a diameter of 10 mm. The stability of the electrolyte against Li metal was investigated by a dissolution-deposition cycle test using a symmetric $\text{Li}/\text{Li}_{5.5}\text{PS}_{4.5}\text{Cl}_{1.5}/\text{Li}$ cell at a current density of 0.25 mA cm^{-2} .

3.3 Results and Discussion

Targeted argyrodite compositions $\text{Li}_{6-x}\text{PS}_{5-x}\text{Cl}_{1+x}$ ($x = 0, 0.25, 0.375, 0.5, 0.55, 0.6$) were prepared by ball-milling the precursors, which were heated at 550°C for five to seven hours. Neutron diffraction data was collected for $\text{Li}_{5.5}\text{PS}_{4.5}\text{Cl}_{1.5}$ composition which exhibited the highest ionic conductivity among the studied compositions. Neutron diffraction pattern and Rietveld refinement for this phase are shown in **Figure 3.1**. **Table 3.1** contains details of atomic coordinates, occupation factor (SOF) and isotropic displacement parameters (U_{iso}). Refinement results suggest that only one Li ($48h$) site is present, with no Li present on the $24g$ site; S1/Cl1 and S2/Cl2 share the $4a$ and $4c$ sites, with the additional Cl^- being distributed evenly over both sites (**Figure 3.2**). In accord with the refinement results, one main resonance corresponding to one Li site is observed in the ^7Li MAS NMR data (**Figure 5.10**) for $\text{Li}_{5.5}\text{PS}_{4.5}\text{Cl}_{1.5}$.

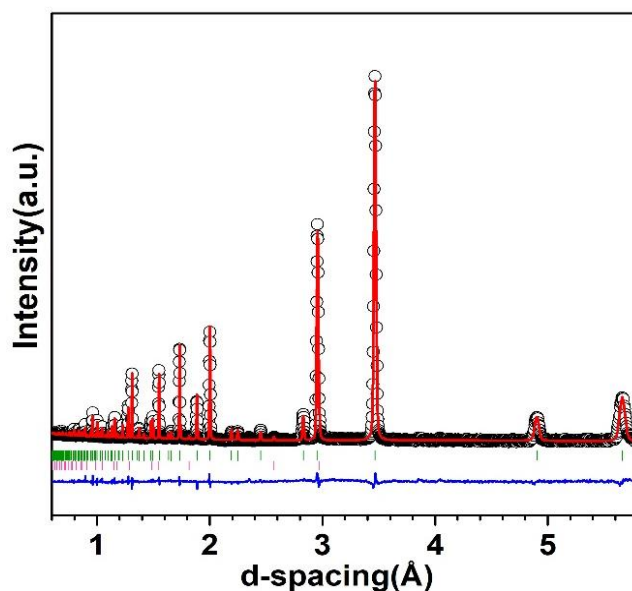


Figure 3.1 Rietveld fit of $\text{Li}_{5.5}\text{PS}_{4.5}\text{Cl}_{1.5}$, refined against time-of-flight (TOF) neutron powder diffraction data collected at 298 K (GOF = 3.37, $R_{\text{wp}} = 4.88\%$). The black circles denote the observed pattern, and the red solid line indicates the calculated pattern. The difference map is in blue. Calculated positions of the Bragg reflections are represented by the vertical tick marks in green, and the ticks for the minority LiCl phase (1.7 wt%) are shown in pink.

Table 3.1 Atomic coordinates, occupation factor and isotropic displacement parameters of $\text{Li}_{5.5}\text{PS}_{4.5}\text{Cl}_{1.5}$ obtained from Rietveld refinement of neutron TOF data (space group $F\bar{4}3m$), $a = 9.8061(1)$ Å. The composition from the fit is $\text{Li}_{5.47}\text{PS}_{4.55}\text{Cl}_{1.45}$, very close to the nominal.

Atom	Wyckoff Site	x	y	z	SOF	$U_{\text{iso}}(\text{Å}^2)$
Li	48h	0.3173(7)	0.3173	-0.0201(9)	0.456(16)	0.075(4)
P	4b	1/2	1/2	1/2	1	0.030(2)
Cl1	4a	0	0	0	0.615(17)	0.029(1)
S1	4a	0	0	0	0.385(17)	0.029(1)
Cl2	4c	1/4	1/4	1/4	0.834(16)	0.037(1)
S2	4c	1/4	1/4	1/4	0.166(16)	0.037(1)
S3	16e	0.1188	-0.1188	0.6188	1	0.050(1)

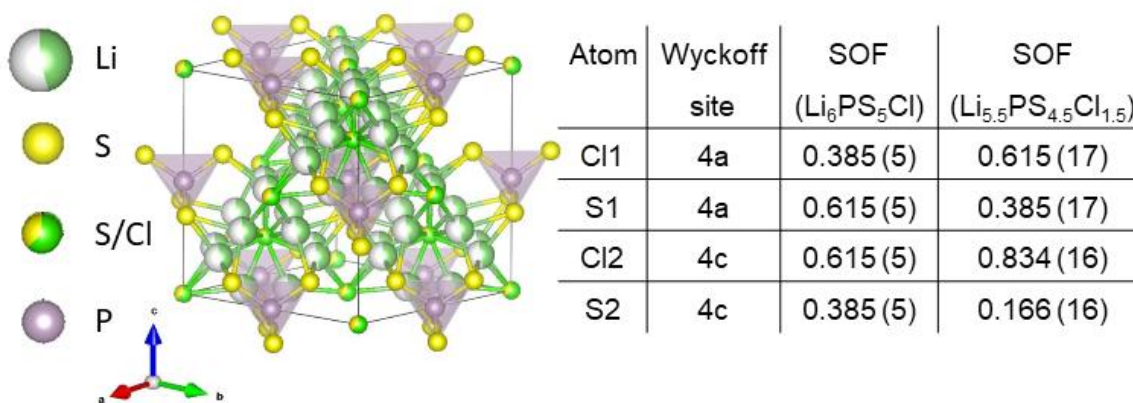


Figure 3.2 Crystal structure of $\text{Li}_{5.5}\text{PS}_{4.5}\text{Cl}_{1.5}$ showing the PS_4^{3-} tetrahedra, lithium-ion cages, free $\text{S}^{2-}/\text{Cl}^-$ anions, and comparison of occupancies (SOF) on the 4a and 4c sites between $\text{Li}_6\text{PS}_5\text{Cl}$ (from ref 75) and $\text{Li}_{5.5}\text{PS}_{4.5}\text{Cl}_{1.5}$.

The EDS mapping of $\text{Li}_{5.5}\text{PS}_{4.5}\text{Cl}_{1.5}$ (**Figure 3.3**) indicates elemental ratios are in excellent accord with the targeted values, and a homogenous distribution of P, S and Cl at the micron scale.

Summary of the EDX analysis for $\text{Li}_{6-x}\text{PS}_{5-x}\text{Cl}_{1+x}$ ($x = 0, 0.25, 0.5$) is presented in **Table 3.2**.

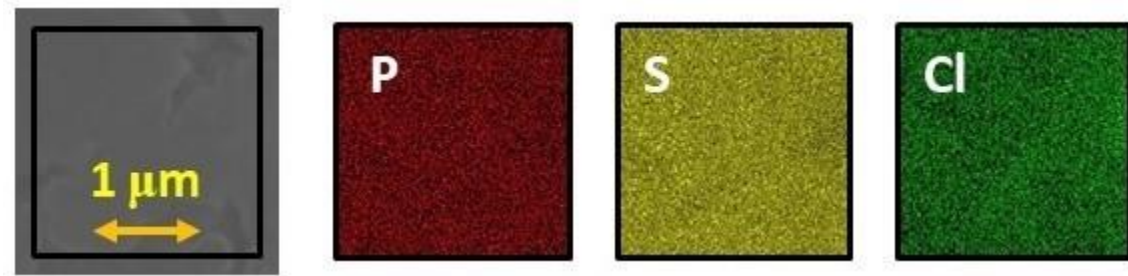


Figure 3.3 EDS mapping of the heat-treated $\text{Li}_{5.5}\text{PS}_{4.5}\text{Cl}_{1.5}$ sample, which indicates a homogenous distribution of P, S and Cl at the micron scale.

Table 3.2 EDX analysis of the $\text{Li}_{6-x}\text{PS}_{5-x}\text{Cl}_{1+x}$ ($x = 0, 0.25, 0.5$). Two measurements per sample are represented. The sulfur content was not quantified due to minor hydrolysis that occurs during the sample transfer into the SEM chamber.

Targeted	Measurement	Observed Cl/P ratio	Average ratio	Element	Atomic percent	Weight percent
$\text{Li}_6\text{PS}_5\text{Cl}$	M1	1.04	0.99	P-K	16.85	16.07
				Cl-K	17.45	19.05
	M2	0.94		P-K	17.49	16.70
				Cl-K	16.42	17.95
$\text{Li}_{5.75}\text{PS}_{4.75}\text{Cl}_{1.25}$	M1	1.26	1.25	P-K	14.7	13.98
				Cl-K	18.5	20.12
	M2	1.24		P-K	15.8	14.99
				Cl-K	19.6	21.37
$\text{Li}_{5.5}\text{PS}_{4.5}\text{Cl}_{1.5}$	M1	1.50	1.51	P-K	14.7	13.95
				Cl-K	22	23.84
	M2	1.52		P-K	13.9	13.16
				Cl-K	21.2	23.05

The higher ratio of Cl^- ions to S^{2-} ions in $\text{Li}_{5.5}\text{PS}_{4.5}\text{Cl}_{1.5}$ leads to a greater fraction of Li vacancies compared to the parent phase $\text{Li}_6\text{PS}_5\text{Cl}$, as evidenced by the lower Li occupancy on the 48h site. The large atomic displacement parameter for the Li site (0.075 \AA^2) suggests high room temperature mobility of the Li-ion as discussed below. XRD patterns of the other members of the series Li_6 .

$x\text{PS}_{5-x}\text{Cl}_{1+x}$ ($x < 0.5$) are represented in **Figure 3.4**. Similar to $x = 0.5$, these targeted compositions showed negligible fractions of impurities.

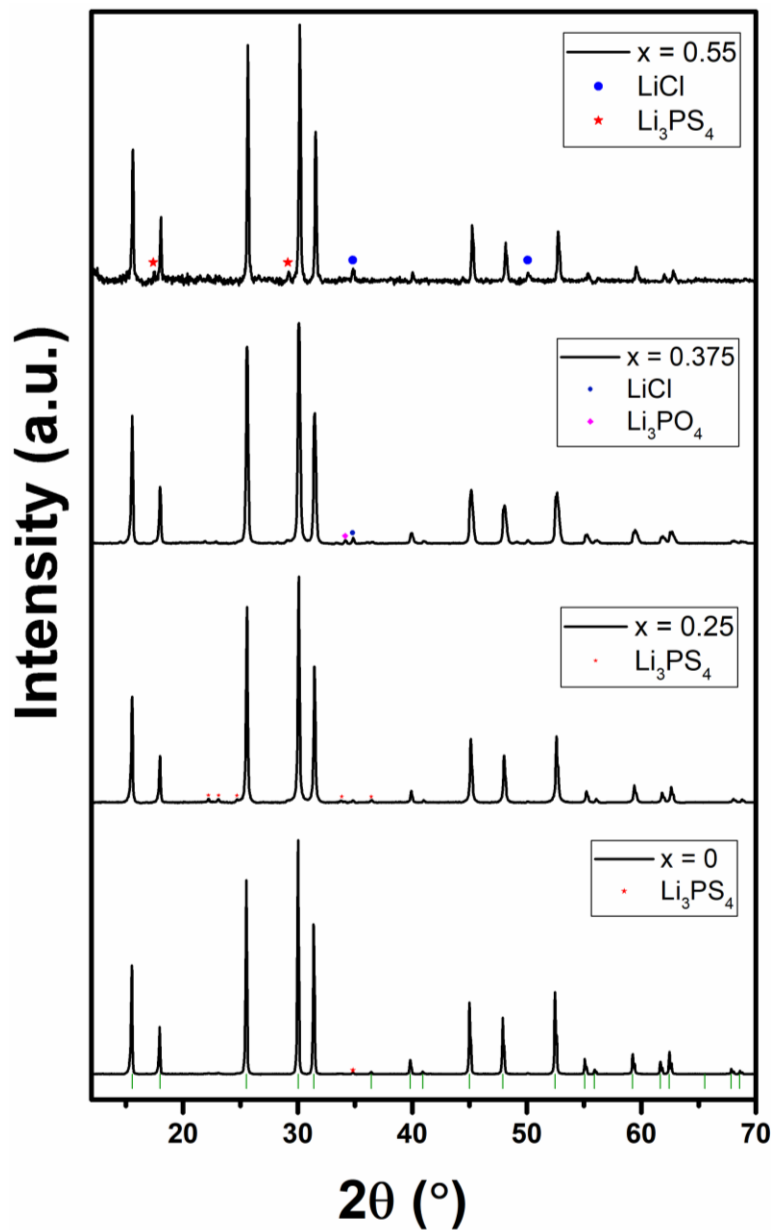


Figure 3.4 XRD patterns of $\text{Li}_{6-x}\text{PS}_{5-x}\text{Cl}_{1+x}$ ($x = 0, 0.25, 0.375$ and 0.55) showing the identified impurities. Calculated positions of the Bragg reflections are represented by the vertical tick marks in green.

Full-profile (LeBail) fitting was used to extract the cubic lattice parameter, a , which is plotted against x in **Figure 3.5a** to show a linear relationship (Vegard's law). The lattice volume of this solid solution shrinks monotonically with increasing x , evidenced by a small decrease in the cell parameter from $a = 9.8598(4)$ Å for $\text{Li}_6\text{PS}_5\text{Cl}$, to $a = 9.8061(1)$ Å for $\text{Li}_{5.5}\text{PS}_{4.5}\text{Cl}_{1.5}$. This decrease in a owes in most part to the Li^+ vacancies, since S^{2-} (170 pm) and Cl^- (167 pm) have very close ionic radii. Various experimental efforts to introduce additional chlorine into the structure resulted in significant exsolution of LiCl at $x > 0.5$ (corresponding XRD pattern is shown in **Figure 3.4**) which is detrimental to ionic conductivity as discussed later. Thermodynamic instability of the lattice at high vacancy content could govern this solvation limit. Therefore, while $\text{Li}_5\text{PS}_4\text{Cl}_2$ was proposed to be a stable composition by Wagemaker *et al.* based on theory,^[76] our experimental efforts show that $\text{Li}_{5.5}\text{PS}_{4.5}\text{Cl}_{1.5}$ is indeed the end member. Analogous attempts to increase the $\text{Br}^-/\text{S}^{2-}$ ratio in $\text{Li}_{6-x}\text{PS}_{5-x}\text{Br}_{1+x}$ showed significant LiBr fractions even at $x = 0.25$. XRD patterns for the synthesized single-phase $\text{Li}_6\text{PS}_5\text{Br}$ and attempted halide rich $\text{Li}_{5.5}\text{PS}_{4.5}\text{Br}_{1.5}$ are demonstrated in **Figure 3.6**. This indicates that solution behaviour is not adopted and is likely due to the larger radius of Br^- (182 pm) which increases the local structural distortion instigated at the modified site.^[102] Given the observation with targeted Br-rich phases, formation of the theoretically anticipated iodide $\text{Li}_{6-x}\text{PS}_{5-x}\text{I}_{1+x}$ phases^[76] would also not likely be possible.

Ionic conductivity for $\text{Li}_{6-x}\text{PS}_{5-x}\text{Cl}_{1+x}$ ($0 \leq x \leq 0.6$) was determined by EIS at variable temperatures. Complex impedance plots collected at 298 K for $x = 0, 0.25, 0.5$ and (0.5, sintered) are shown in **Figure 3.5b** and the resultant total ionic conductivity data is presented in **Table 3.3**. Extracted thickness and resistance values of the impedance analyses are reported in **Table 3.4**.

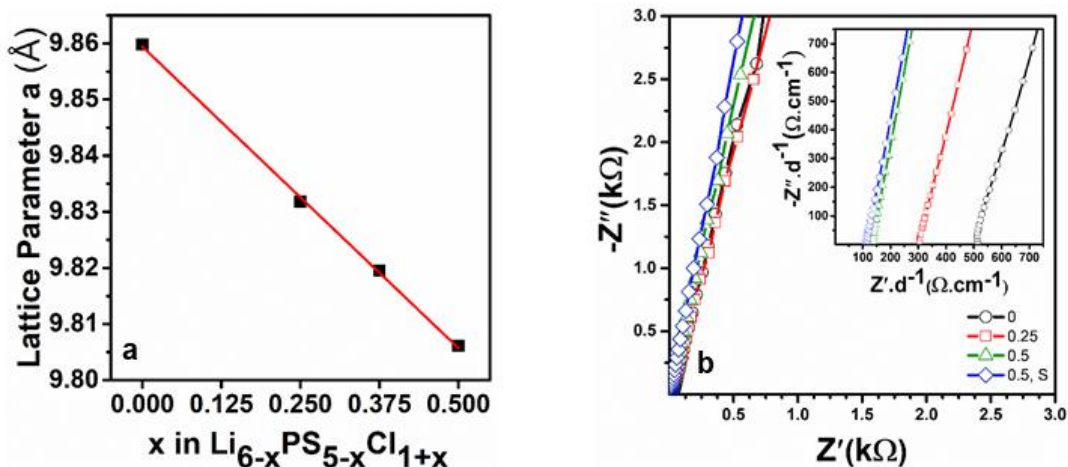


Figure 3.5 a) Lattice parameter of $\text{Li}_{6-x}\text{PS}_{5-x}\text{Cl}_{1+x}$ vs x showing that Vegard's law for a solid solution is obeyed; b) room temperature complex impedance plots of the cold-pressed pellets of $\text{Li}_6\text{PS}_5\text{Cl}$, $\text{Li}_{5.75}\text{PS}_{4.75}\text{Cl}_{1.25}$, $\text{Li}_{5.5}\text{PS}_{4.5}\text{Cl}_{1.5}$, and a sintered pellet of $\text{Li}_{5.5}\text{PS}_{4.5}\text{Cl}_{1.5}$ (550°C for 10 min). Inset = magnified view at high frequencies, where the impedance is normalized to the respective pellet thickness (d) for better comparison of different compositions.

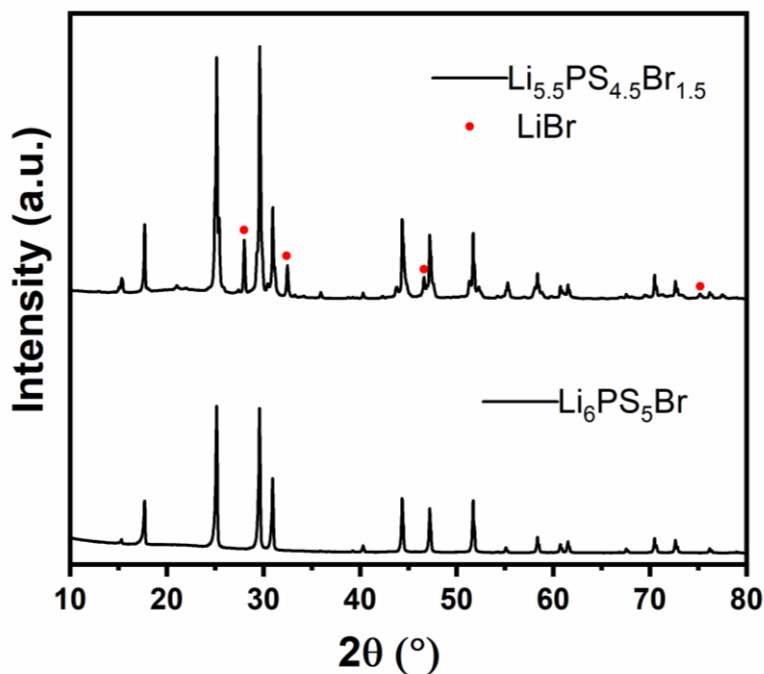


Figure 3.6 XRD patterns of $\text{Li}_{6-x}\text{PS}_{5-x}\text{Br}_{1+x}$ ($x = 0, 0.5$). $\text{Li}_6\text{PS}_5\text{Br}$ was obtained as pure phase. LiBr impurity peaks are identified with red circles for $\text{Li}_{5.5}\text{PS}_{4.5}\text{Br}_{1.5}$.

Table 3.3 Summary of the ionic conductivity (σ_i , for pellets cold-pressed at 2 tons) at 298 K for the synthesized Li-argyrodites. Error in the ionic conductivities is determined from the span in the measurements for multiple samples of the same composition (extracted values of the impedance analyses are tabulated in **Table 3.4**).

$\text{Li}_{6-x}\text{PS}_{5-x}\text{Cl}_{1+x}$	$\sigma_i(\text{tot}) \text{ mS}\cdot\text{cm}^{-1}$
$\text{Li}_6\text{PS}_5\text{Cl}$	2.5(1)
$\text{Li}_{5.75}\text{PS}_{4.75}\text{Cl}_{1.25}$	4.2(2)
$\text{Li}_{5.625}\text{PS}_{4.625}\text{Cl}_{1.375}$	5.6(2)
$\text{Li}_{5.5}\text{PS}_{4.5}\text{Cl}_{1.5}$	9.4(1)
$\text{Li}_{5.5}\text{PS}_{4.5}\text{Cl}_{1.5}$, sintered	12.0(2)
$\text{Li}_{5.45}\text{PS}_{4.45}\text{Cl}_{1.55}$	5.9(2)
$\text{Li}_{5.4}\text{PS}_{4.4}\text{Cl}_{1.6}$	3.3(1)

Table 3.4 Room temperature resistance values for $\text{Li}_{6-x}\text{PS}_{5-x}\text{Cl}_{1+x}$ (pellets of 1.0 cm diameter) which were obtained from the fit of the real-axis impedance intercept in the Nyquist plot, illustrating the sampling used to derive the standard deviation in the reported conductivities. Nyquist plots for series A are represented in **Figure 3.5b**.

Sample series		x=0	x=0.25	x=0.375	x=0.5
A	Thickness (mm)	0.630	0.660	-	0.738
	R (Ω)	31.3	20	-	10
	Total σ	2.6	4.2	-	9.4
B	Thickness (mm)	0.68	1.03	0.647	1.01
	R (Ω)	36.2	33	14.9	13.9
	Total σ	2.4	4.0	5.5	9.3
C	Thickness (mm)	1.03	0.665	0.846	1.00
	R (Ω)	51.3	19.1	18.4	13.4
	Total σ	2.6	4.4	5.9	9.5
D	Thickness (mm)	-	-	0.700	0.896
	R (Ω)	-	-	16.3	12.2
	Total σ	-	-	5.5	9.4
	σ_{average}	2.5	4.2	5.6	9.4
	Standard deviation $\sqrt{\frac{\sum (x-\bar{x})^2}{n}}$	0.1	0.2	0.2	0.1

For $\text{Li}_{5.5}\text{PS}_{4.5}\text{Cl}_{1.5}$, additional EIS data were collected at 286 K and 195 K. These points are displayed in **Figure 3.7**. Nyquist plot for 195 K is shown in **Figure 3.7**, inset. The full semicircle

in the Nyquist plot was fit with an equivalent circuit composed of one CPE/R (constant phase element in parallel to the resistor) in series with a CPE representing the blocking electrodes. Characteristic of a soft thiophosphate, bulk and grain boundary contributions could not be deconvoluted for these argyrodites and the conductivity represents the total. At 298 K, the CPE/R falls beyond the range of the impedance analyzer and the tail of the blocking electrodes was fit to obtain the total conductivity values. Fitted EIS (at 195 K) parameters are presented in **Table 3.5**. The apex frequency is 1.11×10^5 Hz, which corresponds to a capacitance of 1.7×10^{-9} F. The α -value is close to 0.9, indicating the ideality of the CPE.

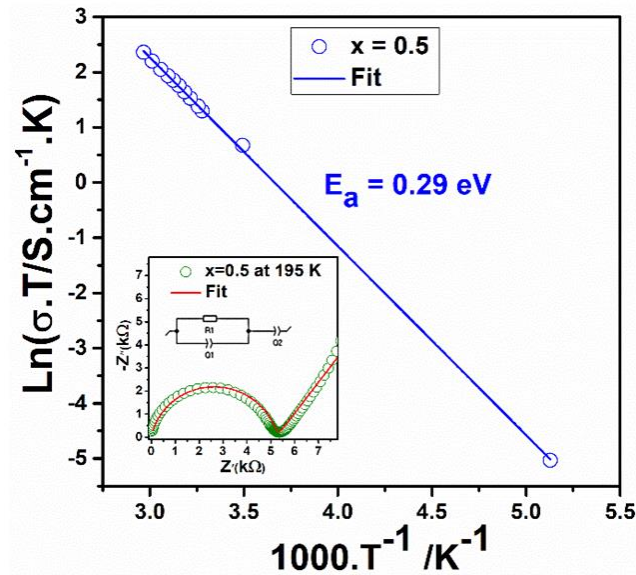


Figure 3.7 Full temperature range Arrhenius plot for $\text{Li}_{5.5}\text{PS}_{4.5}\text{Cl}_{1.5}$ phase and corresponding Nyquist plot at 195K (inset). The apex frequency is 1.11×10^5 Hz, which corresponds to a capacitance of 1.7×10^{-9} F; the α -value is about 0.9, indicating the ideality of the CPE.

Table 3.5 Fitted EIS parameters for $\text{Li}_{5.5}\text{PS}_{4.5}\text{Cl}_{1.5}$ at 195 K ($r_{\text{electrode}} = 0.45$ cm).

Equivalent circuit=	R1/Q1 + Q2
R1	5233 ohm
Q1	$1.487\text{e-}9 \text{ F.s}^{(a-1)}$
a1	0.8825
Q2	$29.26\text{e-}6 \text{ F.s}^{(a-1)}$
a2	0.5937

$\text{Li}_6\text{PS}_5\text{Cl}$ exhibits a conductivity of $\sigma_i = 2.5 \text{ mS.cm}^{-1}$ at 298 K which is consistent with reported values in the literature ($1.1 - 3.15 \text{ mS.cm}^{-1}$).^[86, 89, 97] Substitution of S^{2-} for Cl^- in $\text{Li}_6\text{PS}_5\text{Cl}$ results in an almost exponential increase with x . This exponential trend is depicted in **Figure 3.8**. The highest ionic conductivity of $9.4 \pm 0.1 \text{ mS.cm}^{-1}$ is reached for the composition $\text{Li}_{5.5}\text{PS}_{4.5}\text{Cl}_{1.5}$, almost a four-fold increase *vis a vis* $\text{Li}_6\text{PS}_5\text{Cl}$. The effect of post synthesis annealing was probed

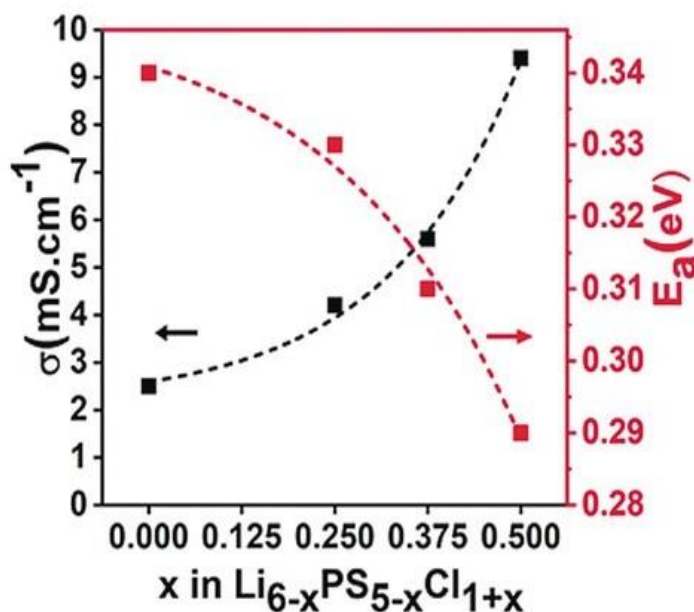


Figure 3.8 Conductivity and activation energy (from EIS) for $\text{Li}_{6-x}\text{PS}_{5-x}\text{Cl}_{1+x}$ ($x = 0, 0.25, 0.375$ and 0.5).

by sintering pellets of $\text{Li}_{5.5}\text{PS}_{4.5}\text{Cl}_{1.5}$ at 550°C for 10 min. As a consequence of optimizing grain boundary conductivity, sintered $\text{Li}_{5.5}\text{PS}_{4.5}\text{Cl}_{1.5}$ exhibited an even higher ionic conductivity of $12.0 \pm 0.2 \text{ mS}\cdot\text{cm}^{-1}$. Electronic conductivity of $\text{Li}_{5.5}\text{PS}_{4.5}\text{Cl}_{1.5}$ was determined by fitting the DC polarisation curve. It is noted that $\text{Li}_{5.5}\text{PS}_{4.5}\text{Cl}_{1.5}$ exhibits a low electronic conductivity of $\sim 3 \times 10^{-9} \text{ S}\cdot\text{cm}^{-1}$ (**Figure 3.9**) similar to the parent phase, which is practically important in determining a transference number close to one.

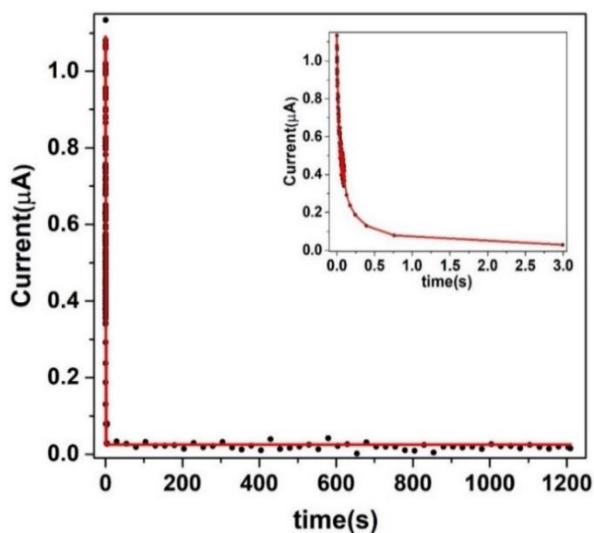


Figure 3.9 Direct current (DC) polarisation data for electronic conductivity determination for $\text{Li}_{5.5}\text{PS}_{4.5}\text{Cl}_{1.5}$. The DC polarisation curve was fitted with a decay function, and the steady current value at the end of the curve was extrapolated. The electronic conductivity of $3 \times 10^{-9} \text{ S}\cdot\text{cm}^{-1}$ was calculated by using Ohm's law.

Activation energies (E_a) for Li-ion mobility in $\text{Li}_{6-x}\text{PS}_{5-x}\text{Cl}_{1+x}$ were determined from both EIS and PFG NMR temperature-dependent measurements. The corresponding E_a values are tabulated in **Table 3.6**. Although comparison of these two values implies consideration of the bulk conductivity from EIS, the ideality of the semicircle and capacitance in **Figure 3.7** correspond to

Table 3.6 Summary of the activation energy (E_a) values obtained from EIS and PFG Arrhenius plots for the synthesized Li-argyrodites.

$\text{Li}_{6-x}\text{PS}_{5-x}\text{Cl}_{1+x}$	E_a (EIS) eV	E_a (PFG) eV
$\text{Li}_6\text{PS}_5\text{Cl}$	0.34(1)	0.35(1)
$\text{Li}_{5.75}\text{PS}_{4.75}\text{Cl}_{1.25}$	0.33(1)	0.343(9)
$\text{Li}_{5.625}\text{PS}_{4.625}\text{Cl}_{1.375}$	0.31(1)	0.320(3)
$\text{Li}_{5.5}\text{PS}_{4.5}\text{Cl}_{1.5}$	0.29(1)	0.29(1)

bulk transport,^[103] and it is fair to assume that grain boundary contributions do not significantly affect the observed trend in **Figure 3.7**. Activation energy for $\text{Li}_6\text{PS}_5\text{Cl}$ ranges between 0.33-0.38 eV in the literature where values are extracted from $\ln \sigma T$ vs T^{-1} .^[86,104,105,134] In this work, activation energy of $\text{Li}_6\text{PS}_5\text{Cl}$ was determined to be 0.34 eV. $\text{Li}_{5.5}\text{PS}_{4.5}\text{Cl}_{1.5}$ exhibits Arrhenius behavior with a low activation energy of 0.29 eV which is considerably smaller than that of $\text{Li}_6\text{PS}_5\text{Cl}$ (**Figure 3.8**). The activation energies obtained from EIS (**Figure 3.7** and **Figure 3.10**) follow an inverse

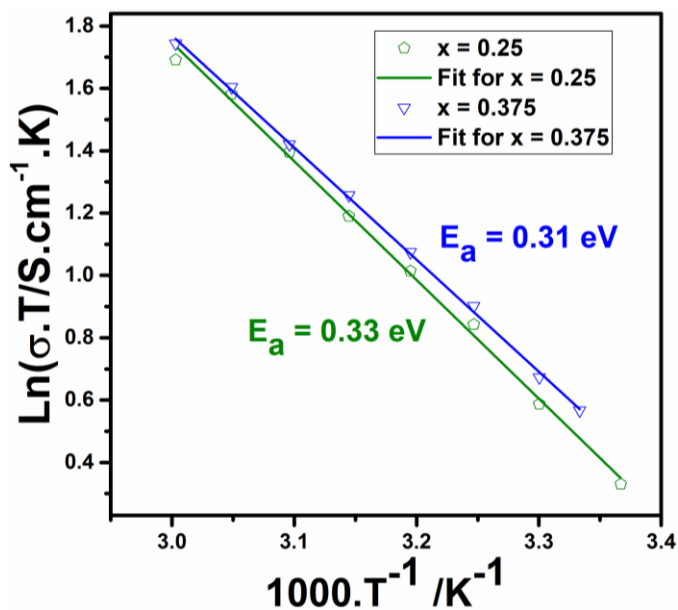


Figure 3.10 Temperature dependence of the ionic conductivity for $x = 0.25$ and $x = 0.375$.

correlation with conductivity (**Figure 3.8**). While going from $x = 0$ to $x = 0.5$, various factors synergistically impact decreasing the activation energy, enhancing diffusion and the ionic transport:

- 1) The increase in the total fraction of Cl^- on the S^{2-} site from 61% for $\text{Li}_6\text{PS}_5\text{Cl}$ to 83% for $\text{Li}_{5.5}\text{PS}_{4.5}\text{Cl}_{1.5}$ plays a role in decreasing the activation energy.
- 2) Increase in Li vacancy content which further drives the increased diffusivity. Statistically, there will be a greater chance of an empty doublet of 48 sites near the Cl^- ions, that will facilitate interstage jumps.
- 3) The substitution of monovalent Cl^- halogen with lower ionic charge for divalent S^{2-} will reduce the electrostatic attraction of the mobile Li ions to the framework anions.
- 4) Decrease in the interstage jump distance from 2.88 Å ($x = 0$) to 2.81 Å ($x = 0.5$) (distance values were determined from the diffraction data). This decrease is due to the shrinkage of the unit cell and will favour higher jump rates. However, this effect is expected to be small.

^7Li PFG NMR diffusivity measurements were carried out from 270 K to 340 K. It was observed that by increasing x in $\text{Li}_{6-x}\text{PS}_{5-x}\text{Cl}_{1+x}$, diffusivity increases. Comparison of the Arrhenius plots of diffusivity for $x = 0$ and $x = 0.5$ phases from both EIS and PFG are presented in **Figure 3.11**. $\text{Li}_{5.5}\text{PS}_{4.5}\text{Cl}_{1.5}$ exhibits a marvelous diffusion coefficient of $1.01 \times 10^{-11} \text{ m}^2\text{s}^{-1}$ at 300 K. In order to

put this value into perspective, it is compared to that reported from PFG NMR measurements of benchmark sulfide materials^[98,106] in table **Table 3.7**.

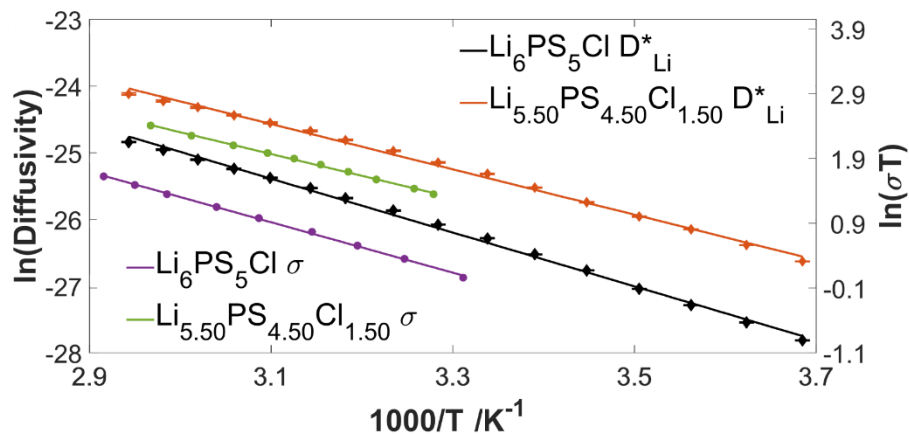


Figure 3.11 Arrhenius plots of the diffusivity and conductivity values for $x = 0$ and $x = 0.5$ from PFG and EIS.

Table 3.7 Diffusion coefficient of materials compared to halide-rich phase.

Electrolyte	Diffusion coefficient	Ref
$\text{Li}_{10}\text{GeP}_2\text{S}_{12}$	$2.2 \times 10^{-12} \text{ m}^2\text{s}^{-1}$	98
$\text{Li}_{11}\text{Si}_2\text{PS}_{12}$	$3.5 \times 10^{-12} \text{ m}^2\text{s}^{-1}$	106
$\text{Li}_{5.5}\text{PS}_{4.5}\text{Cl}_{1.5}$	$1.01 \times 10^{-11} \text{ m}^2\text{s}^{-1}$	This work

Stability of $\text{Li}_6\text{PS}_5\text{Cl}$ vs $\text{Li}_{5.5}\text{PS}_{4.5}\text{Cl}_{1.5}$

Electrochemical window has been used in the literature to evaluate the stability of sulfide electrolytes against Li metal. For $\text{Li}_6\text{PS}_5\text{Cl}$, an excellent stability with electrochemical window of more than 5 V was claimed.^[89] Here the current response and anodic stability for $\text{Li}_6\text{PS}_5\text{Cl}$ and $\text{Li}_{5.5}\text{PS}_{4.5}\text{Cl}_{1.5}$ are compared. Cyclic voltammetry (CV) carried out in a SS/ $\text{Li}_{5.5}\text{PS}_{4.5}\text{Cl}_{1.5}$ /Li cell

shows Li deposition and stripping around 0 V vs Li/Li⁺ (**Figure 3.12a**). The current response of Li_{5.5}PS_{4.5}Cl_{1.5} is significantly higher than the Li₆PS₅Cl phase as a result of its higher ionic conductivity (**Figure 3.12b**).

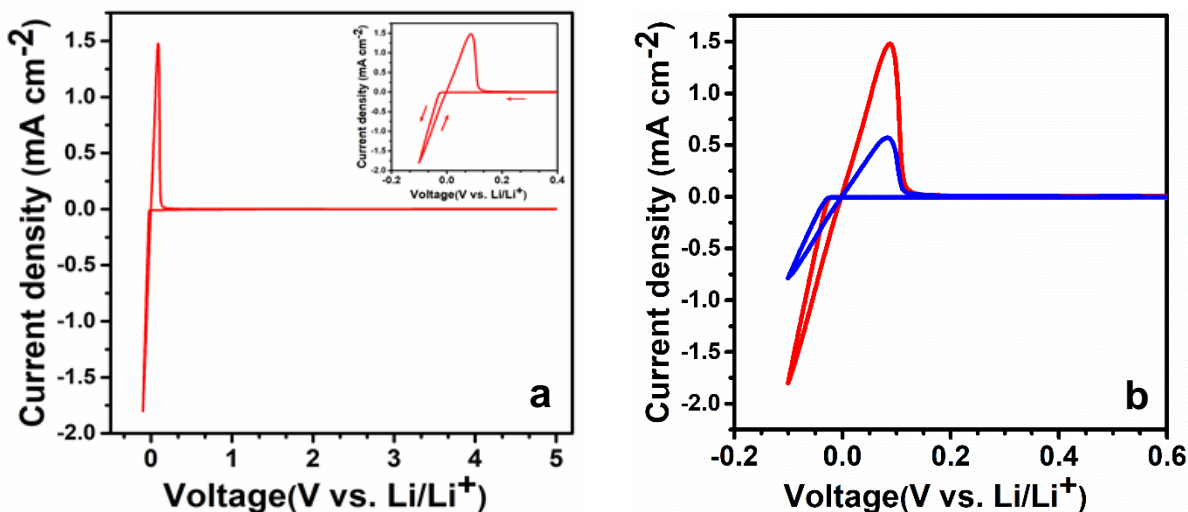


Figure 3.12 a) Cyclic voltammogram using a Li/Li_{5.5}PS_{4.5}Cl_{1.5}/stainless steel cell with a scan rate of 1 mV s⁻¹ in the voltage window of 5.0 - 0.1 V. b) Comparison of cyclic voltammogram using Li/Li_{5.5}PS_{4.5}Cl_{1.5}/stainless steel (red line) and Li/Li₆PS₅Cl/stainless steel (blue line) cells with a scan rate of 1 mV s⁻¹ in the voltage window of 5.0 - 0.1 V.

Furthermore, a comparison of CVs on the anodic scan alone reveals an initial, miniscule anodic current (note y-axis) on the first scan for Li_{5.5}PS_{4.5}Cl_{1.5} corresponding to formation of a passivating interphase that we assign to insulating sulfur formed from oxidation of sulfide in the lattice. It diminishes to virtually zero on the second cycle (**Figure 3.13a**). On the other hand, the anodic current for Li₆PS₅Cl is initially higher (**Figure 3.13b**) and is still measurable on the second sweep. Therefore, Li_{5.5}PS_{4.5}Cl_{1.5} exhibits better anodic stability in these studies, likely due to its lower sulfide content. Studies in cells with active cathode materials need to be conducted to fully evaluate stability but these are beyond the scope of this thesis.

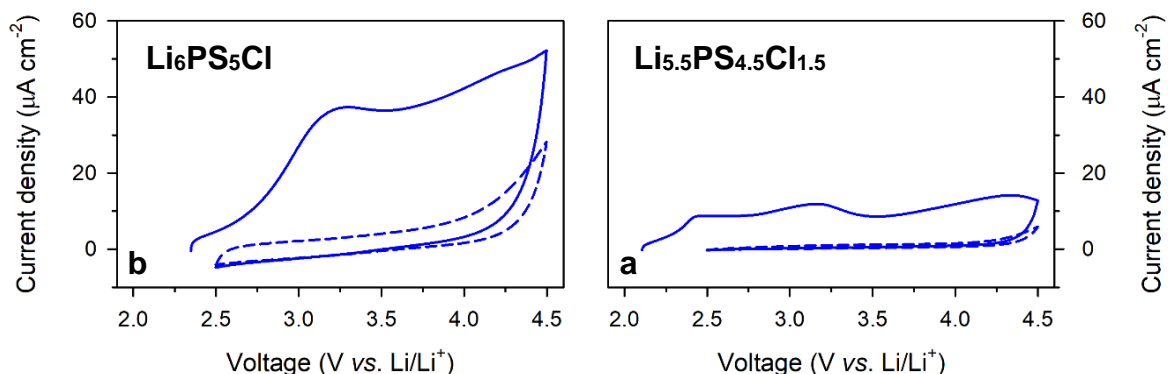


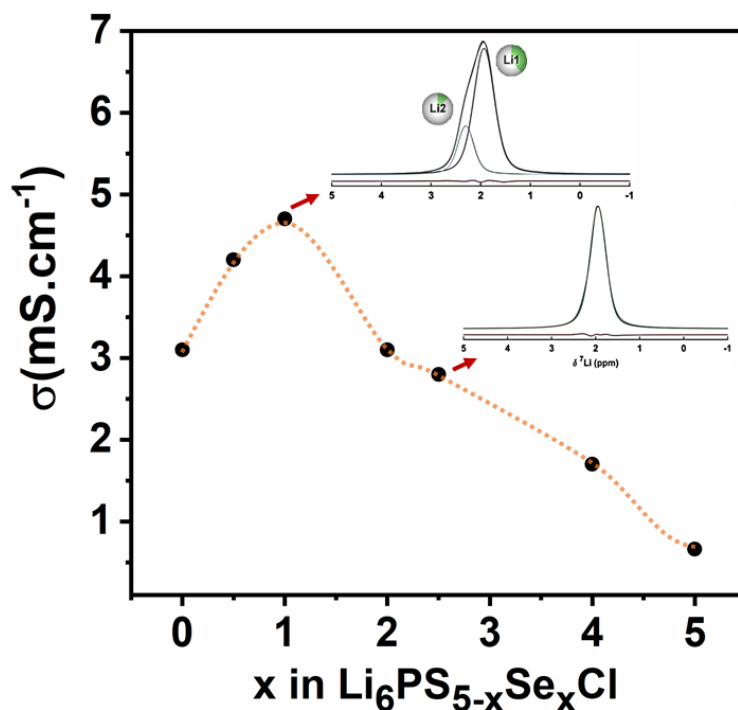
Figure 3.13 a) Cyclic voltammogram of a Li/SE/stainless steel cell using $\text{Li}_6\text{PS}_5\text{Cl}$ or $\text{Li}_{5.5}\text{PS}_{4.5}\text{Cl}_{1.5}$ as a solid electrolyte layer with scan rate of 1 mV s^{-1} . The first (solid) and second (dashed) scans are shown.

3.4 Conclusion

In summation, a new halide-rich solid solution series $\text{Li}_{6-x}\text{PS}_{5-x}\text{Cl}_{1+x}$ was explored and the changes to ionic transport that halide substitution incurs were investigated. Neutron diffraction and variable temperature impedance spectroscopy, in conjunction with ^7Li PFG and MAS NMR studies, provide deep knowledge of structure and ion dynamics. With increasing Cl and Li vacancy content, a significant and systematic lowering of the activation barrier and increase in Li-ion diffusivity was observed. This coincides with an increase of the $\text{Cl}^-/\text{S}^{2-}$ disorder and marks the influence of the monovalent anion. The limit of the solid solution range, $\text{Li}_{5.5}\text{PS}_{4.5}\text{Cl}_{1.5}$, exhibits particularly high Li-ion diffusivity and quadrupled ionic conductivity of $9.4 \pm 0.1 \text{ mS}\cdot\text{cm}^{-1}$ at room temperature (up to $12 \text{ mS}\cdot\text{cm}^{-1}$ for sintered materials, approaching the best benchmarks in the field). Its relatively good stability to lithium metal owing to the lack of easily reduced metals such as Ge, Sn and Si, and low-cost elements suggest this material is a good prospect as a solid-state electrolyte. Presented findings demonstrate that increasing the halide content of thiophosphate-based materials to weaken interactions between the mobile Li-ions and surrounding framework,

while increasing site disorder and lithium cation vacancy population to alter the energy landscape, is an important strategy to increase lithium-ion mobility in the accelerated search for new solid-state ion conductors – not only argyrodites.

Chapter 4 Chalcogenide Substituted Argyrodites



This section is reproduced in part from below manuscript:

Parvin Adeli, J. David Bazak, Jalil Assoud, Abhi Shyamsunder, Gillian R. Goward, and Linda F. Nazar. Correlating structural changes and transport properties in chalcogenide substituted Li-argyrodite superionic conductors, 2022.

Contribution: The NMR measurements and analysis in this chapter were performed by D. Bazak in Dr. G. Goward's lab at McMaster University. Single crystal measurements and refinements were carried out by Dr. J. Assoud (Crystallographer at UWaterloo). Li_2Se precursor was prepared in-house by Abhi Shyamsunder.

4.1 Introduction

Global communication was revolutionized by the discovery and application of the Li-ion rechargeable battery in consumer electronics such as cellular phones, tablets, laptops, and digital cameras. Our day-to-day life relies heavily on the energy storage capability and safety of these electronics.^[3,107] Current widely used commercial Li-ion batteries can pose alarming safety hazards due to the flammable organic liquid electrolyte which can ignite as a consequence of overheating. This heralds the merits of safer battery chemistries such as all-solid-state Li batteries (ASSLBs) which have garnered immense attention within the scientific community.^[2] ASSLBs also enable direct stacking of cell units and decrease the inactive volume of a battery pack. One key challenge in deploying ASSBs is the design and fabrication of promising solid electrolytes that can accommodate the next-generation solid-state battery technology offering high ionic conductivity at room temperature and processability for grand scale fabrication. In the past couple of decades, the myriad of theoretical and experimental research endeavours has led to a set of design principles that should be considered while targeting a solid electrolyte that can potentially enhance the ionic conductivity and hence performance. Specifically, thiophosphates family has been the centre of attention among researchers for enabling high conductivities,^[55] a prominent member of which is the Li-argyrodites.^[56,69] The high mobility of Li⁺ ions in Li-argyrodites makes this class of materials a fascinating base for further in-depth studies to understand and design favourable structures for future solid-state electrolytes.^[75, 108-110]

It was previously reported that the presence of anions with higher polarizability in the argyrodite structure renders a material with correspondingly higher ionic conductivity,^[75,111] however, some studies found this to not always be the scenario.^[112] Our previous work demonstrated the drastic impact of surrounding anion framework on Li⁺ ion transport in the

argyrodite superionic conductors.^[108] This along with the theoretical predictions that chalcogen (Se and Te) substitution will enhance the ionic conductivity,^[113] inspired us to investigate the substitution of a larger anion in the S position in the cubic argyrodite structure $\text{Li}_6\text{PS}_5\text{Cl}$.

Selenium substitution for sulfur has been practiced in various lithium and sodium thiophosphate crystal structures previously; however, studies have been more focused on the latter, particularly on the Na_3PS_4 system.^[74,111,112,114-124] It was demonstrated that the weaker mobile-ion – Se interaction compared to mobile-ion – S interaction led to an increase in ionic conductivity.^[118] Aside from the higher polarizability of Se lessening the diffusion barrier,^[29] another hypothesis is that the larger ionic radius of Se (198 pm) compared to S (184 pm) could lead to an increase in the lattice volume and potentially enlarge the Li^+ ion diffusion path window, also resulting in better ionic conductivity.

Li_7PS_6 was reported for the first time in 1976 by Brice.^[125] Deiseroth *et al.* studied the full Se substitution on the S site for this phase in 2010 and discovered that the lattice parameter for the high-temperature phase increases from 9.993(1) Å for Li_7PS_6 to 10.475(1) Å for Li_7PSe_6 but they did not report ionic conductivity values for these phases.^[122] Later in 2013, Deiseroth and Wilkening probed Long-range Li^+ dynamics in the lithium argyrodite Li_7PSe_6 by spin-lattice relaxation NMR.^[126] At ambient temperature, the Li self-diffusion coefficient is approximately $1.3(8) \times 10^{-15} \text{ m}^2\text{S}^{-1}$. This points to a Li-ion conductivity in the order of $2 \times 10^{-6} \text{ S}\cdot\text{cm}^{-1}$ at 300 K.

Halide containing argyrodites $\text{Li}_6\text{PS}_5\text{X}$ (X: Cl, Br) derived from Li_7PS_6 have been a rising subject of highly conductive solid electrolyte scouting. $\text{Li}_6\text{PS}_5\text{Cl}$ has a cubic argyrodite structure with the space group $F\bar{4}3m$. In $\text{Li}_6\text{PS}_5\text{Cl}$ structure, three anion sites (denoted as Wyckoff 4a, 4c, 16e) exist that S could occupy. 16e sites are fully occupied by S^{2-} and, together with P (Wyckoff

4b), they form isolated PS_4^{3-} units. Wyckoff 4c is the free sulfur site and Cl/S^{2-} are disordered over 4a and 4c sites. Zeier *et al.* studied Se substitution for $\text{Li}_6\text{PS}_{5-x}\text{Se}_x\text{Br}$ ($0 \leq x \leq 1$) and observed that transport behavior is not impacted within this range of Se substitution.^[112] The same group monitored the transport behavior in $\text{Li}_6\text{PS}_{5-x}\text{Se}_x\text{I}$ ($x = 0, 1, 2, 3, 4, 5$) and noticed a linear increase in the ionic conductivity from $0.0025 \text{ mS}\cdot\text{cm}^{-1}$ ($x = 0$) to $0.28 \text{ mS}\cdot\text{cm}^{-1}$ ($x = 5$) upon Se substitution.^[114]

Here the effect of Se substitution is investigated for S in the $\text{Li}_6\text{PS}_5\text{Cl}$ argyrodite solid electrolytes. Solid solution series $\text{Li}_6\text{PS}_{5-x}\text{Se}_x\text{Cl}$ ($x = 0, 0.5, 0.75, 1, 2, 2.5, 4, 5$) were synthesized and the structure of these materials characterized with single-crystal X-ray diffraction (XRD), synchrotron XRD and magic-angle spinning (MAS) nuclear magnetic resonance (NMR). Furthermore, transport properties were studied via Electrochemical Impedance Spectroscopy (EIS) and correlated to the structure. Structure refinement was utilized to study the effect of Se substitution on the previously reported disorder on 4a/4c sites for halide and chalcogen atoms as well as distinguish the $(\text{PS}_{4-n}\text{Se}_n)^{3-}$ moieties via Raman and ^{31}P MAS-NMR.

4.2 Material Synthesis and Characterization

Single crystals: Targeted compositions $\text{Li}_6\text{PS}_{5-x}\text{Se}_x\text{Cl}$ ($x = 0, 0.5, 0.75, 1, 2, 2.5, 4, 5$) were prepared in an argon-filled glovebox (MBraun, O_2 and $\text{H}_2\text{O} < 1.5 \text{ ppm}$). Binary precursors Li_2S powder (Sigma-Aldrich, 99.98%), LiCl anhydrous beads (Sigma-Aldrich, 99.9%), Li_2Se (prepared in-house) and elemental powder precursors Se (Sigma-Aldrich, 99.5%), S (Sigma-Aldrich, 99.9%) and P red (Sigma-Aldrich, 99%) were used as starting materials. Stoichiometric amounts of precursors were hand ground in an agate mortar for 10 minutes. Then the mixture was pelletized at 1.5 metric tons. The pellets were placed in glassy carbon crucibles and transferred to quartz tubes with an inner diameter of 13 mm. The quartz tubes were vacuum sealed with an

oxygen/acetylene torch. The glassy carbon and quartz tubes were preheated at 130°C overnight prior to use. For growing single crystals, the samples were heated to 620°C and held for 12 - 14 hours and then slowly cooled down to room temperature over a period of 99 hours. Heat treatments were carried out in a tube furnace. The air-sensitive products were retrieved in the argon-filled glovebox from which single crystals were picked out and mounted for single-crystal X-ray diffraction measurement.

Powder samples: Targeted $\text{Li}_6\text{PS}_{5-x}\text{Se}_x\text{Cl}$ compositions were prepared with the same solid-state route as described above, albeit with a shorter cooling step applied.

4.2.1 Single Crystal Characterization and Structure Refinement

A series of single crystals with different S:Se ratio of the compounds with the formula $\text{Li}_6\text{PS}_{5-x}\text{Se}_x\text{Cl}$ ($x = 0, 0.5, 0.75, 1, 2, 2.5, 4, 5$) were investigated for crystal structure determination. All samples are in form of colorless plates with the dimensions varying between $0.020 \times 0.080 \times 0.080 \text{ mm}^3$ and $0.020 \times 0.100 \times 0.180 \text{ mm}^3$. The X-ray single diffraction data were collected at 280K (to protect the integrity of the air-sensitive samples) using a BRUKER KAPPA diffractometer equipped with APEX II CCD detector, using a graphite-monochromated Mo-K α radiation. Owing to the air and moisture sensitivity of the crystals, they were mounted on glass fibres with Paratone-N oil protection then maintained under a flow of dry nitrogen using OXFORD Cryostream controller 700 at 280 K. The data were collected in ω and ϕ scan mode, with an increment of 0.3° . For a complete dataset with high resolution and small redundancy, an automatic Bruker APEX II suite strategy were used for the collection of the frame sets. The exposure times were between 10 and 60 seconds per frame. After the data collection, the unit cells were indexed and the data were corrected for Lorentz and polarization effects and a multi-scan absorption

correction were applied using SADABS (Bruker APEX II suite). The structure was solved using the direct method and refined by least-squares fitting incorporated in the SHELXTL package.

After obtaining the structure model with one phosphorus and three chalcogen atoms, the model was refined anisotropically and two Li sites were found in the rest of electron density. First the S:Se mixed occupancy with freely refined Li positions was conducted and the ratio were noted, then the same refinement was conducted again, but with Cl:Se mixed position and freely refined Li, with the ratio again noted. Taking into consideration the Cl contribution in the first S:Se mixed refinement, the Se occupancy was corrected and then fixed for further refinement. Since the samples were obtained as pure phases, the S:Cl ratio was fixed over the two $4a$ and $4c$ crystallographically chalcogen sites. The final refinement converged to very good R-value with the refined formula showing an over- or under-estimation of the Lithium content, due to the light Li atom in the presence of heavy element selenium or due to increase or decrease of the S:Cl ratio since both elements have comparable scattering. **Table 4.1** and **Table 4.2** summarize the crystallographic data, atomic coordinates, and bond distances of $x = 1$ and $x = 2.5$ materials.

4.2.2 Powder X-ray Diffraction

X-ray diffraction (XRD) measurement was performed with a PANalytical Empyrean instrument (45 kV voltage and 40 mA current) using Cu - $K\alpha$ radiation (1.5406 Å). For flat stage measurements, Kapton film was used to protect the sample from moisture. The sample for synchrotron XRD measurement ($\text{Li}_6\text{PS}_{4.25}\text{Se}_{0.75}\text{Cl}$) was loaded into a 0.3 mm diameter and 0.01 mm wall thickness capillary and sealed with epoxy inside the glove box under argon. The sample was measured at the CLS with a wavelength of 0.68954 Å (~18 keV). The diffraction pattern was refined using GSAS II software and single crystal data of $\text{Li}_6\text{PS}_{4.25}\text{Se}_{0.75}\text{Cl}$. The space group $F\bar{4}3m$ was used as a starting point for the refinement.

4.2.3 Raman Spectroscopy

Powder samples were pelletized inside an argon-filled glove box. The pellets were sandwiched between two glass slides and the edges were sealed with epoxy for handling outside glovebox. Raman spectra were recorded with Raman HORIBA HR800 spectrometer at an excitation of 514 nm (measurement time: 20 s, accumulation: 5).

Impedance Spectroscopy was carried out same as previous chapter i.e., powder samples were placed between two stainless steel rods (10 mm) and cold-pressed at 2 tons prior to measurements.

4.3 Results and Discussion

4.3.1 Structural Properties

Single crystals of $\text{Li}_6\text{PS}_{5-x}\text{Se}_x\text{Cl}$ ($x = 0.5, 0.75, 1, 2, 2.5, 4, 5$) argyrodite solid electrolytes were grown via solid-state route. Single crystal diffraction data were collected for all materials and lattice parameters were extracted from refinement which are presented in **Figure 4.1a**. The lattice

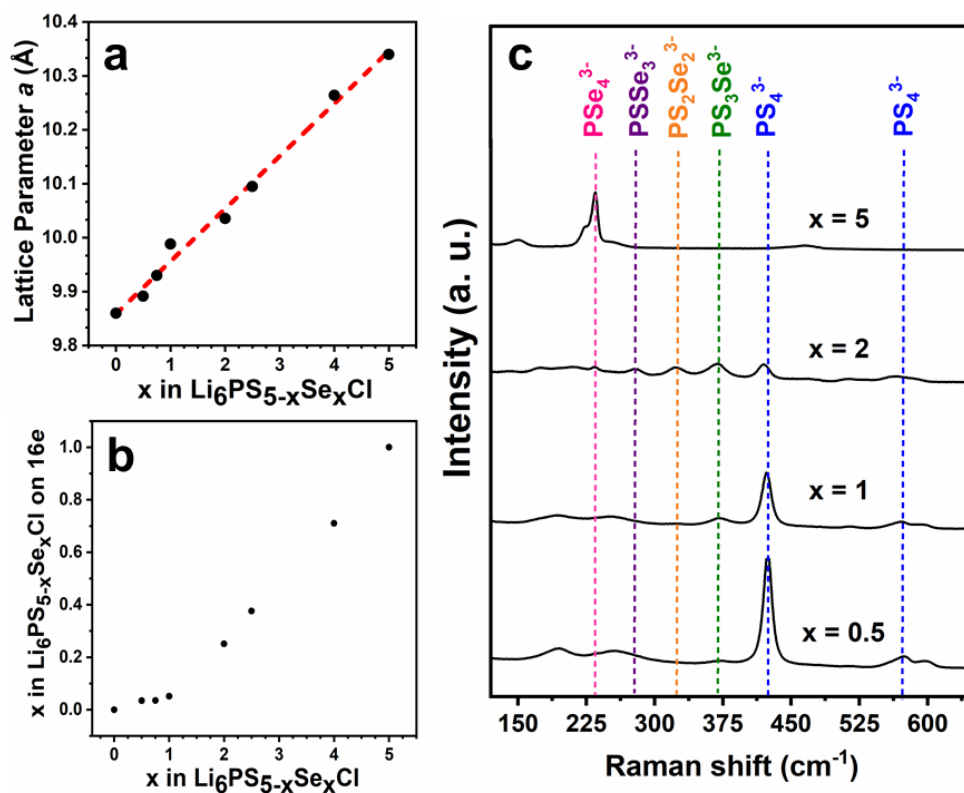


Figure 4.1 a) Lattice parameter of solid solution series $\text{Li}_6\text{PS}_{5-x}\text{Se}_x\text{Cl}$ vs x . The black points represent data extracted from refinement of single crystal X-ray diffraction. The red dotted line denotes the linear fit. b) Se occupancies on Wyckoff 16e site. c) Raman spectra for $x = 0.5, 1, 2$ and 5 . $\text{P}(\text{S}_{4-x}\text{Se}_x)^{3-}$ peaks are identified with different colors of dashed lines.

parameters obey Vegard's law and follow a linear increase upon increasing Se content. The trend for Se occupancy on the 16e site is displayed in **Figure 4.1b**. This trend indicates that for small

amounts of Se doping ($x \leq 1$), Se prefers to occupy the $4a$ or $4c$ sites compared to the tetrahedral site ($16e$). Upon introducing higher amounts of Se doping, this site preference disappears. This behavior is corroborated in the comparative Raman studies which were carried out for $x = 0.5, 1, 2, 5$ shown in **Figure 4.1c**. As the Se amount increases, the PS_4^{3-} shift ($\sim 420 \text{ cm}^{-1}$) gradually disappears. Going from $x = 0$ to $x = 1$ and then to $x = 2$, the rise in the intensity of $\text{PS}_3\text{Se}^{3-}$ vibrational mode is evident and for $x = 5$, only the peak corresponding to PSe_4^{3-} is observed as expected.

The structure of $\text{Li}_6\text{PS}_4\text{SeCl}$ obtained from refinement against the single crystal X-ray diffraction data is displayed in **Figure 4.2a**. Corresponding structural parameters are presented in **Table 4.1**. Similar to $\text{Li}_6\text{PS}_5\text{Cl}$, $\text{Li}_6\text{PS}_4\text{SeCl}$ adopts the cubic $\bar{F}43m$ space group where Li sites form cage-like

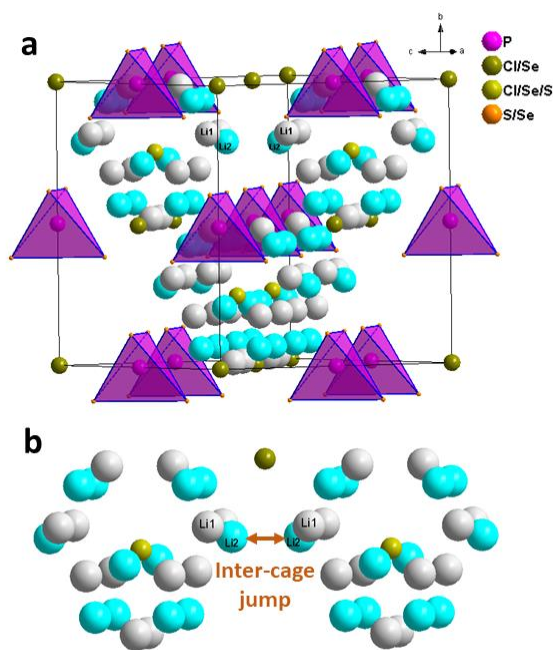


Figure 4.2 a) Crystal structure of $\text{Li}_6\text{PS}_4\text{SeCl}$ obtained from refinement against the single crystal X-ray diffraction data. b) Li cages formed by Li1(48h) (grey) and Li2(48h) (turquoise) sites, Li2(48h) sites introduce a new Li2(48h)-Li2(48h) inter-cage jump pathway.

geometries. In the conventional $\text{Li}_6\text{PS}_5\text{X}$ model, three Li^+ -ion jumps are feasible, namely: intracage ($48h$ - $48h$) hops, doublet hops ($48h$ - $24g$ - $48h$) and intercage hops.^[75] Refinement results for $\text{Li}_6\text{PS}_4\text{SeCl}$ suggest that two $\text{Li}(48h)$ sites are present (**Figure 4.2b**) and the new Li sites reside between the conventional intracage jump sites as previously observed in the thioantimonate Li-argyrodites.^[137] For $\text{Li}_6\text{PS}_5\text{Cl}$, the intercage jump $\text{Li1}(48h)$ - $\text{Li1}(48h)$ distance was determined to be 2.88 Å while for $\text{Li}_6\text{PS}_4\text{SeCl}$ this value is 2.85 Å for $\text{Li1}(48h)$ - $\text{Li1}(48h)$ and 1.92 Å for the new intercage jump $\text{Li2}(48h)$ - $\text{Li2}(48h)$ pathway.

Table 4.1 Atomic coordinates, occupation factor, and equivalent isotropic displacement parameters of $\text{Li}_6\text{PS}_4\text{SeCl}$ obtained from single-crystal X-ray diffraction data refinement at 280 K (space group $F\bar{4}3m$). The calculated formula is $\text{Li}_{6.12}\text{PS}_4\text{SeCl}$.

Atom	Wyckoff Site	x	y	z	SOF	$U_{\text{eq}}(\text{Å}^2)$
P(1)	4b	1/2	1/2	1/2	1	0.026(1)
Cl(1)	4a	0	0	0	0.5266	0.040(1)
Se(1)	4a	0	0	0	0.4735	0.040(1)
Cl(2)	4c	1/4	1/4	1/4	0.4735	0.024(1)
S(2)	4c	1/4	1/4	1/4	0.2062	0.024(1)
Se(2)	4c	1/4	1/4	1/4	0.3207	0.024(1)
S(3)	16e	0.6191(1)	0.6191(1)	0.6191(1)	0.949(3)	0.036(1)
Se(3)	16e	0.6191(1)	0.6191(1)	0.6191(1)	0.051(3)	0.036(1)
Li(1)	48h	0.1842(10)	0.1842(10)	0.0177(14)	0.39(2)	0.067(6)
Li(2)	48h	0.068(4)	0.215(5)	0.068(4)	0.12(3)	0.080(20)

Compared to $\text{Li}_6\text{PS}_4\text{SeCl}$, one $\text{Li}(48h)$ site was observed in $\text{Li}_6\text{PS}_{2.5}\text{Se}_{2.5}\text{Cl}$ (refined composition of $\text{Li}_{5.76}\text{PS}_{2.5}\text{Se}_{2.5}\text{Cl}$ in the cubic $F\bar{4}3m$ space group, **Table 4.2**). Refinement of single crystal X-ray diffraction data for targeted $\text{Li}_6\text{PSe}_5\text{Cl}$ led to a calculated phase of $\text{Li}_{6.42}\text{PSe}_{5.44}\text{Cl}_{0.56}$. To confirm this observation, the synthesis was repeated several times and single crystals were

picked out of different batches. Corresponding refinement results revealed that only a fraction of Cl can be present in the parent structure when full substitution of S by Se is attempted. This is linked to the smaller size of the Cl lattice given that full Se substitution is feasible for iodine argyrodite phases.^[114]

Table 4.2 Atomic coordinates, occupation factor, and equivalent isotropic displacement parameters of $\text{Li}_6\text{PS}_{2.5}\text{Se}_{2.5}\text{Cl}$ obtained from single-crystal X-ray diffraction data refinement at 280 K (space group $F\bar{4}3m$). The calculated formula is $\text{Li}_{5.76}\text{PS}_{2.5}\text{Se}_{2.5}\text{Cl}$.

Atom	Wyckoff Site	x	y	z	SOF	U_{eq} (\AA^2)
P(1)	4b	1/2	1/2	1/2	1	0.028(1)
Cl(1)	4a	0	0	0	0.5592	0.036(1)
Se(1)	4a	0	0	0	0.4409	0.036(1)
Cl(2)	4c	1/4	1/4	1/4	0.4423	0.027(1)
Se(2)	4c	1/4	1/4	1/4	0.5578	0.027(1)
S(3)	16e	0.6213(1)	0.6213(1)	0.6213(1)	0.6242	0.046(1)
Se(3)	16e	0.6213(1)	0.6213(1)	0.6213(1)	0.3758	0.046(1)
Li(1)	48h	0.177(3)	0.177(3)	0.018(5)	0.48(9)	0.100(30)

Powder synchrotron diffraction data were collected for $\text{Li}_6\text{PS}_{4.25}\text{Se}_{0.75}\text{Cl}$. Rietveld refinement against synchrotron data confirmed a pure phase (**Figure 4.3a**). Powder x-ray diffraction data were collected for $x = 1, 2,$ and 2.5 which are shown in **Figure 4.3b**, **Figure 4.4**

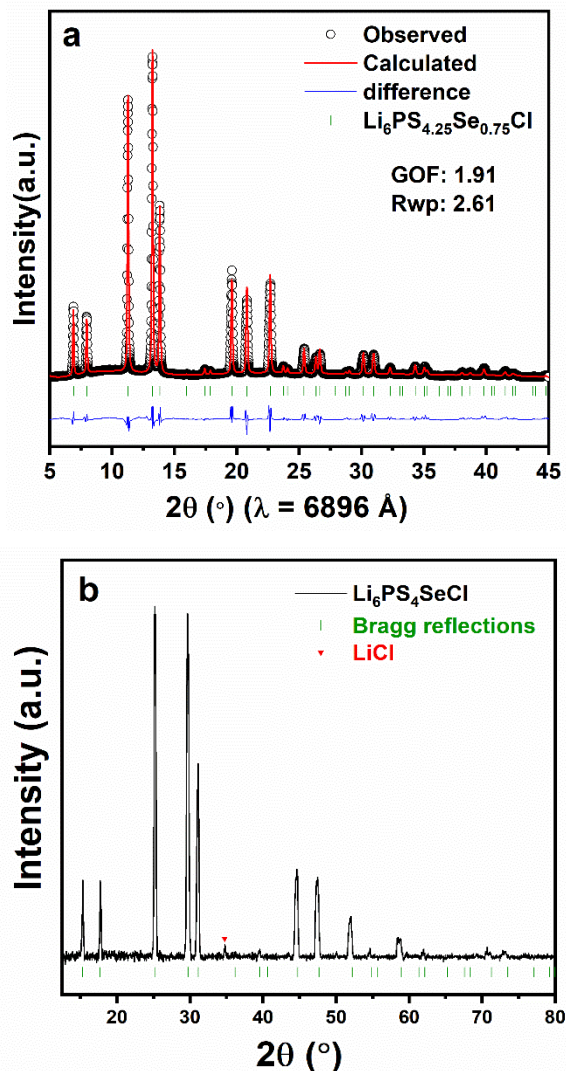


Figure 4.3 a) Rietveld refinement for $\text{Li}_6\text{PS}_{4.25}\text{Se}_{0.75}\text{Cl}$ refined against synchrotron data. The hollow black circles show the observed pattern, and the red solid line denotes the calculated pattern. The difference map is depicted in blue, and the Bragg reflections are displayed in green. b) XRD pattern (flat stage) of $\text{Li}_6\text{PS}_4\text{SeCl}$. Minority LiCl was observed which is indicated with red triangle.

and **Figure 4.5**. Corresponding XRD patterns demonstrate an almost pure phase with a very small amount of impurities that is not expected to influence total ionic conductivity.

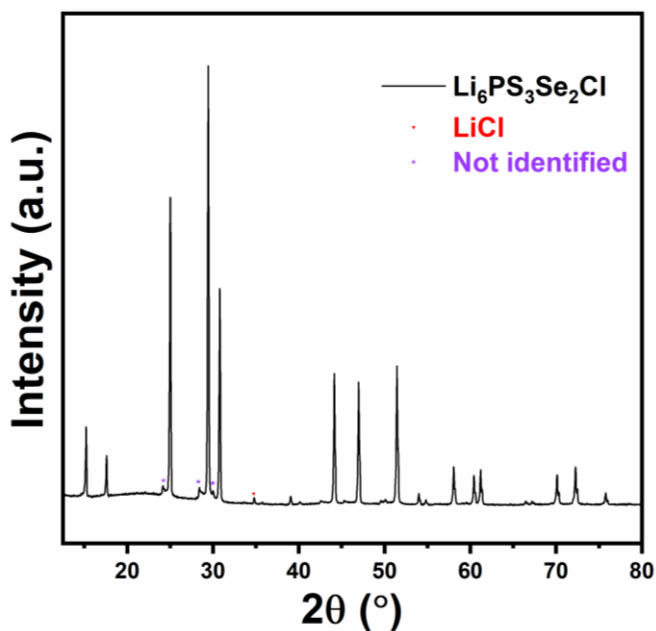


Figure 4.4 XRD pattern (overnight capillary) of $\text{Li}_6\text{PS}_3\text{Se}_2\text{Cl}$ phase. Minority impurity peaks are shown with red triangle (LiCl) and purple stars (not identified).

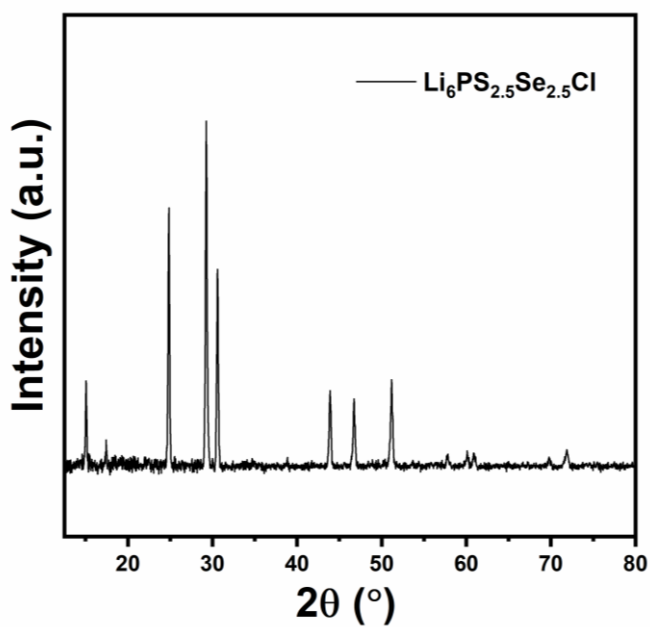


Figure 4.5. XRD pattern (flat stage) of pure $\text{Li}_6\text{PS}_{2.5}\text{Se}_{2.5}\text{Cl}$ phase.

4.3.2 Transport Properties

The argyrodite powders were pressed into pellets for determining ionic conductivities from electrochemical impedance spectroscopy. **Figure 4.6a** shows the trend in ionic conductivity and **Figure 4.6b, c and d** depict the Nyquist plots at room temperature used to extract resistance values for conductivity. For $x = 5$, the impedance data was fit to an equivalent circuit consisting of one parallel CPE/resistor in series with a CPE (see **Table 4.3** for fit parameters) which is typically the circuit used for solid electrolytes (conductive and capacitive behavior) plus polarisation component at room temperature. This model did not lead to a good fit for $x = 4$ and the impedance response was fit to an equivalent circuit consisting of two CPE/resistor in series with a CPE (**Table 4.4**). The second CPE/resistor is ascribed to grain boundary processes given the much higher capacitance.^[127]

All the samples except $x = 5$, exhibit an ionic conductivity greater than 1 mS.cm^{-1} . $\text{Li}_6\text{PS}_4\text{SeCl}$ exhibits the highest ionic conductivity among the studied materials in this work and the previously reported $\text{Li}_6\text{PS}_{5-x}\text{Se}_x(\text{Br/I})$.^[112,114] It was noted that unlike the bromide phases, the ion transport is indeed impacted by Se substitution in the chloride phases. The measured materials exhibited an interesting behaviour as a function of x , with an initial sharp increase peaking at $x = 1$, followed by a more gradual decline from $x = 2$ to $x = 4$, and then a dramatic drop-off for $x = 5$. This trend can be readily correlated to the evolution of the structure upon increased Se substitution.

Going from the parent phase to $x = 0.5$, the increase in the volume of the unit cell (from $V = 958.53 \text{ \AA}^3$ to 967.83 \AA^3) broadens the Li-ion diffusion window and could contribute to a small increase in the ionic conductivity, which continues on going to $x = 1$, reaching a maximum of 4.7 mS.cm^{-1} at this substitution level. The ionic conductivity then drops to 2.8 mS.cm^{-1} for $X = 2.5$.

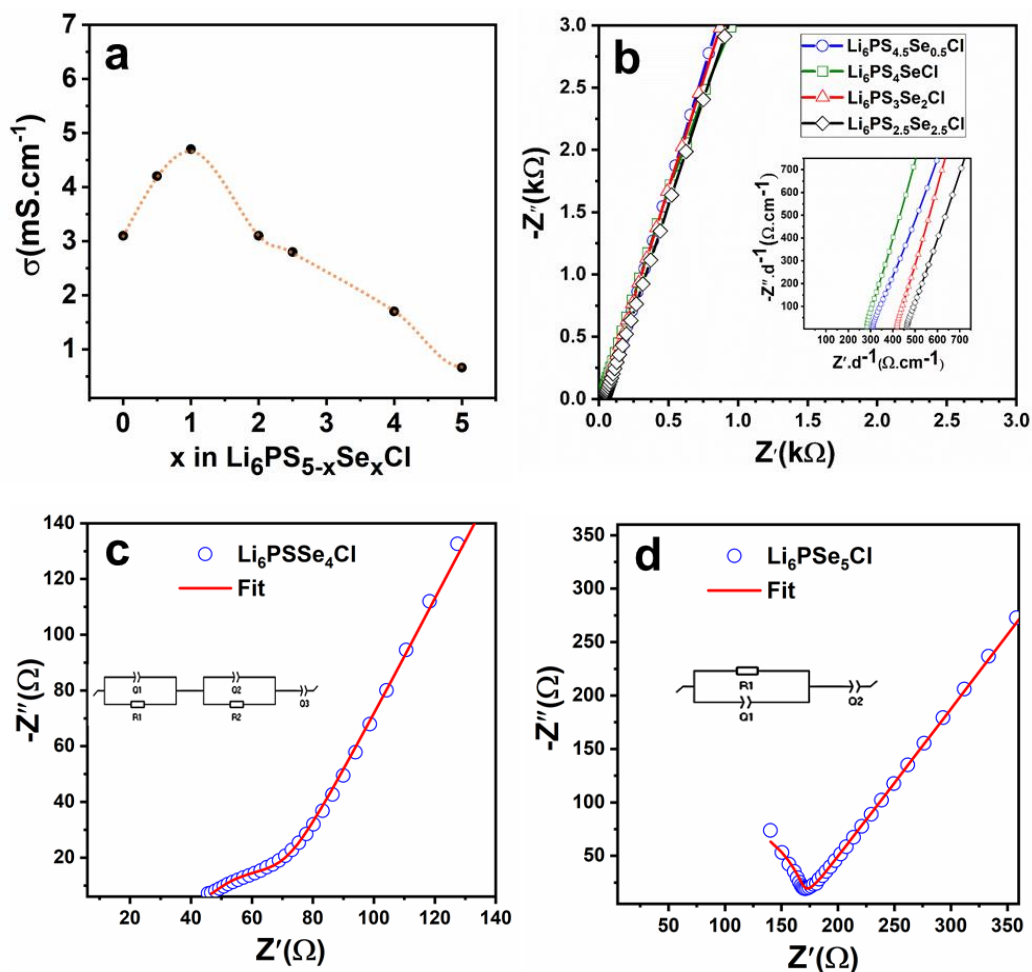


Figure 4.6. a) Room temperature (RT) ionic conductivity values for $\text{Li}_6\text{PS}_{5-x}\text{Se}_x\text{Cl}$ ($x = 0, 0.5, 1, 2, 2.5, 4, 5$); b) Impedance plots for ($x = 0.5, 1, 2, 2.5$), inset denotes enlarged view at high frequencies where the RT impedance values are normalized to the cold-pressed pellet thickness; c) Nyquist impedance plot and corresponding fit for $x = 4$ with the respective equivalent circuit. Fit parameters are detailed in **Table 4.4**; d) Nyquist impedance plot and fit for $x = 5$ with the corresponding equivalent circuit. Fit parameters are presented in **Table 4.3**.

Table 4.3 Fit parameters of the impedance data of $\text{Li}_6\text{PSe}_5\text{Cl}$ at room temperature.

Equivalent circuit =	$\text{R1/Q1} + \text{Q2}$
R1	164.8 Ω
Q1	0.452e-9 $\text{F.s}^{(a-1)}$
a1	0.995
Q2	21.44e-6 $\text{F.s}^{(a-1)}$
a2	0.602

Table 4.4 Fit parameters of the impedance data of $\text{Li}_6\text{PS}_4\text{SeCl}$ at room temperature.

Equivalent circuit =	$\text{R1/Q1} + \text{R2/Q2} + \text{Q3}$
R1	44.44 Ω
Q1	37.9e-11 $\text{F.s}^{(a-1)}$
a1	0.980
R2	22.05 Ω
Q2	8.26e-7 $\text{F.s}^{(a-1)}$
a2	0.825
Q3	1.38e-5 $\text{F.s}^{(a-1)}$
a3	0.716

This increase and subsequent decrease are correlated to a change in the distribution of Li sites present in the structure; two Li(48*h*) sites were realized in $x = 1$ compared with only a single Li site in $x = 2.5$, as determined from single-crystal X-ray diffraction data refinement. The presence of new Li2(48*h*) sites between the intracage jumps facilitate the Li⁺ ion conduction by acting as local minima^[137] and the new shorter intercage jump (Li2(48*h*)-Li2(48*h*) diffusion pathway) is beneficial for long range Li⁺ ion diffusion. This is in accord with previous studies that suggested Li redistribution i.e., partial Li occupation in sites other than the conventional structural model 48*h* sites promotes fast Li ion diffusion in Li-argyrodites.^[128,138] Reflecting on the ionic conductivity trend, our results imply that after a certain threshold, further increase in the volume of the cell leads to longer intercage hopping distances for Li ions (3.00 Å for $x = 5$) and, together with the disappearance of the second Li site, eventually reduces the ionic conductivity.

The $\text{Li}_6\text{PS}_4\text{SeCl}$ and $\text{Li}_6\text{PS}_{2.5}\text{Se}_{2.5}\text{Cl}$ phases were further studied with ^7Li MAS-NMR, which buttressed our finding from refinement regarding the number of Li sites. Li site occupancy distribution extracted from the refinements and deconvolution of the NMR peaks (**Figure 4.7**) are presented in **Table 4.5**. The ratios obtained from refinement are in good accord with the ^7Li MAS-NMR peak ratios. Based on a comparison of the relative signal proportions to the refinement data, the peak at 1.93 ppm in the $x = 1$ spectrum is assigned to Li(1), while Li(2) is the minor component at a shift of 2.30 ppm.

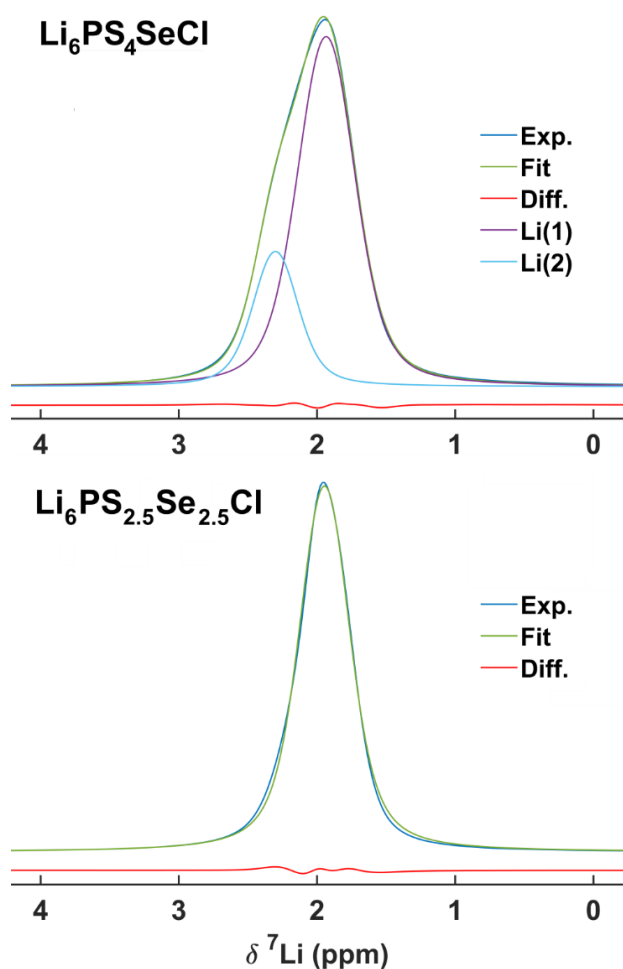


Figure 4.7 ^7Li MAS-NMR for $\text{Li}_6\text{PS}_4\text{SeCl}$ and $\text{Li}_6\text{PS}_{2.5}\text{Se}_{2.5}\text{Cl}$ at 25 kHz and 25°C, demonstrating a two-component fit for the former, while the latter is well-fit by a single Gaussian-Lorentzian line shape.

Table 4.5 Li site distribution extracted from ^7Li NMR and refinement of single crystal X-ray diffraction.

^7Li NMR	$\text{Li}_6\text{PS}_4\text{SeCl}$ Integral	Signal Fraction	$\text{Li}_6\text{PS}_{2.5}\text{Se}_{2.5}\text{Cl}$
Li(1)	3.232	0.764	
Li(2)	0.999	0.236	
	4.232		
XRD	$\text{Li}_6\text{PS}_4\text{SeCl}$		$\text{Li}_6\text{PS}_{2.5}\text{Se}_{2.5}\text{Cl}$
Li(1)	0.39	0.76	0.48
Li(2)	0.12	0.24	-
	0.51		

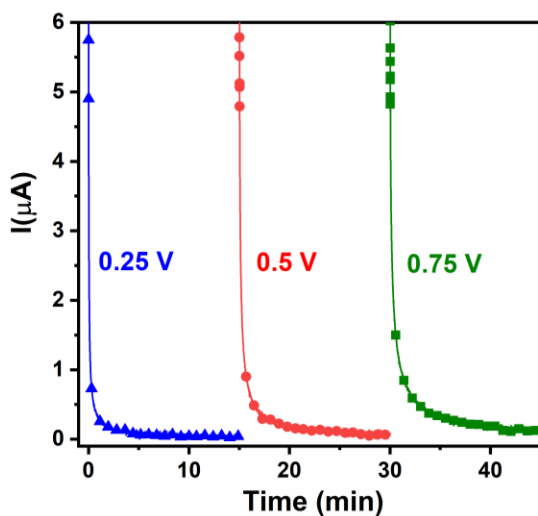


Figure 4.8 DC polarization for $x = 1$ material at 0.25, 0.5 and 0.75 V.

Electronic conductivity ($1.1 \times 10^{-7} \text{ S.cm}^{-1}$) was measured via DC polarization for $x = 1$ (highest conductive phase) and the extracted value verified that the ionic conduction is dominant in this material (**Figure 4.8**).

4.3.3 ^{31}P MAS-NMR

The $x = 1$ and $x = 2.5$ materials were further studied by ^{31}P MAS-NMR. The corresponding spectra are presented in **Figure 4.9**. The substitutional pattern observed is in great agreement with the substitutional pattern in the Raman spectrum of $x = 2$ (**Figure 4.1**) showing a much wider range of thiophosphate Se-substitution possibilities for $x = 2.5$, while either zero (PS_4^{3-}) or one (PSeS_3^{3-}) is preferred in $x = 1$.

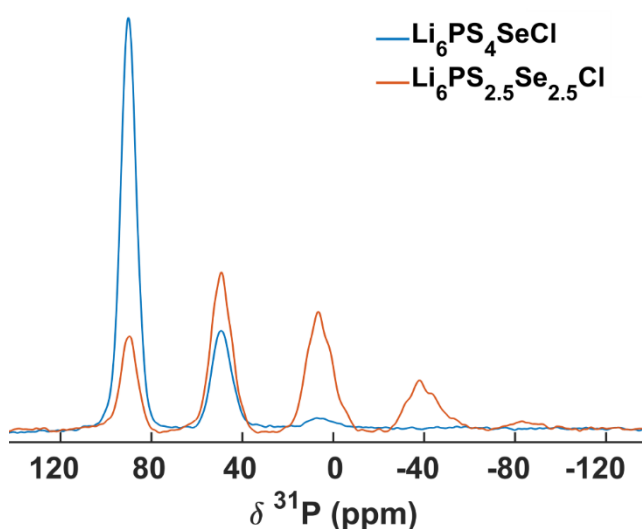


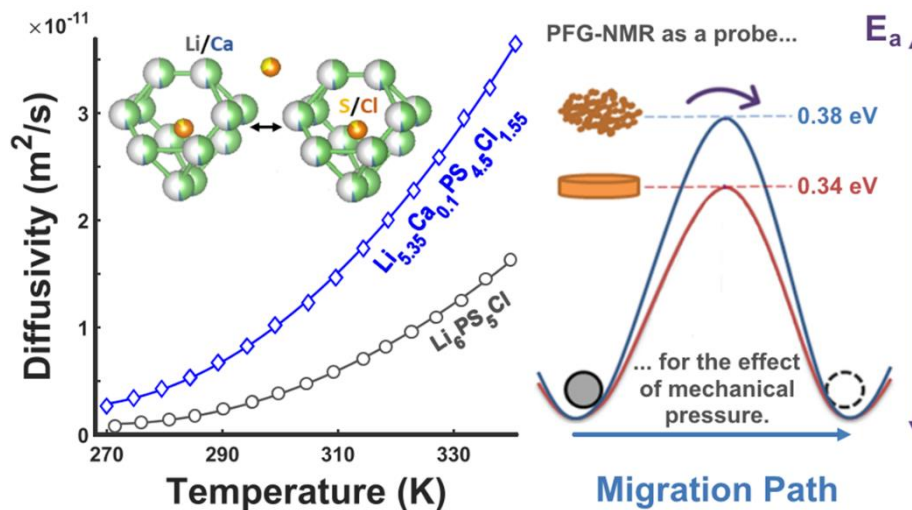
Figure 4.9 ^{31}P MAS-NMR for the $\text{Li}_6\text{PS}_4\text{SeCl}$ and $\text{Li}_6\text{PS}_{2.5}\text{Se}_{2.5}\text{Cl}$ compositions at 25 kHz and 25 °C. The lineshapes exhibit a cascading pattern indicative of differing levels of Se substitution on the PS_4^{3-} tetrahedra, with PS_4^{3-} being the dominant coordination for $x = 1$, whereas $\text{PS}_3\text{Se}^{3-}$ is the most-represented coordination for $x = 2.5$.

4.4 Conclusion

The targeted $\text{Li}_6\text{PS}_{5-x}\text{Se}_x\text{Cl}$ argyrodite compositions were obtained as the primary product and contained colourless single crystals which were investigated via single crystal X-ray diffraction measurements. Contrary to Li_7PSe_6 , $\text{Li}_6\text{PS}_{5-x}\text{Se}_x\text{Cl}$ crystallizes in the cubic high temperature form at room temperature. The effect of Se substitution on the previously reported

disorder on $4a/4c$ sites for halide and chalcogen atoms was investigated and the substitutional patterns of the $(\text{PS}_{4-n}\text{Se}_n)^{3-}$ moieties was distinguished via Raman and ^{31}P solid-state MAS NMR. Furthermore, the ionic conductivity was studied via EIS and correlated to the evolution of the structure with increasing Se substitution. In the explored compositional space, $\text{Li}_6\text{PS}_4\text{SeCl}$ exhibited the highest ionic conductivity of $4.7 \text{ mS}\cdot\text{cm}^{-1}$. This was attributed to the change in the lithium substructure, identification of a new Li (48h) site and shorter $\text{Li}_2(48\text{h})\text{-Li}_2(48\text{h})$ interchange conduction pathway. The insights gathered on the interplay between structure and ion transport for selenide-based argyrodite compositions offer a helpful new avenue for designing and understanding novel superionic solid electrolytes.

Chapter 5 Cation Doped and Dual Modified Argyrodites



This section is reproduced in part with permission from American Chemical Society:

Parvin Adeli, J. David Bazak, Ashfia Huq, Gillian R. Goward, and Linda F. Nazar. Influence of aliovalent cation substitution and mechanical compression on Li-ion conductivity and diffusivity in argyrodite solid electrolytes, *Chem. Mater.* 33, 2021, 146-157.

Contribution: The NMR measurements and analysis in this chapter were performed by D. Bazak in Dr. G. Goward's lab at McMaster University. Only a portion of the NMR data is presented here. For detailed NMR method and results, refer to the corresponding publication.

5.1 Calcium and Other Aliovalent Cation Doped Argyrodites

5.1.1 Introduction

Several theoretical and experimental studies on anion site substitution have been reported for the argyrodite class of materials,^[75,76,97,112] albeit cation substitution on the Li site and dual modification are areas that have not been well explored which inspired this study. Recently, Schneider *et al.* reported stabilization of high-temperature Li_7PS_6 by doping the Li site with iron to form $\text{Li}_6\text{Fe}_{0.5}\text{PS}_6$, the latter exhibits a relatively low ionic conductivity of $1.4 \times 10^{-4} \text{ S.cm}^{-1}$.^[129] While preparing this thesis, other groups suggested partial substitution of $\text{Al}^{3+}/\text{B}^{3+}$ on the Li site for $\text{Li}_6\text{PS}_5\text{X}$ (X=Cl, Br) on the basis of XRD refinements. Among their reported compositions, $\text{Li}_{5.4}\text{Al}_{0.2}\text{PS}_5\text{Br}$ exhibited the highest room temperature conductivity of 2.4 mS.cm^{-1} .^[130] Another study showed that Y^{3+} -doped $\text{Li}_6\text{PS}_5\text{Cl}$ exhibits negligible difference in room temperature ionic conductivity *vis a vis* $\text{Li}_6\text{PS}_5\text{Cl}$ and that YCl_3 is exsolved at the grain boundary.^[131] A patent application claims compositions in the argyrodite lattice derived by substitution of monovalent alkali cations for Li^+ .^[132] While the reason for the substitution of a monovalent ion is not clear, substitution of a divalent cation with a similar radius to Li^+ , such as Mg^{2+} or Ca^{2+} , is strongly motivated by the increase in vacancy concentration on the lithium site. As it is demonstrated later in this chapter, that is responsible for more than a doubling in the ionic conductivity compared to the parent phase, when coupled with a small increase in the $\text{Cl}^-/\text{S}^{2-}$ ratio. The structure and ionic transport properties were probed via neutron powder diffraction (NPD), electrochemical impedance spectroscopy (EIS), ^7Li and ^{31}P magic-angle spinning (MAS) and pulsed-field gradient (PFG) NMR. This study, therefore, helps develop a better understanding of the fundamental structure-property interplays that govern the ionic transport and lead to enhanced performance in this class of materials.

So far, the majority of the Li-argyrodite solid electrolytes have been synthesized by extensive mechanical milling of the solid precursors followed by heat treatment.^[69,133-135] Even the recently reported direct solid-state route by Wagemaker *et al.* utilized a short ball milling step and a 10 h long heat treatment.^[80] Ball-milling consumes a lot of energy and prolongs the preparation time significantly. Recently Zeier *et al.* prepared their highly conductive argyrodite ($\text{Li}_{6+x}\text{P}_{1-x}\text{Ge}_x\text{S}_5\text{I}$) via hand grinding; however, the following heat treatment was two weeks long.^[92] In this chapter, all the reported argyrodite compositions $\text{Li}_{6-2y}\text{Ca}_y\text{PS}_5\text{Cl}$ ($y = 0, 0.05, 0.1, 0.15, 0.2$), $\text{Li}_{6-x-2y}\text{Ca}_y\text{PS}_{5-x}\text{Cl}_{1+x}$ ($x = 0.25, y = 0.1; x = 0.25, y = 0.15; x = 0.375, y = 0.1; x = 0.5, y = 0.1$), $\text{Li}_{6.1-x-2y}\text{Ca}_y\text{PS}_{5.05-x}\text{Cl}_{1+x}$ ($x = 0.55, y = 0.1$) and $\text{Li}_{6-x-3y}\text{M}_y\text{PS}_{5-x}\text{Cl}_{1+x}$ (M: Al or Ga) ($y = 0.05; y = 0.1; y = 0.15; y = 0.2; x = 0.15, y = 0.1; x = 0.25, y = 0.1; x = 0.35, y = 0.1; x = 0.25, y = 0.2$) were prepared by quick hand grinding (15 min) of the precursors followed by a short heat treatment (5 h) at 550 °C. This rapid technique saves a great deal of energy and time.

5.1.2 Material Synthesis and Characterization

All material preparations for $\text{Li}_{6-2y}\text{Ca}_y\text{PS}_5\text{Cl}$ ($y = 0, 0.05, 0.1, 0.15, 0.2$), $\text{Li}_{6-x-2y}\text{Ca}_y\text{PS}_{5-x}\text{Cl}_{1+x}$ ($x = 0.25, y = 0.1; x = 0.25, y = 0.15; x = 0.375, y = 0.1; x = 0.5, y = 0.1$), $\text{Li}_{6.1-x-2y}\text{Ca}_y\text{PS}_{5.05-x}\text{Cl}_{1+x}$ ($x = 0.55, y = 0.1$) and $\text{Li}_{6-x-3y}\text{M}_y\text{PS}_{5-x}\text{Cl}_{1+x}$ (M: Al and Ga, $y = 0.05, 0.1, 0.2$ ($x = 0$); $x = 0.15, y = 0.1, x = 0.25, y = 0.1; x = 0.35, y = 0.1; x = 0.25, y = 0.2$) were performed in an argon-filled glovebox (MBraun, O_2 and H_2O content below 1 ppm). Stoichiometric amounts of the precursors lithium sulfide (Li_2S , Alfa Aesar, 99.9%), calcium sulfide (CaS , Alfa Aesar, 99%), phosphorus pentasulfide (P_2S_5 , Sigma-Aldrich, 99%), lithium chloride anhydrous beads (LiCl , Sigma-Aldrich, 99.9%), aluminum sulfide (Al_2S_3 , Sigma-Aldrich, 98%) and gallium (III) sulfide (Ga_2S_3 , Alfa Aesar, 99.99%) for corresponding compositions were

hand ground in an agate mortar for 15 minutes. The ground mixture with a typical weight of 0.5 gram was pelletized in a 13 mm die at 2 metric tons. The resulting pellets were transferred to quartz ampules which were sealed under vacuum. Glassy carbon crucibles were used to avoid direct contact of the pellets with the quartz ampules. Quartz ampules (inner diameter of 13mm and length of 8 cm) were preheated for one day at 300°C to avoid traces of water meddling in the reaction. The heat treatments were carried out at 550°C for 5 hours in a tube furnace with a rate of 0.5°C/min. Subsequently, the air sensitive products were ground, loaded and sealed in a 0.3 mm diameter quartz capillary for powder X-ray diffraction (XRD) measurements. The XRD patterns were measured overnight on a PANalytical Empyrean X-ray diffractometer applying Cu $\kappa\alpha$ radiation (1.5406 Å). The applied voltage and current were 45 kV and 40 mA respectively. Patterns were recorded in Debye-Scherrer setup and HighScore Plus software was used to identify the peaks. Time-of-flight (TOF) neutron diffraction data were collected on POWGEN at the SNS at ORNL (center λ : 1.5 Å, d-spacing over the range of 0.50097 - 13.0087 Å) at ambient temperature. The program GSAS II was used for Rietveld refinement, and the $\text{Li}_6\text{PS}_5\text{Cl}$ structure in the space group $F\bar{4}3m$ was used as a starting point for the refinement. The P and S occupancies on the $4b$ and $16e$ sites were fixed at their stoichiometric values. The atomic coordinates and atomic displacement parameters (U_{iso}) were restrained to be the same for the shared sites S1 and Cl1 (and for S2 and Cl2). The sum of occupancies was set to one for the shared sites ($\text{Occ}(\text{S1})+\text{Occ}(\text{Cl1})=1$ and $\text{Occ}(\text{S2})+\text{Occ}(\text{Cl2})=1$), and the atomic coordinates were restrained to be the same for Li and Ca on the $48h$ site. All other parameters were subsequently refined.

Scanning Electron Microscopy (SEM) and Energy Dispersive X-ray (EDX) Analysis

A Zeiss Leo 1530 FESEM (with EDX detector) was utilized for microstructural observation of the materials as well as elemental analysis. As the materials were not stable under

prolonged electron beam illumination, an acceleration voltage of 15 kV, with an acquisition time of 1 minute was used for EDX measurements.

Electrochemical Impedance Spectroscopy (EIS)

EIS was employed to obtain the ionic conductivities. Powder samples were sandwiched between two stainless steel rods (diameter of 10 mm) and cold-pressed at 2 tons by a uniaxial hydraulic press to give pellets between 0.5 to 1.1 mm thick. EIS measurements were carried out by sandwiching the pellets between two indium foils at 100 mV and in the frequency range of 1 MHz to 100 mHz at 298 K using a VMP3 potentiostat/galvanostat (Bio-logic). For temperature-dependent conductivity measurements, impedance spectra were recorded in the frequency range of 35 MHz to 100 mHz with the MTZ-35 impedance analyzer (Bio-Logic) controlled by MT-LAB (Bio-Logic) software from 298 K to 338 K at 5 K intervals. The EIS measurement for $x = 0.5$, $y = 0.1$ was performed at 273 K by immersing the sealed EIS cell in a cooling bath and waiting until equilibrium was achieved. Data analysis was performed using the EC-Lab software and the activation energy was determined from the slope of the Arrhenius plot.

5.1.3 Results and Discussion

Compositions varying only in Ca content (standard). Targeted compositions $\text{Li}_{6-2y}\text{Ca}_y\text{PS}_5\text{Cl}$ ($y = 0, 0.05, 0.1, 0.15$) were prepared. The XRD patterns for ($y = 0, 0.1, 0.15$) are shown in **Figure 5.1**. These argyrodites show a very small amount of impurities (< 1.5 wt%; see **Figure 5.2a** for quantitative Rietveld refinement of the XRD data and **Figures Figure 5.4, Figure 5.6, Figure 5.7** for quantitative Rietveld refinements of NPD data) which are not likely to impact the ionic conductivity. Attempts to increase the Ca^{2+} fraction to $y = 0.2$ led to the rise of Li_3PS_4 and $\text{CaP}_4\text{O}_{11}$ impurities (see XRD pattern in **Figure 5.3**) and a decrease in the ionic conductivity, indicating that $y = 0.15$ is the limit of solid solubility.

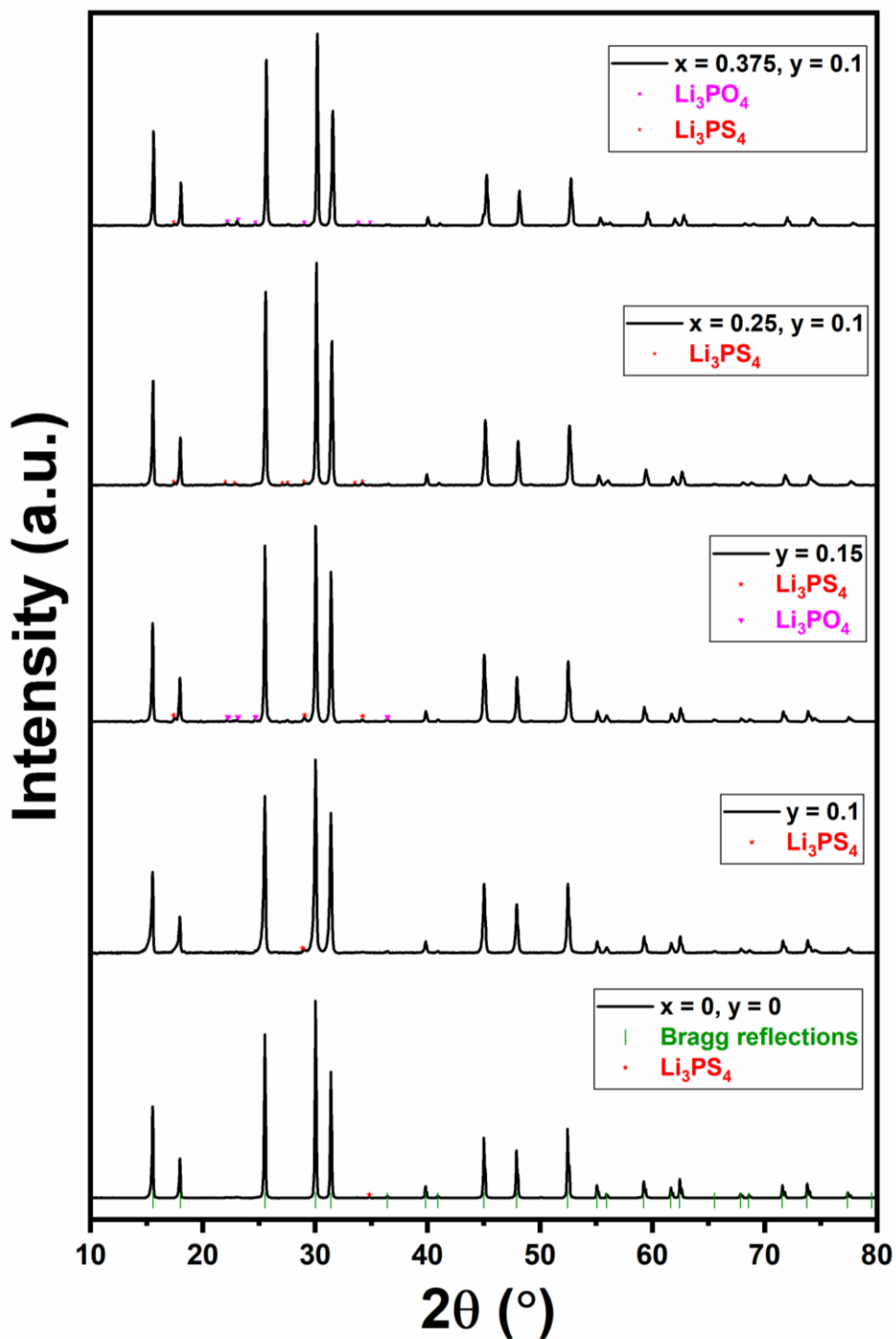


Figure 5.1 XRD (capillary) patterns of ($y = 0, 0.1, 0.15$) and ($x = 0.25, y = 0.1; x = 0.375, y = 0.1$) representing the identified impurities. Vertical tick marks in green represent the calculated positions of the Bragg reflections.

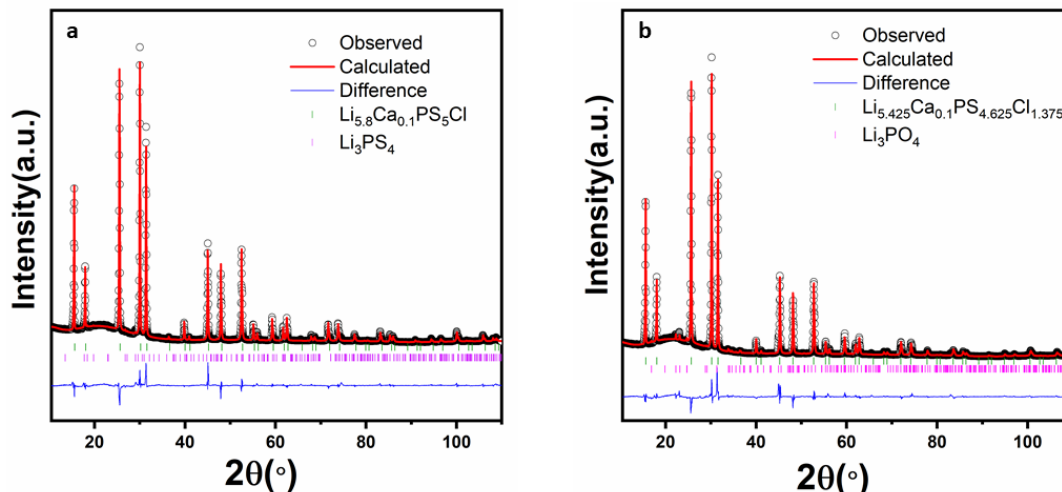


Figure 5.2 Rietveld refinement of XRD patterns of a) $\text{Li}_{5.8}\text{Ca}_{0.1}\text{PS}_5\text{Cl}$, $\text{GOF} = 3.39$, $R_{\text{wp}} = 5.95$ (minority Li_3PS_4 phase: 0.9 wt%) b) $\text{Li}_{5.425}\text{Ca}_{0.1}\text{PS}_{4.625}\text{Cl}_{1.375}$, $\text{GOF} = 5.77$, $R_{\text{wp}} = 7.59$ (minority Li_3PO_4 phase: 2.7 wt%). Experimental data are shown in black, calculated data in red and difference profile in blue. Vertical ticks for Bragg reflections are shown in green and minority impurity phases are illustrated in magenta.

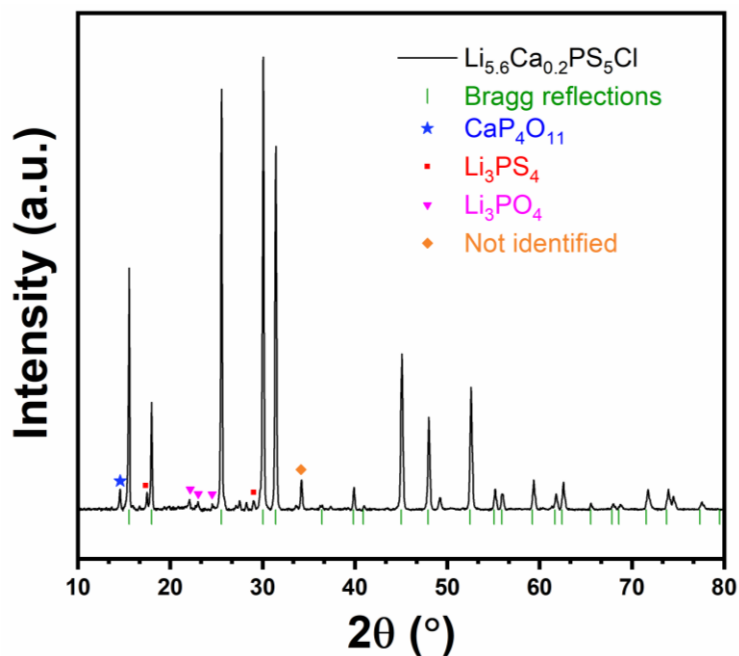


Figure 5.3 XRD pattern of $y = 0.2$ with illustrated impurity.

In order to have a better understanding of the structural influences of Ca^{2+} doping on the argyrodite products, Rietveld refinement against the neutron diffraction pattern was carried out for $y = 0.15$ (**Figure 5.4**) in the cubic space group $F\bar{4}3m$, yielding reasonable occupancy values that were in accord with the targeted stoichiometry. Because of the low fraction of Ca^{2+} in the lattice, the U_{iso} for Ca (0.05 \AA^2) was not refined and was set to be about half that of Li (assuming that a divalent cation will have a smaller atomic displacement parameter on the same site due to its divalent nature and larger size). Performing the refinement without fixing the U_{iso} for Ca^{2+} or with smaller fixed U_{iso} values (e. g. 0.04 \AA^2)^[136], which was reported for Ca^{2+} dopant in other cubic thiophosphates, did not yield meaningful occupancies. We recognise that the accuracy of the refined occupancy of Ca^{2+} could be compromised by our approach; nonetheless, the refined composition ($\text{Li}_{5.71}\text{Ca}_{0.15}\text{PS}_{4.95}\text{Cl}$) is almost identical to the targeted stoichiometry ($\text{Li}_{5.70}\text{Ca}_{0.15}\text{PS}_5\text{Cl}$).

The refinement results for $y = 0.15$ (**Table 5.1**) reveal that both Li^+ and Ca^{2+} ions partially occupy the $48h$ site and neither are present on the $24g$ site. In this Li vacancy-rich material, as in the other Ca-substituted compositions (**Figure 5.6** and **Figure 5.7** discussed below), we do not observe occupation on additional sites in the lattice that were recently revealed by low-temperature neutron diffraction studies of “Li-stuffed” argyrodite $\text{Li}_{6+x}\text{M}_x\text{Sb}_{1-x}\text{S}_5\text{I}$,^[137] and by Zeier’s group for $\text{Li}_6\text{PS}_5\text{X}$ ($\text{X} = \text{Cl}, \text{Br}$).^[138] The site disorder (ratio of $\text{Cl}^-/\text{S}^{2-}$ on the $4c$ site, 62.8%) is almost the same as in the parent phase (61.5%).

Energy dispersive X-ray (EDX) analysis confirmed the homogeneity within the material and showed elemental ratios that were in accord with the theoretical values. Selected examples of the normalized ratios obtained from EDX are given in **Table 5.2**. For $y = 0.1$ and $y = 0.15$, the Ca:P:Cl ratio is 0.10:1.01:1.00 and 0.16:0.99:1.00 respectively

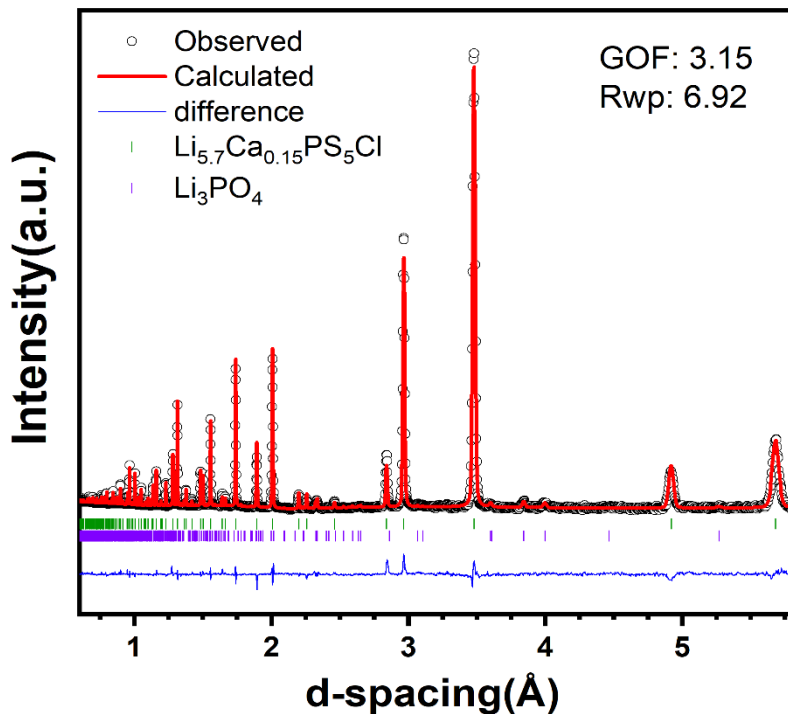


Figure 5.4 Time-of-flight (TOF) neutron powder diffraction pattern of the targeted $\text{Li}_{5.7}\text{Ca}_{0.15}\text{PS}_5\text{Cl}$ after heat-treatment at 550°C for 5 h. Ticks for the minority Li_3PO_4 phase (<1.5 wt%) are in purple.

Table 5.1 Atomic coordinates, occupation factor and isotropic displacement parameters of $\text{Li}_{5.7}\text{Ca}_{0.15}\text{PS}_5\text{Cl}$ obtained from Rietveld refinement of neutron time of flight data (space group $F\bar{4}3m$) $a = 9.8414$ (1) Å, and volume = 953.20 (2) Å³ yielding a refined composition of $\text{Li}_{5.71}\text{Ca}_{0.15}\text{PS}_{4.95}\text{Cl}$.

	Wyckoff Site	x	y	z	SOF	$U_{\text{iso}}(\text{Å}^2)$
Atom						
Li	48h	0.3116	0.0234	0.6885	0.476(14)	0.084(4)
Ca	48h	0.3116	0.0234	0.6885	0.0125(30)	0.05
Cl1	4a	0	0	0	0.420(9)	0.024(1)
Cl2	4c	1/4	1/4	1/4	0.628(11)	0.033(1)
P1	4b	0	0	0.5	1	0.025(1)
S1	4a	0	0	0	0.580(9)	0.024(1)
S2	4c	1/4	1/4	1/4	0.372(11)	0.033(1)
S3	16e	0.1189	-0.1189	0.6189	1	0.040(1)

Table 5.2 EDX analysis of the $\text{Li}_{5.8}\text{Ca}_{0.1}\text{PS}_5\text{Cl}$, $\text{Li}_{5.7}\text{Ca}_{0.15}\text{PS}_5\text{Cl}$ and $\text{Li}_{5.3}\text{Ca}_{0.1}\text{PS}_{4.5}\text{Cl}_{1.5}$. Given the slight amount of hydrolysis that takes place during the material transfer into the SEM chamber, the sulfur content could not be accurately quantified. A minimum of 4 measurements per composition is reported.

$\text{Li}_{5.8}\text{Ca}_{0.1}\text{PS}_5\text{Cl}$	Atomic percent			Weight percent		
Measurement	Ca	P	Cl	Ca	P	Cl
M1	1.79	16.01	17.70	2.20	15.20	19.23
M2	1.83	16.02	18.04	2.25	15.20	19.59
M3	1.67	17.38	15.42	2.06	16.55	16.81
M4	1.89	17.10	16.47	2.33	16.25	17.91
M5	1.60	17.87	15.84	1.97	17.01	17.26
Average	1.76	16.88	16.69	2.16	16.04	18.16
Standard dev.	0.11	0.74	1.15			
Normalized to Cl amount	0.10	1.01	1.00			
$\text{Li}_{5.7}\text{Ca}_{0.15}\text{PS}_5\text{Cl}$	Atomic percent			Weight percent		
Measurement	Ca	P	Cl	Ca	P	Cl
M1	3.14	16.09	18.30	3.84	15.21	19.80
M2	3.12	15.45	18.26	3.82	14.60	19.76
M3	2.15	17.48	15.09	2.64	16.63	16.43
M4	2.49	16.28	14.63	3.07	15.48	15.92
Average	2.73	16.33	16.57	3.34	15.48	17.98
Standard dev.	0.42	0.73	1.70			
Normalized to Cl amount	0.16	0.99	1.00			
$\text{Li}_{5.3}\text{Ca}_{0.1}\text{PS}_{4.5}\text{Cl}_{1.5}$	Atomic percent			Weight percent		
Measurement	Ca	P	Cl	Ca	P	Cl
M1	1.26	15.39	21.55	1.55	14.56	23.35
M2	1.52	15.61	22.27	1.87	14.75	24.10
M3	1.52	14.2	23.72	1.86	13.40	25.61
M4	1.6	15.13	22.62	1.96	14.29	24.45
M5	1.45	15.53	22.27	1.78	14.68	24.10
Average	1.47	15.17	22.49	1.80	14.34	24.32
Standard dev.	0.01	0.26	0.5			
Normalized to P amount	0.10	1.00	1.48			

Compositions varying in both Ca and Cl contents. Targeted compositions $\text{Li}_{6-x-2y}\text{Ca}_y\text{PS}_{5-x}\text{Cl}_{1+x}$ ($x = 0.25, y = 0.1; x = 0.25, y = 0.15; x = 0.375, y = 0.1; x = 0.5, y = 0.1$) were prepared. The XRD patterns of ($x = 0.25, y = 0.1$) and ($x = 0.375, y = 0.1$) are presented in **Figure 5.1**, indicating that the materials are essentially pure single phases. The composition was confirmed by refinements against the XRD data for ($x = 0.375, y = 0.1$; **Figure 5.2b**) and ($x = 0.5, y = 0.1$; **Figure B.1, Table B.1**) and against the NPD data for ($x = 0.25, y = 0.1$; **Figure 5.6**) that all revealed ≤ 2.7 wt % impurities. However, additional Ca substitution to target a nominal composition of $\text{Li}_{5.45}\text{Ca}_{0.15}\text{PS}_{4.75}\text{Cl}_{1.25}$ led to a notable fraction of secondary phases, which had an undesirable impact on the ionic conductivity. Therefore, the Cl-rich argyrodites cannot sustain as high a degree of Ca substitution, likely owing to vacancy limitations on the $48h$ site. The local structure of $x = 0.5, y = 0.10$ was explored with Raman, showing only the PS_4^{3-} moiety characteristic of the crystalline structure with no evidence of P_2S_6 (**Figure 5.5a**). The EDX for this phase yielded a Ca:P:Cl ratio of 0.10:1.00:1.48 (**Table 5.2**).

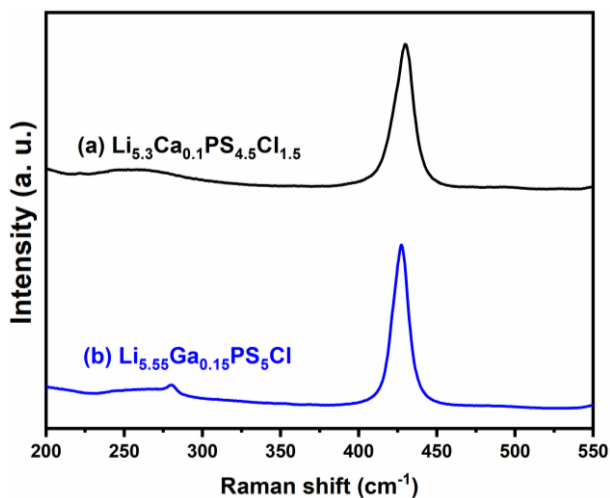


Figure 5.5 Raman spectra for (a) $\text{Li}_{5.3}\text{Ca}_{0.1}\text{PS}_{4.5}\text{Cl}_{1.5}$ and (b) $\text{Li}_{5.55}\text{Ga}_{0.15}\text{PS}_5\text{Cl}$ exhibiting the peaks corresponding to PS_4^{3-} moiety.

Rietveld refinement of $x = 0.25, y = 0.1$ was performed against the neutron data (**Figure 5.6**), where the U_{iso} values for Li and Ca on the $48h$ site were fixed (see **5.1.2** for details). The results of the Rietveld refinement are presented in **Table 5.3** and reveal a composition of $\text{Li}_{5.56}\text{Ca}_{0.10}\text{PS}_{4.73}\text{Cl}_{1.27}$ that is very close to the targeted $\text{Li}_{5.55}\text{Ca}_{0.1}\text{PS}_{4.75}\text{Cl}_{1.25}$. The site disorder increases to 74%, compared to 61% for $\text{Li}_6\text{PS}_5\text{Cl}$.

Rietveld refinement of the “super Cl-rich” $x = 0.55, y = 0.1$ was similarly performed against neutron diffraction data (**Figure 5.7**), where the U_{iso} values for Li and Ca on the $48h$ site were fixed. The results of the Rietveld refinement are presented in **Table 5.4** and show a refined composition of $\text{Li}_{5.36}\text{Ca}_{0.08}\text{PS}_{4.47}\text{Cl}_{1.54}$ that is almost identical to targeted $\text{Li}_{5.35}\text{Ca}_{0.1}\text{PS}_{4.5}\text{Cl}_{1.55}$. While the diffraction pattern of this “super Cl-rich” material appears to be single phase, its ^7Li NMR spectrum reveals the presence of two closely related argyrodite-type phases which will be discussed later in the NMR section.

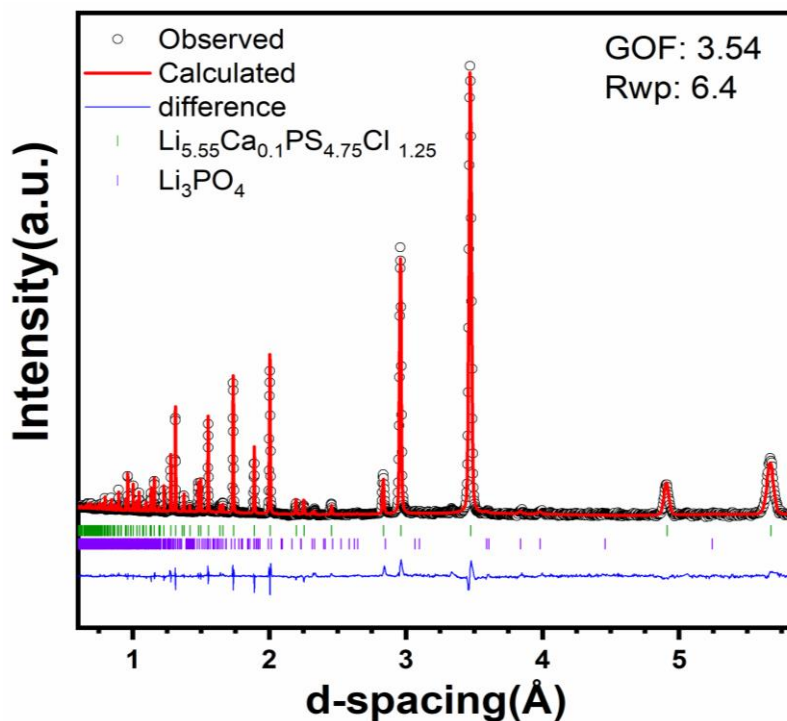


Figure 5.6 TOF neutron powder diffraction pattern of $\text{Li}_{5.55}\text{Ca}_{0.1}\text{PS}_{4.75}\text{Cl}_{1.25}$. Bragg reflections are shown in green; ticks for the minority Li_3PO_4 phase (0.63 wt%) are illustrated in purple.

Table 5.3 Atomic coordinates, occupation factor and isotropic displacement parameters of $\text{Li}_{5.55}\text{Ca}_{0.1}\text{PS}_{4.75}\text{Cl}_{1.25}$ obtained from Rietveld refinement of neutron time of flight data (space group $F\bar{4}3m$) $a = 9.8222(1)$ Å, and volume = $947.59(2)$ Å³. The calculated composition $\text{Li}_{5.56}\text{Ca}_{0.10}\text{PS}_{4.73}\text{Cl}_{1.27}$ is close to the targeted one.

Atom	Wyckoff Site	x	y	z	SOF	$U_{\text{iso}}(\text{Å}^2)$
Li	48h	0.3143(15)	0.0212(9)	0.6858(15)	0.463(3)	0.075
Ca	48h	0.3143(15)	0.0212(9)	0.6858(15)	0.008(3)	0.05
Cl1	4a	0	0	0	0.536(15)	0.028(1)
Cl2	4c	1/4	1/4	1/4	0.738(15)	0.033(1)
P1	4b	0	0	0.5	1	0.030(1)
S1	4a	0	0	0	0.464(15)	0.028(1)
S2	4c	1/4	1/4	1/4	0.262(15)	0.033(1)
S3	16e	0.120	-0.120	0.620	1	0.049(1)

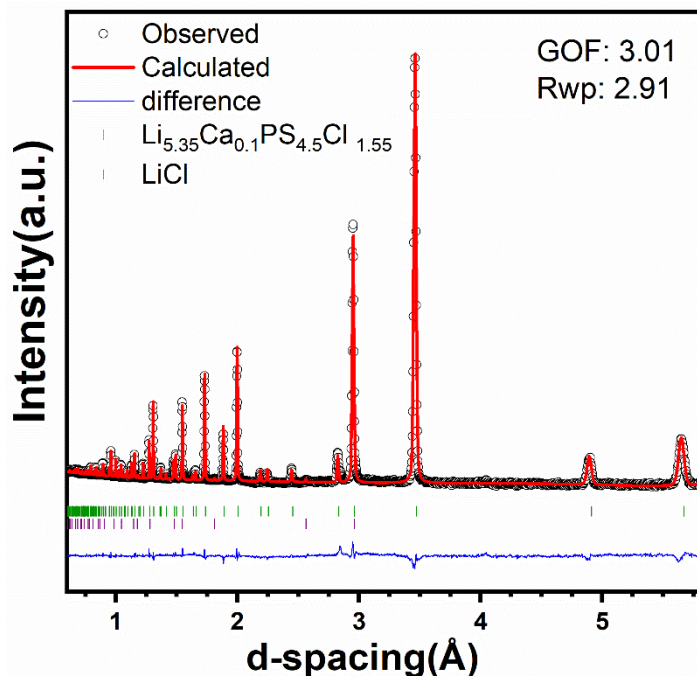


Figure 5.7 TOF neutron powder diffraction pattern of $\text{Li}_{5.35}\text{Ca}_{0.1}\text{PS}_{4.5}\text{Cl}_{1.55}$ after heat-treatment at 550°C for 5 h. Ticks for the minority LiCl phase (0.6 wt%) are in purple.

Table 5.4 Atomic coordinates, occupation factor and isotropic displacement parameters of $\text{Li}_{5.35}\text{Ca}_{0.1}\text{PS}_{4.5}\text{Cl}_{1.55}$ obtained from Rietveld refinement of neutron time of flight data (space group $F\bar{4}3m$) $a = 9.7898(1)$ Å, and volume = $938.24(3)$ Å³. The calculated composition $\text{Li}_{5.36}\text{Ca}_{0.08}\text{PS}_{4.47}\text{Cl}_{1.54}$ is very close to targeted.

Atom	Wyckoff Site	x	y	z	SOF	$U_{\text{iso}}(\text{Å}^2)$
Li	48h	0.3174(8)	0.0227(10)	0.6827(8)	0.447(3)	0.075
Ca	48h	0.3174(8)	0.0227(10)	0.6827(8)	0.007(3)	0.05
Cl1	4a	0	0	1	0.668 (19)	0.020(1)
Cl2	4c	1/4	1/4	3/4	0.867(17)	0.031(1)
P1	4b	0	0	0.5	1	0.030(1)
S1	4a	0	0	1	0.332(19)	0.020(1)
S2	4c	1/4	1/4	3/4	0.133(15)	0.031(1)
S3	16e	0.1200	-0.1200	0.6200	1	0.048(1)

Compositions containing tri and tetra-valent cations. Other aliovalent dopants on the Li site were also explored including but not limited to trivalent Ga^{3+} , Al^{3+} , and tetravalent Zr^{4+} and Si^{4+} . Different factors such as the size of the cation, mobility, charge, cost, and elemental abundance, were considered. Ge substitution on the P site was recently reported, yielding high conductivity, but this presents limitations in terms of both cost and stability.^[92] Owing to the smaller size of Al^{3+} (0.535 Å) and Ga^{3+} (0.620 Å) cations compared to Li^+ (0.76 Å), only small fractions of dopant could be incorporated ($y = 0.1$); selected XRD patterns/refinement (**Figure 5.8** and **Figure 5.9**), along with EDX data (**Table 5.5**) are presented below. Attempts to synthesize phase pure $\text{Li}_{6-3y}\text{M}_y\text{PS}_5\text{Cl}$ ($\text{M}=\text{Al}$ and Ga) at $y > 0.15$ were unsuccessful and led to significant Li_3PS_4 and lithium thiogallate (LiGaS_2) impurities respectively. Si^{4+} or Zr^{4+} doping was not feasible. Given that the Ca-argyrodite prepared materials exhibited the most promising results in terms of purity and conductivity (discussed later in the transport section) at higher doping levels, we focused the ^7Li NMR investigations on this set of materials which utilize earth-abundant elements Ca, P and S.^[139]

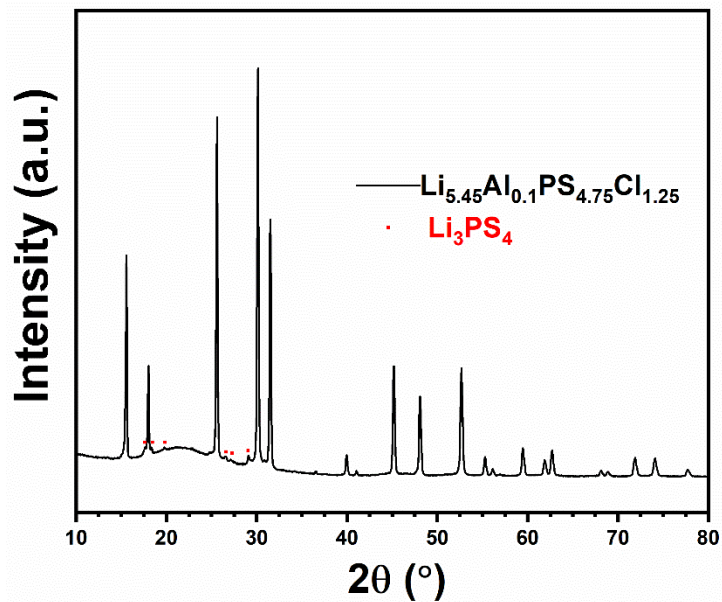


Figure 5.8 XRD pattern of $\text{Li}_{5.45}\text{Al}_{0.1}\text{PS}_{4.75}\text{Cl}_{1.25}$ heat treated at 550°C for 5 h.

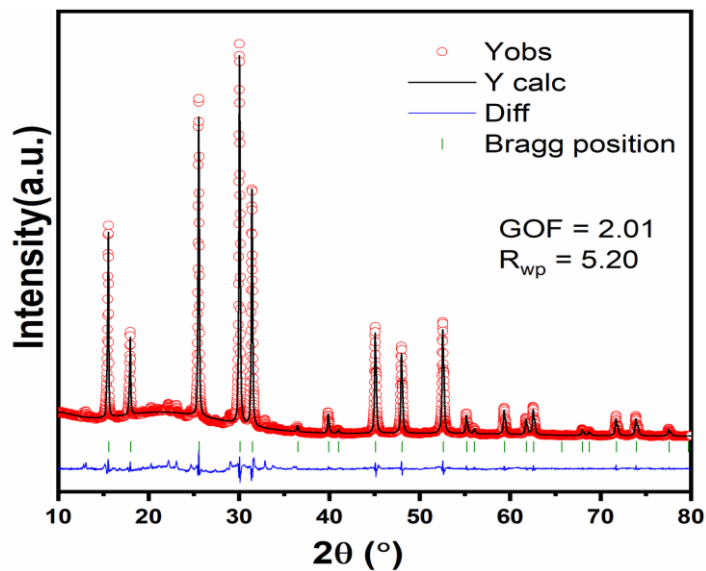


Figure 5.9 XRD pattern of $\text{Li}_{5.7}\text{Ga}_{0.1}\text{PS}_5\text{Cl}$, $a = 9.8374(1) \text{ \AA}$ obtained from whole pattern fitting.

Table 5.5 EDX analysis of the $\text{Li}_{5.7}\text{Ga}_{0.1}\text{PS}_5\text{Cl}$ and $\text{Li}_{5.45}\text{Al}_{0.1}\text{PS}_{4.75}\text{Cl}_{1.25}$. Given the slight amount of hydrolysis that takes place during the material transfer into the SEM chamber, the sulfur content could not be accurately quantified. A minimum of three measurements per composition are reported.

$\text{Li}_{5.8}\text{Ga}_{0.1}\text{PS}_5\text{Cl}$	Atomic percent			Weight percent		
Measurement	Ga	P	Cl	Ga	P	Cl
M1	1.73	15.95	16.34	3.64	14.93	17.50
M2	1.71	17.15	14.26	3.61	16.10	15.31
M3	1.10	17.42	14.66	2.33	16.46	15.85
M4	1.50	15.87	17.05	3.17	14.88	18.30
Average	1.51	16.60	15.58	3.19	15.59	16.74
Standard dev.	0.25	0.69	1.15			
Normalized to Cl amount	0.10	1.06	1.00			
$\text{Li}_{5.45}\text{Al}_{0.1}\text{PS}_{4.75}\text{Cl}_{1.25}$	Atomic percent			Weight percent		
Measurement	Al	P	Cl	Al	P	Cl
M1	1.24	16.57	19.48	1.03	15.81	21.26
M2	1.43	16.48	19.42	1.19	15.72	21.21
M3	1.39	16.50	19.46	1.15	15.74	21.24
Average	1.35	16.52	19.45	1.12	15.76	21.24
Standard dev.	0.08	0.04	0.02			
Normalized	0.09	1.06	1.25			

⁷Li MAS NMR

Besides NPD, the presence of Ca^{2+} in the vicinity of Li^+ was also established by the appearance of a small secondary peak in the ^7Li MAS NMR measurements for several Ca^{2+} -containing compositions (**Figure 5.10**), along with the expected main resonance. Deconvolution of the lineshapes for $y = 0.1$, $y = 0.15$, and $(x = 0.25, y = 0.1)$, for which the secondary peak was not obscured by the larger, halide-enrichment-induced chemical shift trend,^[109] yielded peak areas with ratios corresponding to the $\text{Li}^+/\text{Ca}^{2+}$ stoichiometric ratio in each case. For several nominally targeted $(x = 0.5, y = 0.1)$ compositions, we observed more than one main peak in the ^7Li MAS NMR (**Figure 5.10**). Although there was no indication of more than one significant phase in the XRD or NPD pattern, these materials exhibited higher diffusivity. This prompted us to increase the Cl-content further and target the composition $\text{Li}_{5.35}\text{Ca}_{0.1}\text{PS}_{4.5}\text{Cl}_{1.55}$. This “super Cl-rich” material appears single phase by neutron diffraction (**Figure 5.7**) but its biphasic nature is evidenced by its ^7Li MAS NMR spectrum (**Figure 5.10**, upper trace in dark green), which exhibits two very well-resolved peaks. The peak at 0.98 ppm is consistent with the phase where $x \simeq 0.5$, whereas the new narrow peak at 0.83 ppm that is shifted to a much lower frequency environment is indicative of a more chlorine-rich argyrodite. This peak does not correspond to LiCl , which appears at -1.2 ppm as a solid,^[109] and was only observed in trace amounts in the full spectra of **Figure 5.10**. Semi-quantitative analysis based on the 1:2 area of the two peaks in the spectrum (derived from curve deconvolution), and the overall targeted stoichiometry suggests a composition of $x \sim 0.63$ for the new argyrodite at 0.83 ppm. The jump to much lower frequency (*vis a vis* the $x = 0.50$ composition) indicates the lithium ions in this argyrodite (which may form nano-domains not resolvable in the NPD pattern) exhibit a unique electronic environment that is more highly surrounded by chloride anions.

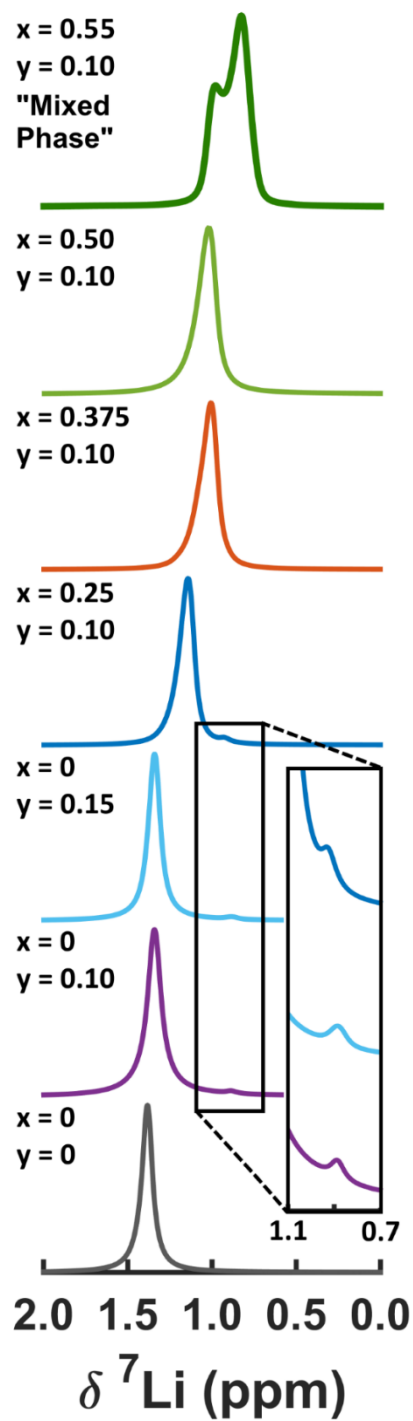


Figure 5.10 Stack plot of ^7Li MAS spectra for the y-series and dual-doped series, demonstrating the strong chlorine-enrichment shift trend, and no major change in chemical shift associated with Ca^{2+} -doping. The inset reveals the secondary peak associated with a Ca^{2+} dopant.

Physical and electrochemical properties

The relative density of all the cold-pressed pellets was $91 \pm 0.8 \text{ g. cm}^{-3}$ (**Table 5.6**). This value was calculated using the sample geometry and mass compared to the theoretical density of the argyrodite. The morphology of the microcrystalline material obtained by scanning electron microscopy (**Figure 5.11**) reveals that there is a distribution in the size of the particles (predominantly 0.5 to 5 μm). Comparative SEM studies showed that the Ca substitution does not influence the dominant grain size range (**Figure 5.11b**).

Table 5.6 The relative density of the cold-pressed pellets. This value was calculated using the sample geometry and mass compared to the theoretical density of the argyrodite.

Composition	$\text{Li}_{5.7}\text{Ca}_{0.15}\text{PS}_5\text{Cl}$	$\text{Li}_{5.55}\text{Ca}_{0.1}\text{PS}_{4.75}\text{Cl}_{1.25}$	$\text{Li}_{5.3}\text{Ca}_{0.1}\text{PS}_{4.5}\text{Cl}_{1.5}$
Relative density	89.9	91.7	91.5

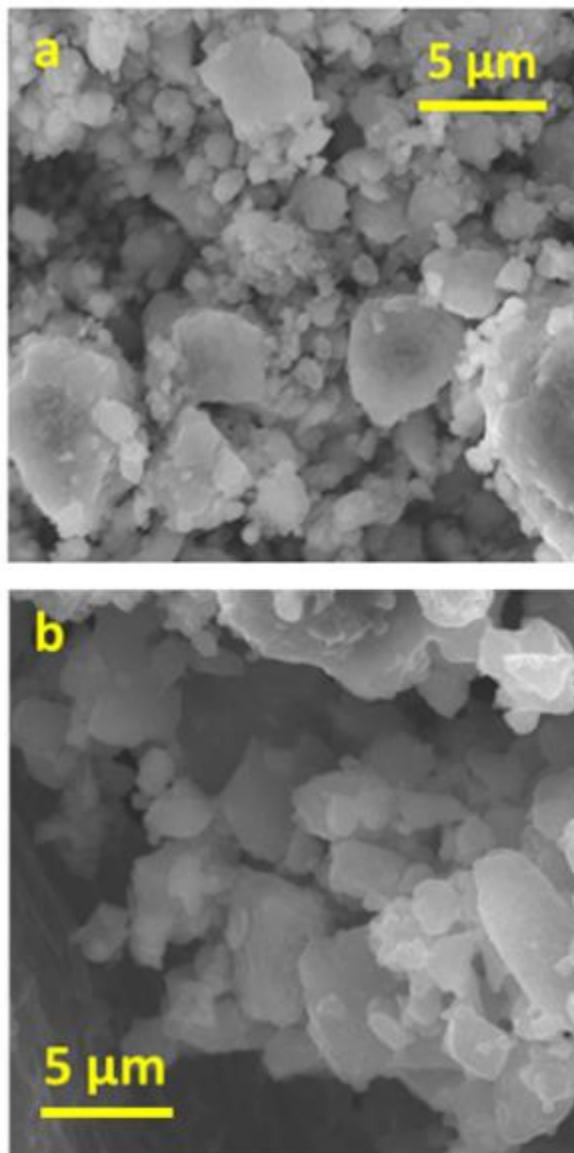


Figure 5.11 SEM images of a) $y = 0.1$ $x = 0$, (550°C, 5 h) and b) of $y = 0.15$ $x = 0$, (550°C, 5 h).

The electrochemical window is significant to assess the stability of the prepared electrolyte against lithium metal. The presence of metals such as Si and Ge that are easily reduced would have a detrimental impact on the voltage window that the solid electrolyte can offer. For example, Jung *et al.* carried out cyclic voltammetry to evidence that despite the higher conductivity (> 6 times) of LGPS compared to Li_3PS_4 , the former exhibits poor stability in the low voltage range below ~ 1

V (vs. Li/Li⁺).^[140] We recorded the cyclic voltammograms of SS/y = 0.1 (x = 0)/Li cell in a voltage window of 5.0 to -0.1 V at a scan rate of 1 mV s⁻¹ at 300 K (illustrated in **Figure 5.12a**) which is in accord with the recently reported voltage window for y = 0.^[67] The prepared samples also exhibited a low electronic conductivity on the order of 10⁻⁹ S.cm⁻¹. The prepared materials exhibited a low electronic conductivity: the DC polarisation curve of a representative sample (y =

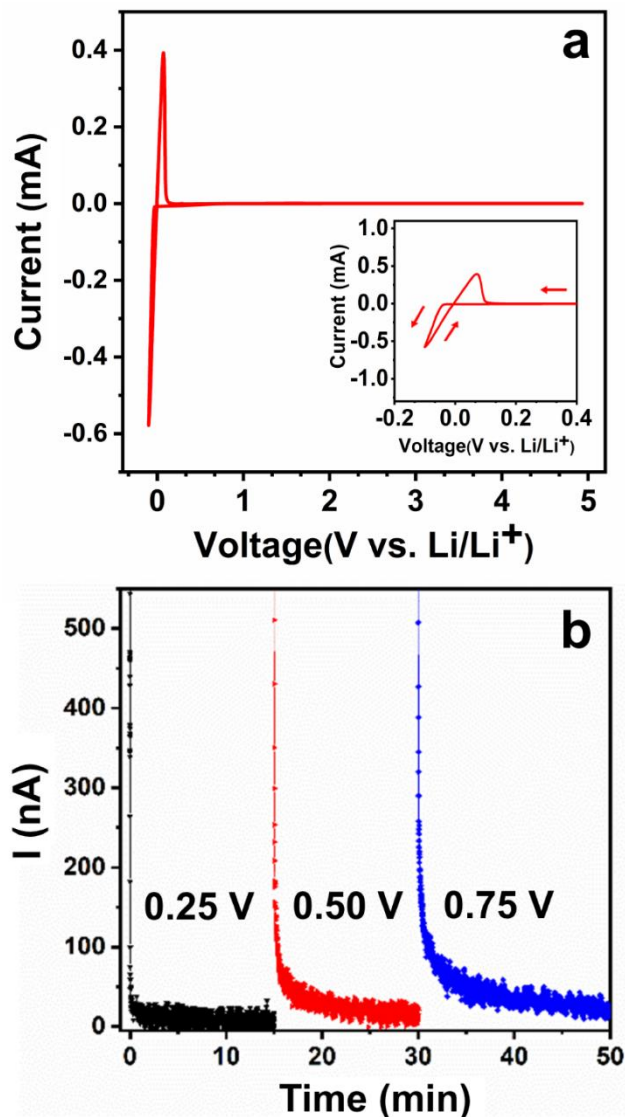


Figure 5.12 a) Cyclic voltammogram curve of the stainless steel/y = 0.1 (x = 0)/Li cell with scan rate of 1 mV S⁻¹ in the voltage window of 5.0 to -0.1 V, inset shows the magnified view in the voltage range of 0.4 to -0.1 V. b) DC polarisation curve for y = 0.15 (x = 0) at 0.25 V (black), 0.5 V (red), 0.75 V (blue) (cold-pressed at two tons and 300 K).

0.15, $\sigma_e = 5 \times 10^{-9} \text{ S.cm}^{-1}$) is demonstrated in **Figure 5.12**. Thus, the combination of good stability and low electronic conductivity makes the substituted argyrodite materials favorable as a solid electrolyte.

Transport Properties of the Ca-doped compositions

Temperature-dependent EIS and PFG-NMR measurements were carried out to assess changes to the ion transport as a result of Ca^{2+} substitution in selected standard and Cl-rich compositions. The corresponding impedance responses with the respective fits are shown in **Figure 5.13**, and Arrhenius plots of all materials obtained from EIS are shown in **Figure 5.14** and **Figure 5.15**. Since the CPE/resistor component is shifted to frequencies at room temperature that are too high to measure with the impedance analyzer, only the Warburg tail of the blocking electrodes was used for the fit. EIS measurement for $y = 0.15$ was performed at 195 K by immersing the sealed EIS cell in a cooling bath. The impedance data at low temperature were fit with an equivalent circuit consisting of one parallel constant phase element (CPE)/resistor in series with a CPE, representing the blocking electrodes. Bulk and grain boundary contributions could not be deconvoluted but the α value is 0.9 denoting the ideality of the CPE (**Figure 5.16** and **Table 5.7**). The ionic conductivities at room temperature and the activation energies (E_a) for compositions varying in both Ca and Cl content are displayed in **Table 5.8**. The marriage of anion disorder and the presence of unoccupied neighboring sites for the mobile ion hops lead to good conductivity.

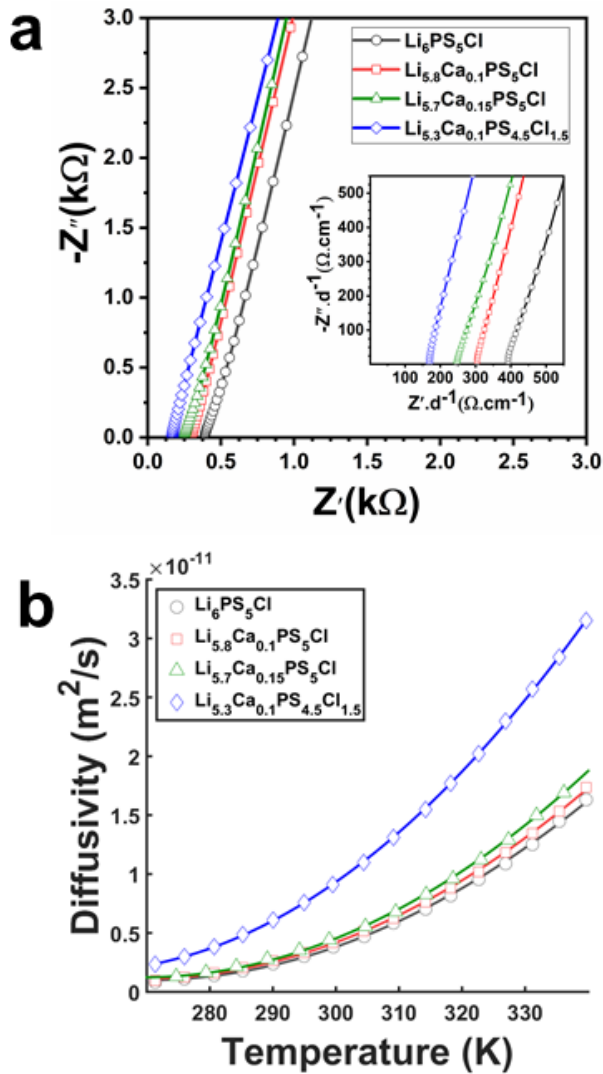


Figure 5.13 a) Nyquist impedance plots of $y = 0, 0.1, 0.15$, ($x = 0$) and $y = 0.1, x = 0.5$ at 298 K. Figure inset illustrates the enlarged view at high frequencies. For the sake of easy comparison, the impedance was normalized to the corresponding pellet thickness d (cm); b) Diffusivity plots for $y = 0, 0.1, 0.15$ ($x = 0$), $y = 0.1, x = 0.5$ from PFG NMR data.

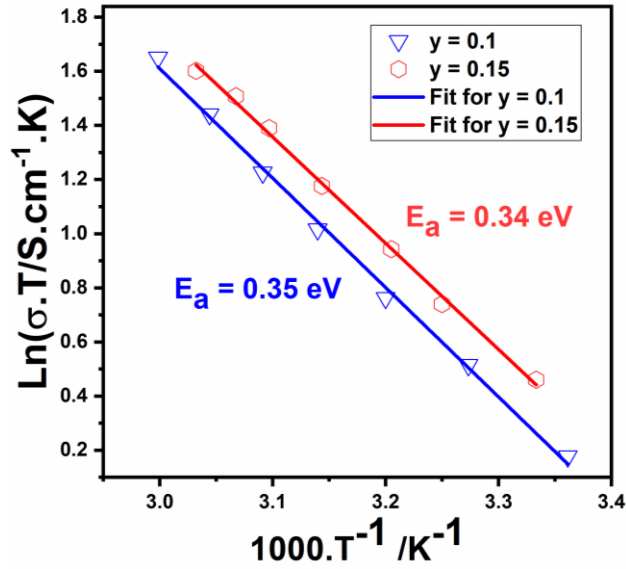


Figure 5.14 Temperature dependence of the ionic conductivity for $y = 0.1$ and $y = 0.15$.

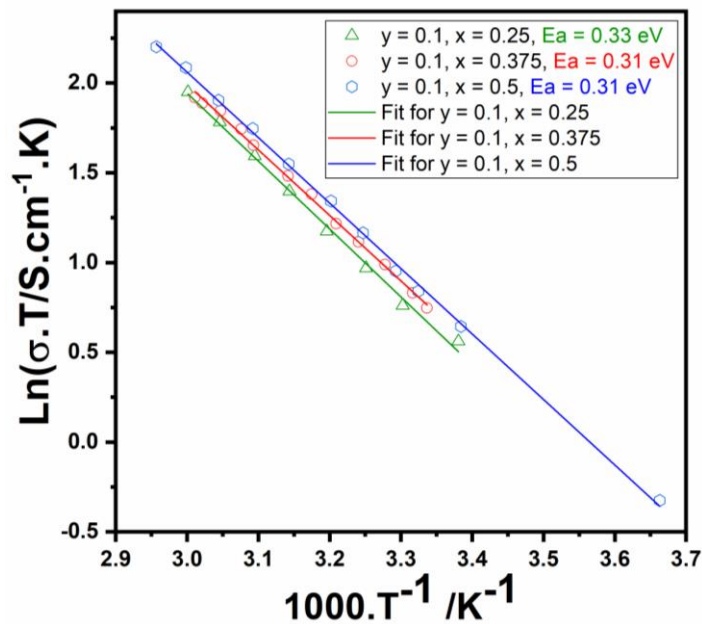


Figure 5.15 Temperature dependence of the ionic conductivity for $x = 0.25, 0.375, 0.5$ ($y = 0.1$).

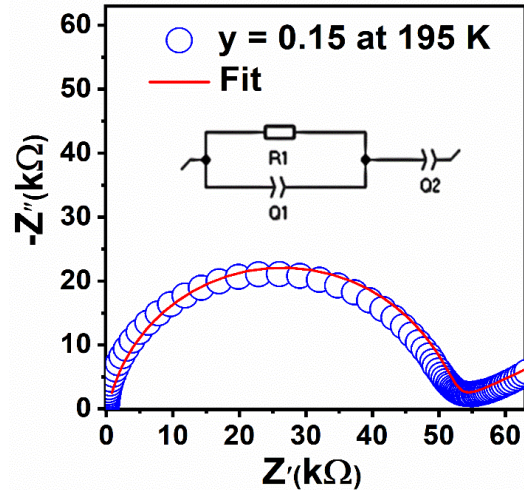


Figure 5.16 Nyquist plot of $y = 0.15$ at 195 K. The apex frequency is 1.11×10^4 Hz, which corresponds to a capacitance of 1.78×10^{-9} F; the α -value is almost 0.9, indicating the ideality of the CPE.

Table 5.7 Fitted EIS parameters for $y = 0.15$ at 195 K

($r_{\text{electrode}} = 5$ mm, $d_{\text{electrode}} = 1.28$ mm).

Equivalent circuit=	R1/Q1+Q2
R1	50724 ohm
Q1	$1.108e-9 \text{ F}\cdot\text{s}^{(a-1)}$
a1	0.8987
Q2	$38.14e-6 \text{ F}\cdot\text{s}^{(a-1)}$
a2	0.2965

Table 5.8 Conductivity (σ at 25 °C, for cold-pressed pellets at 2 ton) and activation energy (E_a) values obtained from EIS and PFG Arrhenius plots for the prepared Ca-argyrodites. See **Table 5.9** for analysis details.

Compositions	σ_{tot} [mS.cm ⁻¹]	E_a (EIS) [eV] \pm 0.01	E_a (PFG) [eV]
Li ₆ PS ₅ Cl (pristine)	3.1	0.34	0.35 (1)
Li _{5.9} Ca _{0.05} PS ₅ Cl	3.5	-	-
Li _{5.8} Ca _{0.1} PS ₅ Cl	4.3	0.35	0.337 (4)
Li _{5.7} Ca _{0.15} PS ₅ Cl	5.2	0.34	0.334 (3)
Li _{5.6} Ca _{0.2} PS ₅ Cl	3.4	-	-
Varying in both Ca and Cl			
Li _{5.55} Ca _{0.1} PS _{4.75} Cl _{1.25}	6.8	0.33	0.317 (6)
Li _{5.45} Ca _{0.15} PS _{4.75} Cl _{1.25}	6.1	-	-
Li _{5.425} Ca _{0.1} PS _{4.625} Cl _{1.375}	7.2	0.31	0.307 (7)
Li _{5.3} Ca _{0.1} PS _{4.5} Cl _{1.5}	7.7	0.31	0.302 (5)
Li_{5.35}Ca_{0.1}PS_{4.5}Cl_{1.55} -Pellet	10.2	0.30	0.287 (4)
Li _{5.35} Ca _{0.1} PS _{4.5} Cl _{1.55} - Powder	-	-	0.301 (4)

The site disorder arises because Cl⁻ ions share two sites (4*a* and 4*c*) with S²⁻ which alters the energy landscape for Li ion diffusion.^[76] For Li_{6-2y}Ca_yPS₅Cl, the stepwise introduction of Ca in the Li site is accompanied by a gradual increase in vacancy concentration which is the main contributor to the enhancement in the conductivity, given that the disorder is not significantly changed *vis a vis* Li₆PS₅Cl. The effect of Ca²⁺ incorporation on the intracage or doublet jumps should be negligible at this small level of doping (one Ca per ~ 10 and ~ 6 cages for $y = 0.1$, $y = 0.15$ respectively). It is the long-range transport between the cages (intercage) which dictates the macroscopic conductivity in Li-argyrodites, as demonstrated by ab initio molecular dynamics simulations.

Table 5.9 Room temperature resistance values for $\text{Li}_{6-x-2y}\text{Ca}_y\text{PS}_{5-x}\text{Cl}_{1+x}$ (cold-pressed pellets at 2 ton, 10 mm diameter) obtained from the fit of the real-axis impedance intercept in the Nyquist plot. R, d and σ denote resistance, thickness and total conductivity respectively. Samples **A**, **E**, **G** and **K** are depicted in **Figure 5.13a**.

$\text{Li}_{6-x-2y}\text{Ca}_y\text{PS}_{5-x}\text{Cl}_{1+x}$	Sample	d (mm)	R(Ω)	σ ($\text{mS}\cdot\text{cm}^{-1}$)	σ_{average} ($\text{mS}\cdot\text{cm}^{-1}$)
Li₆PS₅Cl (pristine)	A	0.649	25.1	3.30	3.12
	B	0.625	27.2	2.93	
Li_{5.9}Ca_{0.05}PS₅Cl	C	0.704	25.7	3.50	3.50
	D	0.606	22.3	3.50	
Li_{5.8}Ca_{0.1}PS₅Cl	E	0.804	24.1	4.25	4.26
	F	0.768	22.9	4.27	
Li_{5.7}Ca_{0.15}PS₅Cl	G	0.983	24.1	5.20	5.18
	H	1.032	25.5	5.16	
Li_{5.6}Ca_{0.2}PS₅Cl	I	0.664	24.8	3.41	3.40
	J	0.732	27.6	3.38	
Li_{5.55}Ca_{0.1}PS_{4.75}Cl_{1.25}	K	0.736	13.7	6.84	6.76
	L	0.722	13.8	6.67	
Li_{5.45}Ca_{0.15}PS_{4.75}Cl_{1.25}	M	1.070	22.2	6.14	6.06
	N	0.695	14.8	5.98	
Li_{5.425}Ca_{0.1}PS_{4.625}Cl_{1.375}	O	0.880	15.3	7.33	7.24
	P	0.926	16.5	7.15	
Li_{5.3}Ca_{0.1}PS_{4.5}Cl_{1.5}	Q	0.729	12.1	7.68	7.74
	R	1.096	17.9	7.80	
Li_{5.35}Ca_{0.1}PS_{4.5}Cl_{1.55}	S	0.966	12.1	10.2	

These studies showed that the intercage jump rate has the lowest jump frequency of all and will hence limit macroscopic diffusion. For example, in the case of $\text{Li}_6\text{PS}_5\text{Cl}$, the jump rates are 0.73, 17.78, and $21.58 (\times 10^{10} \text{ s}^{-1})$ for intercage, intracage and doublet jumps, respectively.^[76] The fact that the Ca^{2+} does not disrupt transport is further supported by the activation energies of the solely Ca^{2+} -substituted phases (**Table 5.8**), which are effectively the same as $\text{Li}_6\text{PS}_5\text{Cl}$. Regarding the argyrodites with trivalent dopants, selected conductivity and extracted impedance analyses values are demonstrated in **Table 5.10**, among which, $\text{Li}_{5.45}\text{Al}_{0.1}\text{PS}_{4.75}\text{Cl}_{1.25}$ exhibited the highest ionic conductivity of the compositions ($5.7 \text{ mS}\cdot\text{cm}^{-1}$), which is lower than its Ca^{2+} counterpart, $\text{Li}_{5.55}\text{Ca}_{0.1}\text{PS}_{4.75}\text{Cl}_{1.25}$ ($\sigma = 6.8 \text{ mS}\cdot\text{cm}^{-1}$).

Table 5.10 Room temperature resistance values for $\text{Li}_{6-x-3y}\text{M}_y\text{PS}_{5-x}\text{Cl}_{1+x}$ (cold-pressed pellets at 2 ton, 10 mm diameter) obtained from the fit of the real-axis impedance intercept in the Nyquist plot. R, d and σ denote resistance, thickness, and total conductivity respectively.

$\text{Li}_{6-x-3y}\text{M}_y\text{PS}_{5-x}\text{Cl}_{1+x}$	σ ($\text{mS}\cdot\text{cm}^{-1}$)	d (mm)	R(Ω)	Lattice parameter(\AA)
$\text{Li}_{5.7}\text{Al}_{0.1}\text{PS}_5\text{Cl}$	3.70	0.615	21.2	-
$\text{Li}_{5.4}\text{Al}_{0.2}\text{PS}_5\text{Cl}$	3.60	0.635	22.5	-
$\text{Li}_{5.45}\text{Al}_{0.1}\text{PS}_{4.75}\text{Cl}_{1.15}$	4.76	0.631	16.9	-
$\text{Li}_{5.45}\text{Al}_{0.1}\text{PS}_{4.75}\text{Cl}_{1.25}$	5.69	0.500	11.2	9.8249(2)
$\text{Li}_{5.45}\text{Al}_{0.1}\text{PS}_{4.75}\text{Cl}_{1.35}$	5.29	0.942	22.7	-
$\text{Li}_{5.15}\text{Al}_{0.2}\text{PS}_{4.75}\text{Cl}_{1.25}$	3.58	0.629	22.4	-
$\text{Li}_{5.85}\text{Ga}_{0.05}\text{PS}_5\text{Cl}$	3.74	0.720	24.5	-
$\text{Li}_{5.7}\text{Ga}_{0.1}\text{PS}_5\text{Cl}$	3.89	0.590	19.3	9.8374(1)
$\text{Li}_{5.55}\text{Ga}_{0.15}\text{PS}_5\text{Cl}$	4.44	1.09	31.3	-
$\text{Li}_{5.4}\text{Ga}_{0.2}\text{PS}_5\text{Cl}$	4.05	0.623	19.6	-
$\text{Li}_{5.45}\text{Ga}_{0.1}\text{PS}_{4.75}\text{Cl}_{1.25}$	4.81	0.634	16.8	-

Doping with an aliovalent cation introduces Li vacancies and these generated vacancies increase the Li ion mobility and diffusivity as demonstrated in **Figure 5.13b**, owing to a lower E_a for defect formation. Room temperature Li^+ diffusivities exhibited by the $y = 0.1$ and $y = 0.15$ phases are $4.15 \times 10^{-12} \text{ m}^2/\text{s}$ and $4.44 \times 10^{-12} \text{ m}^2/\text{s}$ respectively, compared with $3.85 \times 10^{-12} \text{ m}^2/\text{s}$ for $y = 0$ (parent phase), which reflects a respective 8% and 15% increase. The dual substituted argyrodite $x = 0.5, y = 0.1$ exhibited a high diffusivity of $9.10 \times 10^{-12} \text{ m}^2/\text{s}$, which is about 2.5 times that of the parent phase, but lower than that of the solely Cl-enriched phase ($\text{Li}_{5.5}\text{PS}_{4.5}\text{Cl}_{1.5}$).^[109] In contrast, the diffusivity of the super Cl-rich $\text{Li}_{5.35}\text{Ca}_{0.1}\text{PS}_{4.5}\text{Cl}_{1.55}$ composition is 33% higher than $x = 0.5, y = 0.1$ with an outstanding value of $1.21 \times 10^{-11} \text{ m}^2/\text{s}$. In $\text{Li}_{6-x-2y}\text{Ca}_y\text{PS}_{5-x}\text{Cl}_{1+x}$, simultaneous substitution of cation and anion yields additional vacancies that contract the lattice to result in a progressive decrease in the interage hop distance with x , along with an increase in the site disorder (**Figure 5.17**, see NPD tables above and **Table B.1**). These factors, conjointly with the weakened electrostatic interactions between the mobile Li-ions and surrounding framework anions (induced by substitution of divalent S^{2-} for monovalent Cl), are the key contributors to the high ionic conductivities for the dual doped compositions, similar to what was found for the purely Cl-enriched argyrodites.^[109] Ionic conductivities for the soft argyrodites can be further improved by hot pressing the powder or sintering and modifying the grain boundaries.

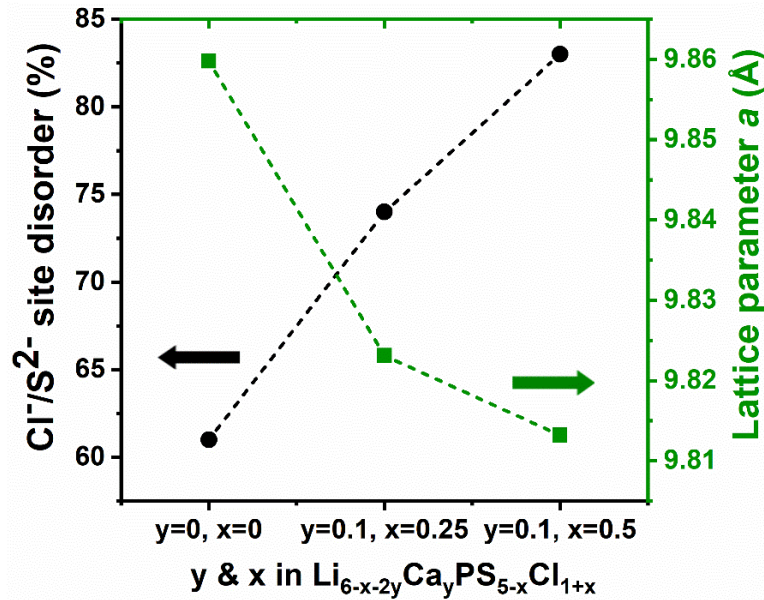


Figure 5.17 Site disorder and lattice parameter vs x for $\text{Li}_{6-x-2y}\text{Ca}_y\text{PS}_{5-x}\text{Cl}_{1+x}$.

Activation energy is a factor that governs ionic conduction. For the Ca-argyrodites, temperature-dependent conductivity measurements follow Arrhenius behavior with the lowest activation energy exhibited by the super Cl-rich material $x = 0.55, y = 0.1$ (0.30 eV). The modified Arrhenius equation was applied to include a temperature dependent pre-exponential: $\sigma T = \sigma_0 \exp(-E_a/k_b T)$, where σ is the temperature dependent ionic conductivity, σ_0 is the prefactor, E_a is the activation energy for ion migration, and k_b and T represent their common meanings. E_a values were also obtained from ^7Li PFG-NMR and are in good accord with the values obtained from impedance spectroscopy, as compared in **Table 5.8**. For each dual-modified composition, the chemical shift observed in NMR was almost identical to that of the equivalent x -only series previously studied.^[109] Combined with the relatively small ^7Li chemical shift of the y -series relative to the parent phase $\text{Li}_6\text{PS}_5\text{Cl}$ (see **Figure 5.10**), this suggests that the Ca^{2+} dopants are not

significantly modifying the electronic environment of Li^+ within the cages where the Ca^{2+} reside; their primary contribution to improving the transport is via the excess vacancies that they introduce to the Li^+ cage network, as illustrated in **Figure 5.13b** and by comparison of the γ -series activation energies with those of the dual-doped series in **Table 5.8**.

5.1.4 Summary and Conclusion

In summary, a novel array of compounds in the Li-argyrodite family was introduced with the advantage of a rapid preparation technique and monitored their behaviour as solid electrolytes by substituting an aliovalent cation for Li^+ and increasing the Cl^- content. This firmly proves the efficacy of aliovalent cation doping in this class of superionic argyrodites as a means of increasing the vacancy population and thereby boosting their conductivity. Furthermore, the underlying principles governing the fast ion conduction and diffusion in this class of materials were established. ASSBs employing thiophosphates often operate with cold-pressed pellets, hence it is important that a solid electrolyte exhibits high conductivity in the absence of sintering. The novel super Cl-rich composition $\text{Li}_{5.35}\text{Ca}_{0.1}\text{PS}_{4.5}\text{Cl}_{1.55}$ possesses a high room temperature ionic conductivity of 10.2 mS cm^{-1} in the cold-pressed state with a low activation energy of $0.30 \pm 0.01 \text{ eV}$ and a very high diffusivity of $1.21 \times 10^{-11} \text{ m}^2/\text{s}$.

5.2 Sodium Argyrodites

5.2.1 Introduction

Sodium's lower cost and natural abundance have motivated researchers to pursue the sodium analogues of lithium-based solid ionic conductors which exhibit attractive ionic conductivity for application in practical sodium solid-state batteries. One such example is the sodium analog of the $\text{Li}_7\text{P}_3\text{S}_{11}$ phase which is predicted to have an ionic conductivity of $10 \text{ mS}\cdot\text{cm}^{-1}$ at room temperature.^[141] Nevertheless, its synthesis has not been successful^[142] to date which is in accord with the computational studies suggesting that the thermodynamic stability may be a challenge for the isostructural Na compound.^[141] Li-argyrodites exhibit a suitable ionic conductivity for practical applications and researchers have put much effort into making the sodium version. Argyrodites with monovalent cations other than Na such as copper and silver argyrodites are quite well known. Recently, Studenyak *et al.* claimed to have made K_7PS_6 and $\text{K}_6\text{PS}_5\text{X}$ (X: Cl, Br)^[143] and they concluded that these materials do not form a cubic argyrodite structure relying on Raman spectra. However, they do not present any diffraction data.

The activation energy for Na^+ ion diffusion is lower than Li^+ ion in argyrodites structure albeit Na-argyrodites are less stable compared to Li-argyrodites. While Adams *et al.* demonstrated that Na_7PS_6 may be a practically accessible Na-argyrodite phase based on computational techniques,^[144] experimental endeavors fail to prove that claim. Xie *et al.* reported on their assiduous efforts to make argyrodite $\text{Na}_{12-n}\text{M}^{n+}\text{S}_6$ (P, Ge, Sn) and stated that they were not successful.^[145]

It was demonstrated that Cl-doping is the most favorable halide (among Cl, Br and I) for doping the anion (S^{2-}) site in Na_3PS_4 phase owing to the lowest formation energy.^[102] The above

inspired this part of my thesis to investigate whether Cl substitution in Na₇PS₆ positively impacts synthesizability.

5.2.2 Material Synthesis and Characterization

Sodium sulfide (Na₂S, Sigma-Aldrich, 99%), phosphorus pentasulfide (P₂S₅, Sigma-Aldrich, 99%), and sodium chloride (NaCl, Sigma-Aldrich, 99%) and lithium chloride (LiCl, Sigma-Aldrich, 99%) powders were used as starting precursors. The stoichiometric amounts of starting precursors (total weight about one gram) were mixed in a mortar for ten minutes in an argon-filled glovebox (H₂O, O₂ <1.5 ppm). For the programs that included milling, the ground mixture was then ball milled with 133 balls in a sealed zirconia jar using a high energy planetary ball mill (Fritsch PULVERISETTE 7 Premium). The milling speed and duration were 400 rpm and 7.5 h respectively. All the materials (other than sample 8) were pelletized in a die inside glovebox before loading to a quartz tube which was vacuum sealed prior to heat treatment.

5.2.3 Results and Discussion

Na₆PS₅Cl, Na_{5.5}PS_{4.5}Cl_{1.5} and Na₅PS₄Cl₂ mixture were prepared, and several heat treatment procedures were attempted. **Table 5.11** summarizes some of these synthesis efforts with different heat treatment programs. The varying parameters are: type of mixing (hand grind or milling), holding temperature, holding time and ramp/cool time.

The reactions for Na_{7-x}PS_{6-x}Cl_x (x = 1, 1.5, 2) are as follows:

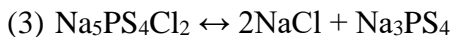


Table 5.11 Various preparation methods for targeted sodium argyrodites.

Sample	Composition	Ballmill speed and length	Ramp	Heat treatment temperature and holding time	Cool
1	Na ₆ PS ₅ Cl	400 rpm, 7.5 h	10 h	550°C, 24 h	60 h
2	Na ₆ PS ₅ Cl	400 rpm, 7.5 h	8.75 h	550°C, 48 h	8.75 h
3	Na ₆ PS ₅ Cl	400 rpm, 7.5 h	30 h	750°C, 168 h	90 h
4	Na ₆ PS ₅ Cl	400 rpm, 7.5 h	25 h	750°C, 336 h	30 h
5	Na ₆ PS ₅ Cl	400 rpm, 7.5 h	21.5 h	800°C, 50 h	25 h
6	Na _{5.5} PS _{4.5} Cl _{1.5}	Hand-grind	11.75 h	730°C, 7.5 h	11.75 h
7	Na _{5.5} PS _{4.5} Cl _{1.5}	Hand-grind	13 h	780°C, 7 h	8.5 h
8	Na ₅ PS ₄ Cl ₂	Hand-grind	36 h	550°C, 24 h	99 h
9	Na ₅ PS ₄ Cl ₂	Hand-grind	17.5 h	550°C, 168 h	87.5 h

XRD patterns for selected samples (1, 2 and 5) are shown in **Figure 5.18**. Most of the peaks observed in XRD correspond to Na₃PS₄, NaCl and Na₂S. XRD patterns for sample 6 and sample 7 are shown in **Figure 5.19**. Peaks for the Na₃PS₄, NaCl and Na₂S phases are identified. The presence of these three phases in the final products is in accord with the above-mentioned reaction (2). Moreover, XRD patterns for sample 8 and sample 9 (**Figure 5.20**) show the formation of the stable Na₃PS₄ phase and presence of NaCl, in accord with the above-mentioned reaction (3). Therefore, our experimental efforts indicate that the competing phases dominate the final products and additional halogen substitution will not stabilize the fully substituted sodium argyrodites.

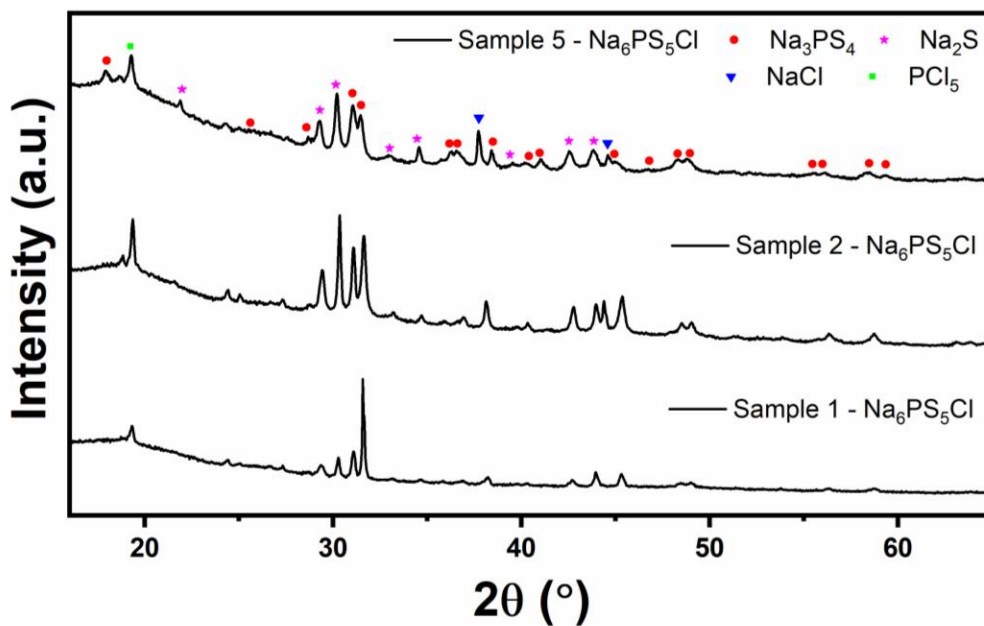


Figure 5.18 XRD patterns (flat stage) for sample six and sample seven from **Table 5.11**. Solid black line shows observed pattern for targeted $\text{Na}_6\text{PS}_5\text{Cl}$. Na_3PS_4 , NaCl and Na_2S peaks are identified with red circles, blue triangles, and magenta stars, respectively.

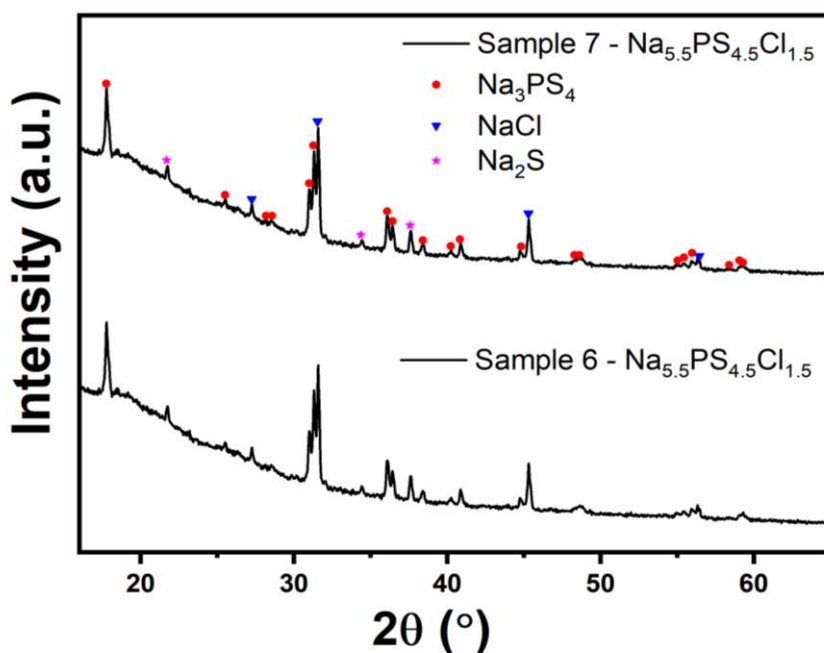


Figure 5.19 XRD patterns (flat stage) for sample six and sample seven from **Table 5.11**. Solid black line denotes observed pattern for targeted $\text{Na}_{5.5}\text{PS}_{4.5}\text{Cl}_{1.5}$. Na_3PS_4 , NaCl and Na_2S peaks are identified with red circles, blue triangles, and magenta stars, respectively.

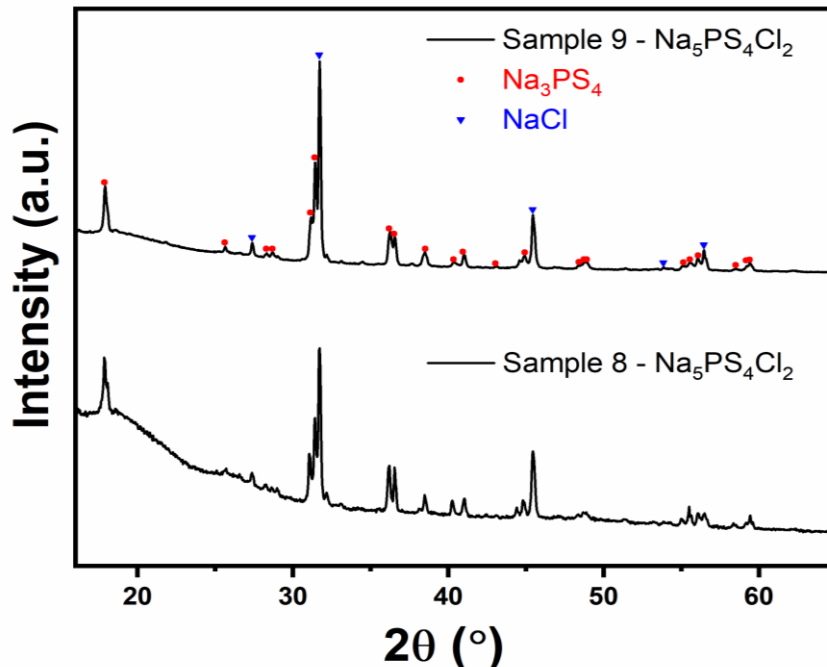


Figure 5.20 XRD patterns (flat stage) for sample eight and sample nine from **Table 5.11**. Solid black line shows observed pattern for targeted $\text{Na}_5\text{PS}_4\text{Cl}_2$. Na_3PS_4 and NaCl peaks are identified with red circles and blue triangles, respectively.

Afterwards, a small amount of Na doping was attempted with simultaneous halogen doping in the anion site (composition: $\text{Li}_{5.72}\text{Na}_{0.03}\text{PS}_{4.75}\text{Cl}_{1.25}$). Several heating programs were explored which are tabulated in **Table 5.12** and the final products were characterized by XRD. Heat treatment parameters were optimized in order to obtain a phase pure product.

Selected XRD patterns (Sample 3 and sample 5) are presented in **Figure 5.21**. Samples 1 - 4 showed small amounts of LiCl and Li_3PO_4 impurities. Sample 5 showed no impurities in the XRD pattern. The corresponding heat-treatment procedure was repeated three times to check the reproducibility. This pure single-phase sample was characterized by impedance spectroscopy (**Figure 5.22**) and exhibited an ionic conductivity of $5.4 \text{ mS}\cdot\text{cm}^{-1}$ which is higher than that of $\text{Li}_{5.75}\text{PS}_{4.75}\text{Cl}_{1.25}$ (σ : $4.2 \text{ mS}\cdot\text{cm}^{-1}$).

Table 5.12 Various preparation methods for $\text{Li}_{5.72}\text{Na}_{0.03}\text{PS}_{4.75}\text{Cl}_{1.25}$ phase.

Sample	Ballmill speed and length	Ramp	Heat treatment temperature and holding time	Cool
1	380 rpm, 16.5 h	18 h	550°C, 24 h	20 h
2	380 rpm, 16.5 h	17.5 h	550°C, 6 h	17.5 h
3	380 rpm, 16.5 h	15 h	550°C, 7 h	15 h
4	380 rpm, 16.5 h	17.5 h	550°C, 5 h	17.5 h
5	380 rpm, 16.5 h	15 h	550°C, 7 h	17.5 h

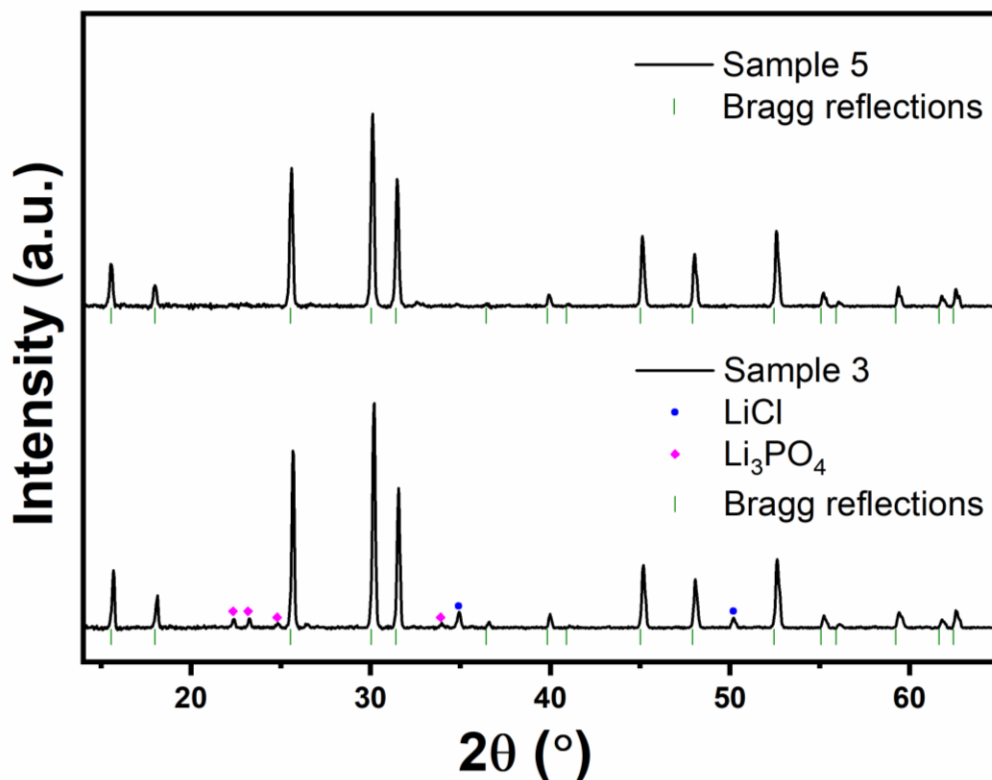


Figure 5.21 XRD patterns (flat stage) for sample three and sample five from **Table 5.12**. Solid black line shows observed pattern for targeted $\text{Li}_{5.72}\text{Na}_{0.03}\text{PS}_{4.75}\text{Cl}_{1.25}$. LiCl and Li_3PO_4 impurity peaks are identified with blue circles and magenta diamonds, respectively. Bragg reflections are shown by the green vertical ticks.

Due to the time restrictions, further Na doping to find the limit of the solid solution was not attempted and can be the subject of a future experimental or computational study.

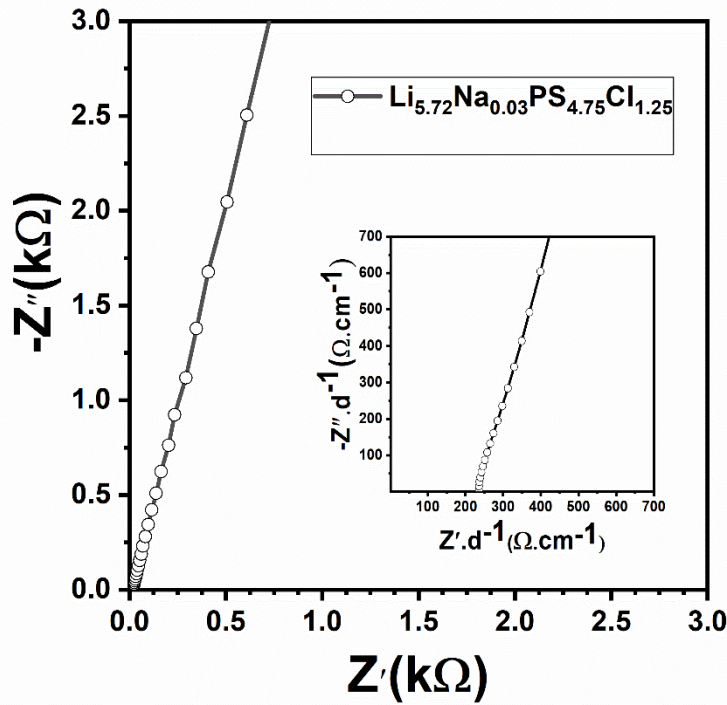
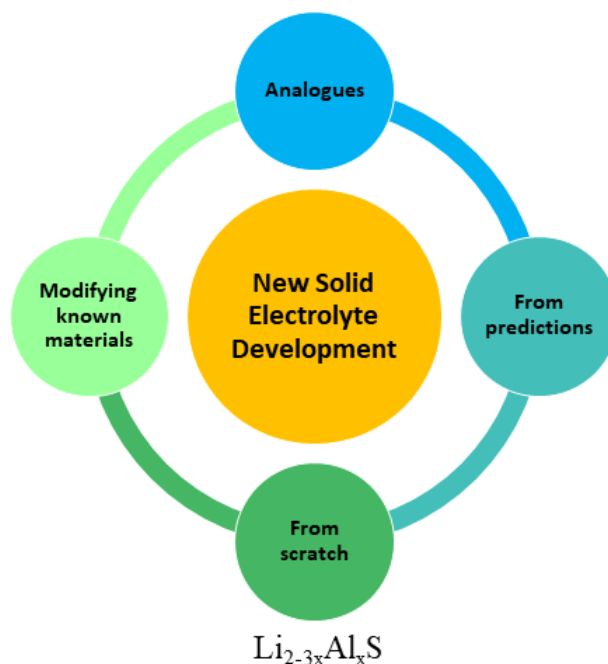


Figure 5.22 Impedance plot of the cold-pressed pellet (2 tons) of $\text{Li}_{5.72}\text{Na}_{0.03}\text{PS}_{4.75}\text{Cl}_{1.25}$ at 298 K. Inset denotes magnified view at high frequencies. Impedance was normalized to the pellet thickness (0.640 mm).

For full Na substitution, considering the larger ionic radius of Na (1.02) compared to Li (0.76), formation of $\text{Na}_6\text{PS}_5\text{M}$ (M = Br, I) or $\text{Na}_6\text{PSeS}_4\text{Br}$ (reflecting on chapter 4 of this thesis) could be more likely and a subject for future experimental exploration. Also, other synthesis approaches such as quenching the tube in ice water right after the high-temperature isothermal time step could be investigated for potentially attaining the Na argyrodite framework.

Chapter 6 Discovering New Solid Electrolytes



Single crystal measurements of targeted $\text{Na}_2\text{Al}_2\text{P}_3\text{S}_{11}\text{Cl}$ were carried out by Dr. J. Assoud (Crystallographer at UWaterloo).

This section summarizes efforts for finding new solid electrolytes. The term glass in this chapter refers to an amorphous material.

6.1 Li-based System: Li-Al-S Glass

6.1.1 Introduction

Inorganic glassy solid electrolytes are highly promising for application to all-solid-state batteries because of their several advantages in comparison with the crystalline solid electrolytes: a wide selection of compositions, isotropic properties, no grain boundaries, easy film formation

and so on.^[146] On the other hand, solid state ceramic electrolytes are safe to use at very high temperatures due to the intrinsic thermal stability of ceramics.^[147]

A material may show either better or worst conductivity in the glass form compared to glass-ceramic state. Masahiro's group in Japan has reported that the conductivity of their crystallized $\text{Li}_2\text{S-SiS}_2$ -based sulfide sample was lowered by at least two orders of magnitude after heating up above the crystallization temperature (T_c) compared to the original glass at room temperature. However, they noticed a different behavior for their $\text{Li}_2\text{S-P}_2\text{S}_5$ -based glass samples. After the latter system is heated up beyond T_c , the ionic conductivity was improved to higher values of $0.6 \text{ mS}\cdot\text{cm}^{-1}$ for the crystalline solid electrolyte (vs. $0.1 \text{ mS}\cdot\text{cm}^{-1}$ for the glass at room temperature).^[148] The chemical composition of the solid electrolyte and the morphology of the final phase also influence the conductivity.

In this section, with the aim of discovering new solid electrolytes, Li-Al-S system was studied and is briefly discussed. This idea was inspired from a 2015 patent^[149] regarding atomic layer deposition (ALD) method of $\text{Li}_x\text{Al}_y\text{S}$ film production for stabilizing Li metal anode. The lithium aluminum sulfide film reported in the patent exhibited a very low ionic conductivity on the order of $10^{-4} \text{ mS}\cdot\text{cm}^{-1}$. The same authors have published a paper^[150] in 2016 based on their patent, reporting the same conductivities. Here, $\text{Li}_{2-3x}\text{Al}_x\text{S}$ compositions were targeted as potential solid electrolytes and the products were characterized via EIS.

6.1.2 Material Synthesis and Results

Li_2S (Sigma-Aldrich, 99.98%) and Al_2S_3 (received directly from BASF, Germany as part of collaboration) were used as starting precursors. The precursors were ball milled at 370 rpm for 20 h. The ball milled materials were redeemed in the Ar-filled glovebox and had a khaki color. Three

compositions ($\text{LiAl}_{0.33}\text{S}$, $\text{Li}_{1.55}\text{Al}_{0.15}\text{S}$, $\text{Li}_{0.65}\text{Al}_{0.45}\text{S}$) were synthesized among which $\text{LiAl}_{0.33}\text{S}$ exhibited the highest ionic conductivity of $0.08 \text{ mS}\cdot\text{cm}^{-1}$ (σ at 25°C , for cold-pressed pellets at 3 ton). Ball milled $\text{LiAl}_{0.33}\text{S}$ mixture was heat treated at 240°C for 2 h and the conductivity dropped

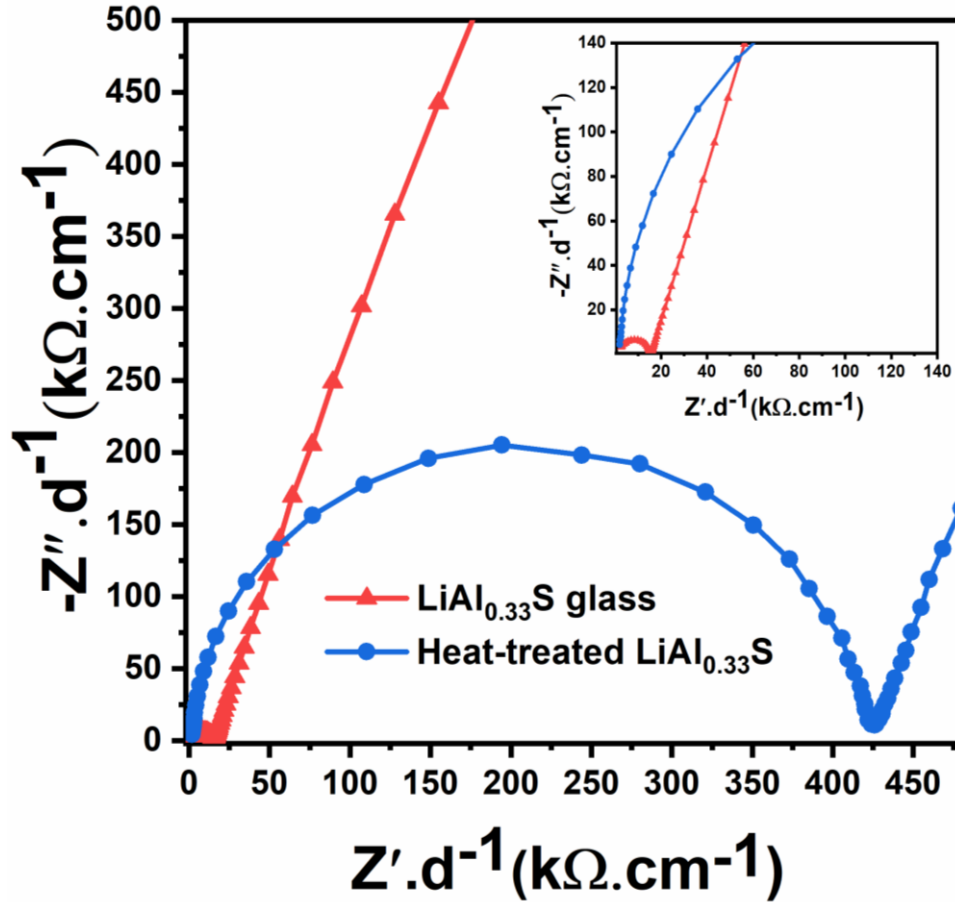


Figure 6.1 Room temperature Nyquist plots for $\text{LiAl}_{0.33}\text{S}$ glass and heat-treated $\text{LiAl}_{0.33}\text{S}$. Impedance is normalized to the respective pellet thickness for better comparison. Inset displays magnified view at high frequencies.

from $0.08 \text{ mS}\cdot\text{cm}^{-1}$ for glass to $0.003 \text{ mS}\cdot\text{cm}^{-1}$ for the heat-treated material (see **Figure 6.1** for impedance plots). Understanding the underlying behavior of the Li-Al-S system requires further characterization of the material which was not pursued as part of this work.

6.2 Na-based Systems: Na-Zr-P-S, Na-Al-P-S and Na-Y-P-S

6.2.1 Introduction

In recent years, Na-ion batteries have garnered tremendous interest as an alternative to Li-ion batteries because of sodium's low cost and natural abundance.^[151-154] Current Na-ion electrolytes are very similar to non-aqueous Li-ion electrolytes, which are flammable organic liquids and have limited electrochemical stability window (< 4.5 V). A promising alternative is all-solid-state Na-ion batteries that utilize Na-ion conducting ceramic electrolytes offering wide electrochemical window (> 5 V) and high thermal stability.^[155] The development of all-solid-state batteries still falls short of expectations due to the lack of suitable solid electrolytes required for practical applications, with most present-day Na solid electrolytes only exhibiting good ionic conductivities at elevated temperatures. If solid-state Na-ion batteries are to be competitive for stationary energy storage systems, they must encompass high performance i.e., high conductivity at room temperature.^[147] In 2012, a major milestone was achieved towards practical Na-ion solid conductors by the report of glass-ceramic Na₃PS₄ exhibiting 0.2 mS.cm⁻¹ at ambient temperature owing to the stabilization of Na₃PS₄'s cubic high-temperature phase. This sulfide electrolyte was employed in an all-solid-state Na battery and a room temperature rechargeable Na battery was realized.^[147] Sulfide systems are particularly interesting due to their high room temperature ionic conductivity compared to the oxide analogues. This stems from the large size and high polarizability of sulfide (S²⁻) ions which open up the bottlenecks for ion migration. Moreover, they possess low grain boundary impedance and are easy to process into thin electrolyte membrane by simple cold pressing.

This section describes the efforts that were made to develop a novel sulfide electrolyte based on the Na-Zr-P-S system (**Figure 6.2**) and the electrochemical performance for glass, glass

ceramic and ceramic compositions of the mentioned system were explored to determine which composition exhibits the best conductivity value at room temperature.

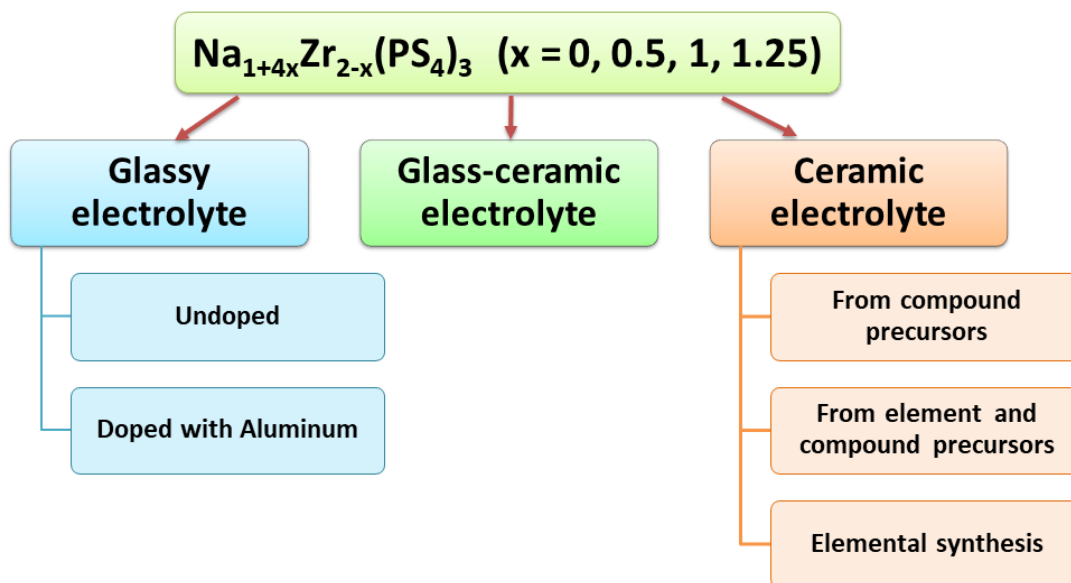


Figure 6.2 Schematic of experimental procedure carried out for Na-Zr-P-S system.

6.2.2 Material Synthesis and Characterization

Precursor preparation: Zirconium Sulfide (ZrS_2) powder which is one of the main precursors was prepared in house via solid-state route. Zirconium (Strem Chemicals Inc.) and sulfur (Sigma-Aldrich, 99.998%) were placed in a quartz tube in an Ar-filled glovebox. The tube containing the mixture was vacuum-sealed and heat-treated at 900°C for seven days.^[156] Zirconium melting point is 1855°C therefore the element precursors were held at 900°C for seven days in order to allow the solid state reaction to slowly occur. After the heat treatment, the tube was opened inside the argon-filled glovebox to redeem the powder for XRD measurements. For XRD measurement, ZrS_2 powder was mounted on a zero-background holder (ZBH) via grease. Kapton film was used as a moisture-protective barrier.

Glass Compositions Preparation: In order to prepare $\text{Na}_{1+4x}\text{Zr}_{2-x}(\text{PS}_4)_3$ ($x = 0, 0.5, 1, 1.25$) glasses, appropriate amounts of the compound precursors Na_2S (Sigma-Aldrich, X%), P_2S_5 (Sigma-Aldrich, 99%) and ZrS_2 (synthesized in-house) were mixed and transferred to the ball mill jars in an Ar-filled glovebox. Milling was performed in a planetary ball-mill (Fritsch™ Pulverisette 7 Premium Line) up to 12 h at 500 rpm under Ar atmosphere. After redeeming the powder, XRD (sample was prepared on a ZBH) was utilized to confirm the presence of a pure glass phase, followed by pelletization (under 25 MPa) and temperature-dependent ionic conductivity measurements. The ionic conductivities of these glasses were determined in a Swagelok® cell using EIS. EIS measurements were performed over the range of 100 mHz to 1 MHz and at 25°C to 200°C. Aluminum Sulfide (granular, 98%, Aldrich) was used as the precursor in the Al-substituted glass materials targeting $\text{Na}_2\text{AlZr}(\text{PS}_4)_3$ and $\text{Na}_3\text{Al}_2(\text{PS}_4)_3$ compositions.

Glass-Ceramic Composition: For preparing glass-ceramic conductors for the above-noted compositions, glasses obtained via mechanochemical reaction were subjected to controlled heat treatment.

Ceramic Composition:

From Compound Precursor: Alternative synthesis procedures were pursued to avoid the glass phase formation through direct high temperature solid-state reaction of relevant precursors for the preparation of crystalline superionic conductors. Compound precursors, which are Na_2S (Sigma-Aldrich, X%), P_2S_5 (Sigma-Aldrich, 99%) and ZrS_2 were mixed in a mortar inside an Ar-filled glove box. Then the powder mixture was pressed in a cylindrical die under a force of 6 tons for two minutes in the glovebox. Following that, the obtained pellets were transferred to a quartz tube, and vacuum sealed with a torch. Afterwards, the tube was heat treated in a tube furnace at different temperature steps based on the melting point of the precursors. The quartz tubes were carbon

coated prior to use to inhibit the reaction of sodium with the quartz tube. After heat treatment, the pellets were crushed and ground and then prepared for XRD measurement.

From Element-compound Mix Precursor: Synthesis via solid-state method was implemented in a sealed quartz tube from a mixture of elemental precursors and compound precursors.

Elemental Synthesis: For the solid-state synthesis of ceramic solid electrolytes from elements; metallic sodium, sulfur, red phosphorous and zirconium were mixed in a glassy carbon crucible (SIGRADUR G) and then the crucible was placed in a quartz tube in an Ar-filled glovebox. The tube was sealed under vacuum and transferred to a tube furnace for heat treatment. Schematic of the performed heat treatments are shown in **Figure 6.3** and **Figure 6.4**. The first heat treatment was performed based on temperatures held at each precursor's melting point to allow sufficient time for the precursors to completely melt and react.

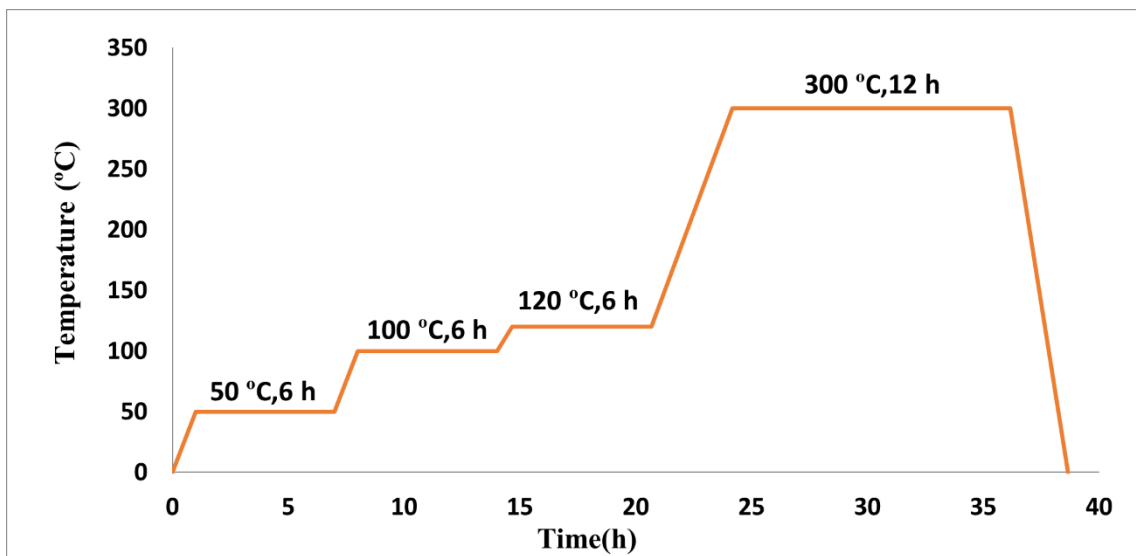


Figure 6.3 Heat treatment procedure of targeted $\text{Na}_{1+4x}\text{Zr}_{2-x}(\text{PS}_4)_3$ synthesized from elements.

The second heat treatment was carried out based on the paper by S. Coste *et al*, in which they report successful synthesis of $\text{Na}_3\text{Cr}_2\text{P}_3\text{S}_{12}$.^[157]

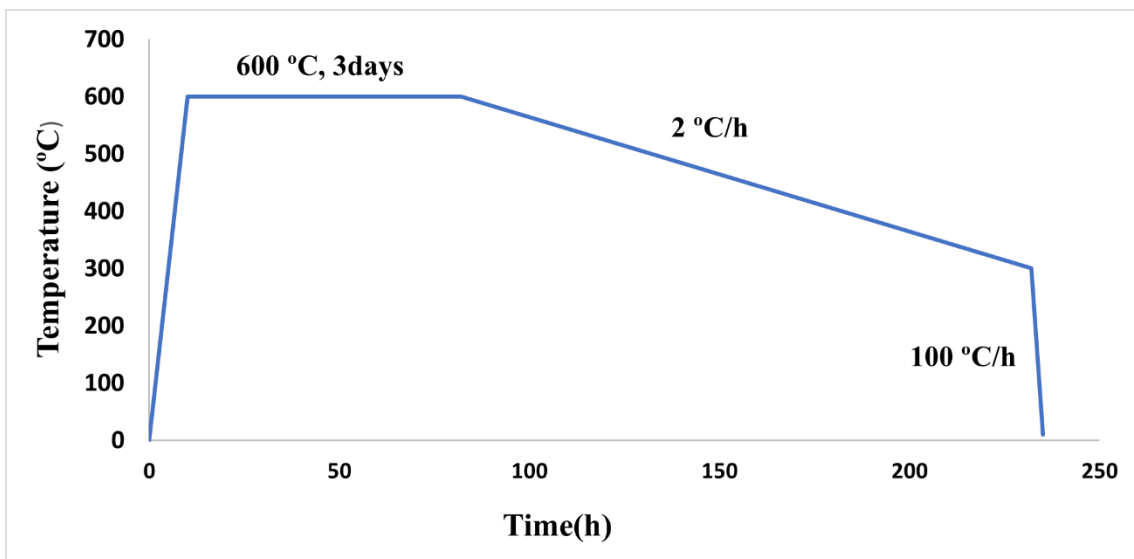


Figure 6.4 Heat treatment procedure of targeted $\text{Na}_{1+4x}\text{Zr}_{2-x}(\text{PS}_4)_3$ synthesized from elements.

6.2.3 Results and Discussion

ZrS_2 precursor powder was synthesized in-house via solid state route. The colour of synthesized ZrS_2 powder was a violet brown as expected. Formation of ZrS_2 material was confirmed by XRD pattern (**Figure 6.5**). The common impurity present in the synthesized ZrS_2 samples is ZrS_3 which has an orange like color. This was separated from ZrS_2 prior to proceeding to the next step.

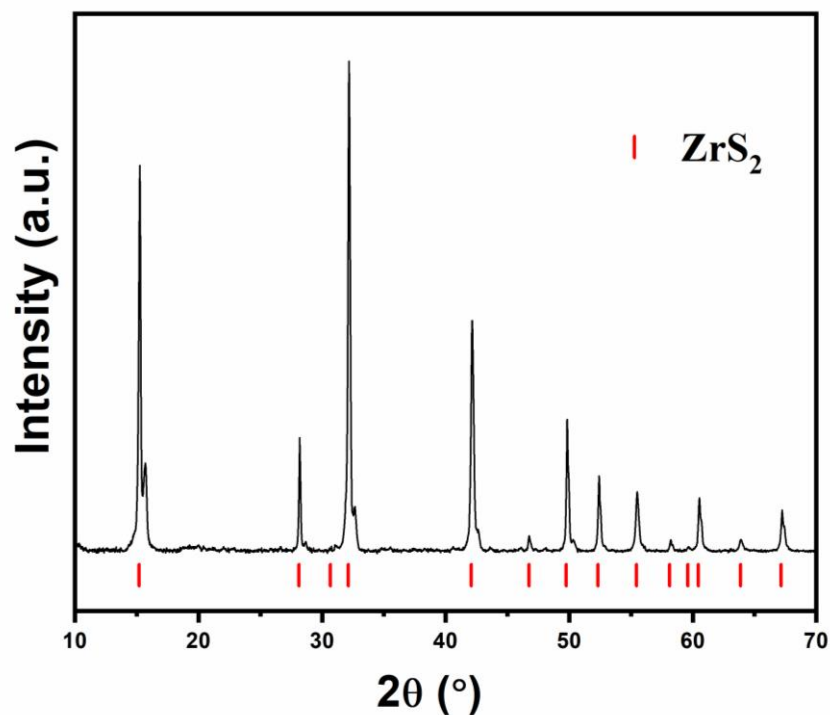


Figure 6.5 XRD pattern of the synthesized ZrS_2 .

6.2.3.1 $\text{Na}_{1+4x}\text{Zr}_{2-x}(\text{PS}_4)_3$ ($x = 0, 0.5, 1, 1.25$) glass materials

Potential solid electrolytes were investigated by systematically synthesizing and characterizing glassy, glass ceramic and ceramic compositions of $\text{Na}_{1+4x}\text{Zr}_{2-x}(\text{PS}_4)_3$ ($x = 0, 0.5, 1, 1.25$). The $\text{NaZr}_2(\text{PS}_4)_3$ and $\text{Na}_5\text{Zr}(\text{PS}_4)_3$ glass materials had a brick red and mustard colour after milling, respectively. The XRD measurements ascertain the presence of amorphous glasses. Selective XRD patterns for $\text{NaZr}_2(\text{PS}_4)_3$ and $\text{Na}_5\text{Zr}(\text{PS}_4)_3$ glasses are shown in **Figure 6.6** and **Figure 6.7**.

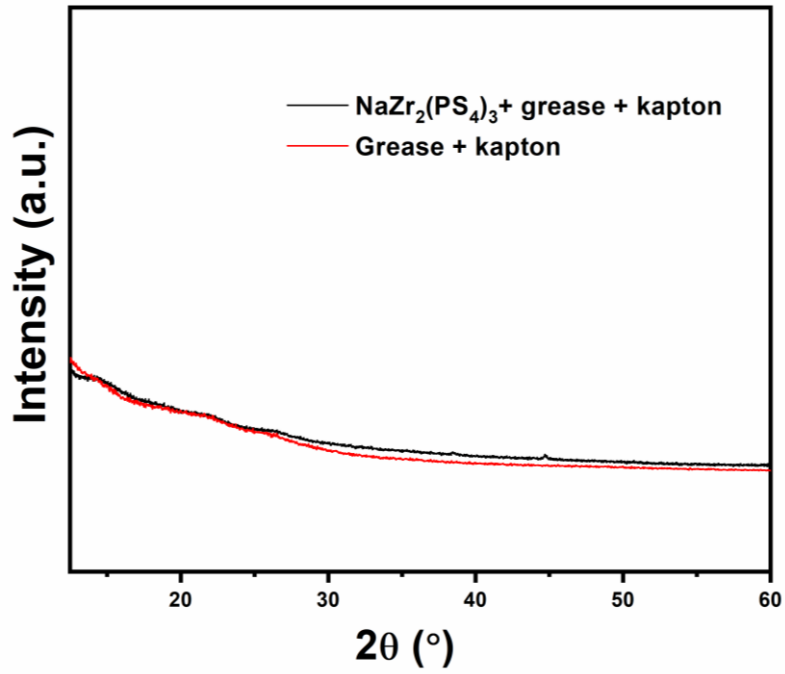


Figure 6.6 XRD pattern of $\text{NaZr}_2(\text{PS}_4)_3$ glass.

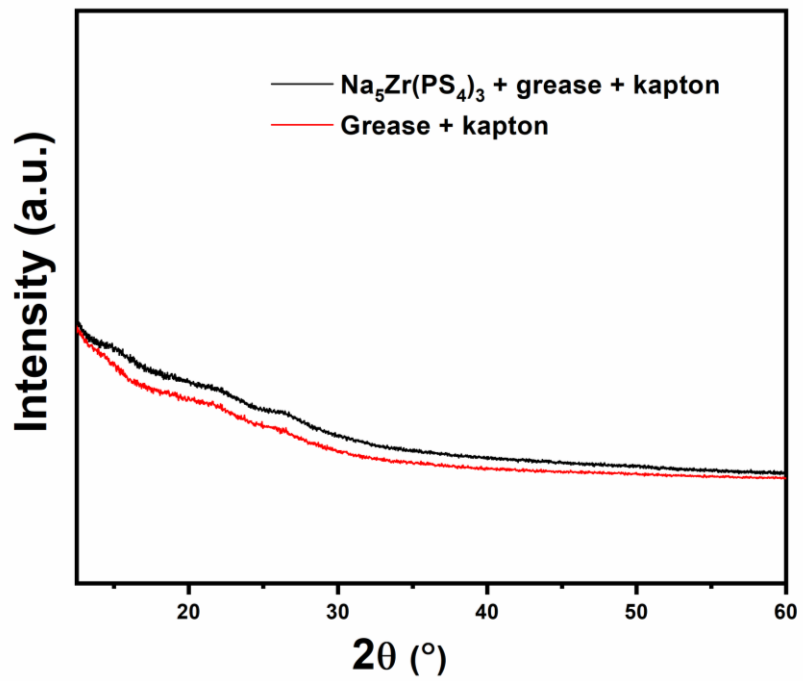


Figure 6.7 XRD pattern of $\text{Na}_5\text{Zr}(\text{PS}_4)_3$ glass.

EIS measurements were carried out for $\text{Na}_{1+4x}\text{Zr}_{2-x}(\text{PS}_4)_3$ ($x = 0, 0.5, 1, 1.25$). All the Na glasses exhibit rather low ionic conductivities $10^{-7} - 10^{-5} \text{ S.cm}^{-1}$ at room temperature. Selective Nyquist plots of the impedance diagram for $\text{Na}_6\text{Zr}_{0.75}(\text{PS}_4)_3$ glass are shown in **Figure 6.8**. It is noted that as the temperature rises, the bulk conductivity of the solid electrolyte increases. By comparing the ionic conductivity data obtained from all the synthesized glass materials (**Figure 6.9**), It is observed that increasing the Na content leads to better bulk ionic conductivity.

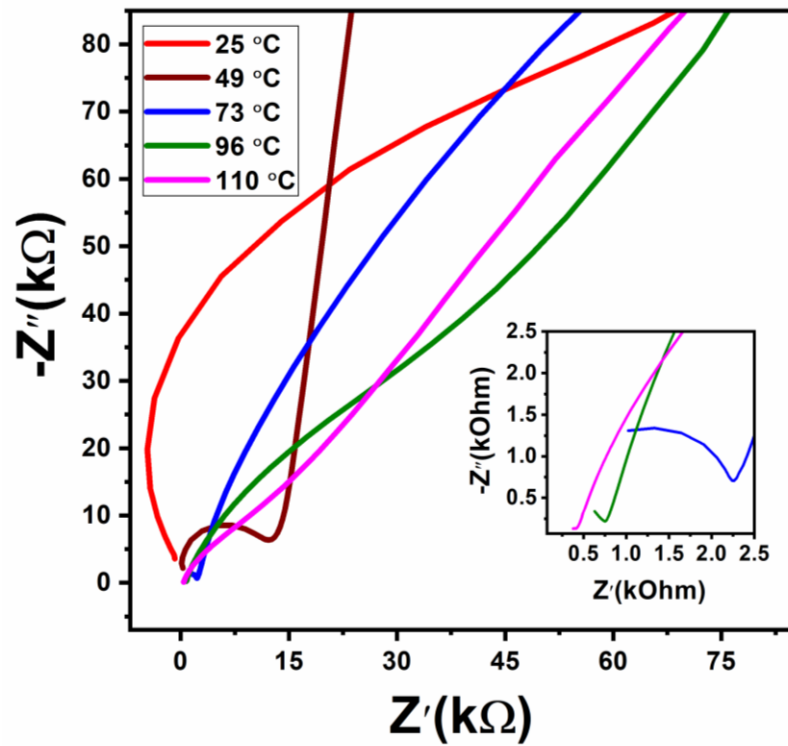


Figure 6.8 Nyquist plots of the impedance diagram for $\text{Na}_6\text{Zr}_{0.75}(\text{PS}_4)_3$ in the frequency range 100 mHz to 1 MHz. Inset displays magnified view at high frequencies.

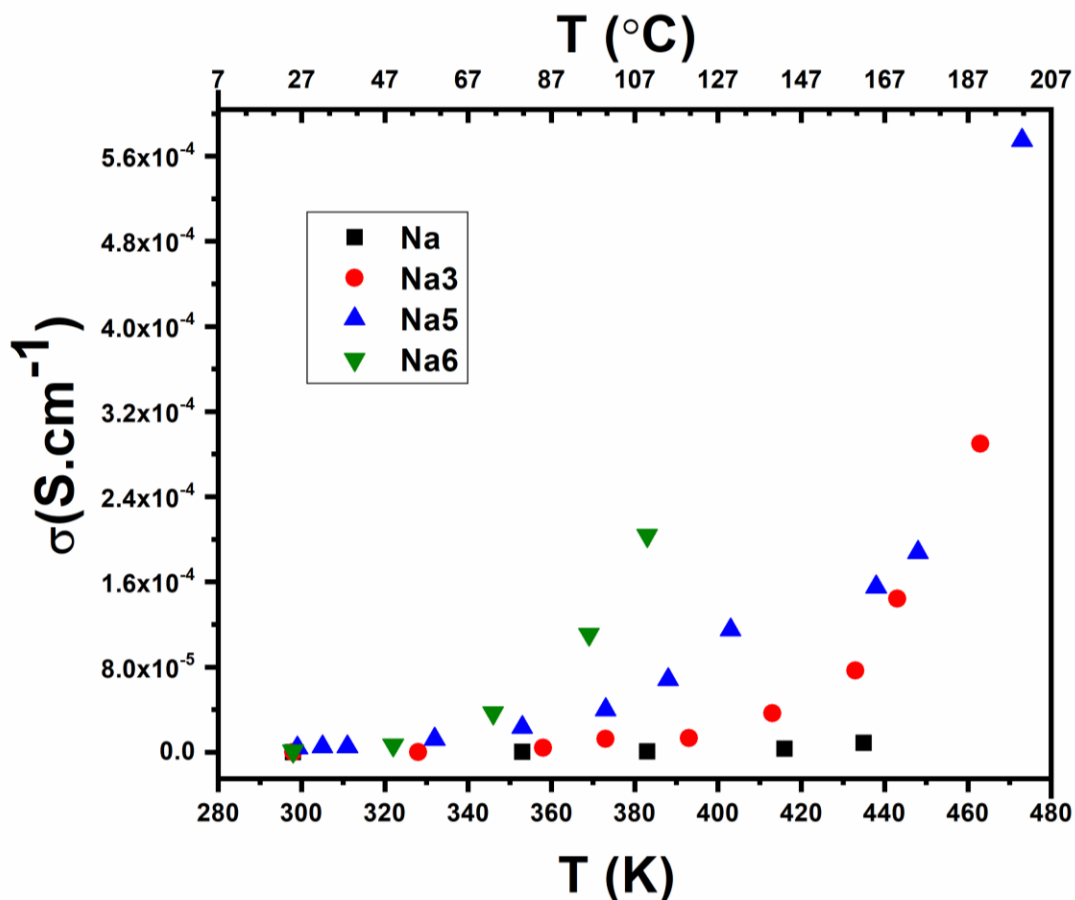


Figure 6.9 Comparison of ionic conductivities for the $\text{Na}_{1+4x}\text{Zr}_{2-x}(\text{PS}_4)_3$ ($x = 0, 0.5, 1, 1.25$) synthesized glass materials.

Targeted $\text{Na}_{1+4x}\text{Zr}_{2-x}(\text{PS}_4)_3$ ($x = 0, 0.5, 1, 1.25$) mixtures were subject to different heat treatment procedures as described in section **6.2.2** Material Synthesis and Characterization. Nevertheless, these efforts were not fruitful towards forming a thio-NASICON structure. Selective XRD pattern for $\text{Na}_5\text{Zr}(\text{PS}_4)_3$ for three different heat treatment procedures (500 $^{\circ}\text{C}$, hold 10 h; 500 $^{\circ}\text{C}$, hold 4 days and 600 $^{\circ}\text{C}$, hold 11 h) are provided in **Appendix C** - Supplementary Information for Chapter 6 (**Figure C.1**).

6.2.3.2 Na₃Al₂(PS₄)₃

Aluminum doping in the zirconium site was carried out to determine the effect on the glass ionic conductivities by targeting Na₂AlZr(PS₄)₃ and Na₃Al₂(PS₄)₃ compositions. Cl doping was also attempted (Na_{2.25}Al₂P₃S_{11.25}Cl_{0.75} and Na₂Al₂P₃S₁₁Cl) by ball milling (Na₂S + P₂S₅ + Al₂S₃ + NaCl). After heat treating (650°C, 6 days followed by slow cooling) amorphous mixture of Na₂Al₂P₃S₁₁Cl, the product consisted of a yellow plate like crystal, an orange crystal, and some grey residue. The yellow crystal was determined to be AIPS₄ via single crystal diffraction and

Table 6.1 Summary of room temperature ionic conductivities and preparation methods for targeted compositions. HT stands for heat treated.

Composition		Conductivity (S.cm ⁻¹)	Preparation method
Na ₆ Zr _{0.75} (PS ₄) ₃	glass	8.3 x 10 ⁻⁷	500 rpm, 12.5 h
Na ₃ Al ₂ (PS ₄) ₃	glass	4.8 x 10 ⁻⁷	500 rpm, 12.5 h
Na _{2.88} Al ₂ Zr _{0.03} (PS ₄) ₃	HT 650°C, 3 days, 36 h ramp, 90 h cool	6.8 x 10 ⁻⁶	500 rpm, 15 h
Na ₂ AlZr(PS ₄) ₃	glass	6 x 10 ⁻⁷	500 rpm, 12.5 h
Na _{2.25} Al ₂ P ₃ S _{11.25} Cl _{0.75}	glass	1.6 x 10 ⁻⁷	500 rpm, 13.5 h
Na ₆ Y ₃ (PS ₄) ₅	glass	1.6 x 10 ⁻⁷	500 rpm, 20 h
Na ₆ Y ₃ (PS ₄) ₅	glass	5.5 x 10 ⁻⁷	500 rpm, 13.5 h
Na ₆ Y ₃ (PS ₄) ₅	HT 500°C, 168 h, 36 h ramp, 99 h cool	5 x 10 ⁻⁶	550 rpm, 20 h
Na ₆ Y ₂ La(PS ₄) ₅	glass	2.3 x 10 ⁻⁷	500 rpm, 20 h

EDX analysis. The orange crystal showed a phase that included all the elements in the aimed composition during EDX. The corresponding conductivity results for some of the glasses and heat-treated materials are summarized in **Table 6.1**.

6.2.3.3 Na-Y-P-S glass

The Li-Y-P-S system has been the subject of theoretical and experimental studies in the search for potential solid electrolytes. $\text{Li}_6\text{Y}_3(\text{PS}_4)_5$ phase has been synthesized but this phase exhibits a low ionic conductivity on the order of $10^{-3} \text{ mS}\cdot\text{cm}^{-1}$.^[158] In 2017, Ong *et al.* reported that $\text{Li}_3\text{Y}(\text{PS}_4)_2$ phase possesses an ionic conductivity of $2.16 \text{ mS}\cdot\text{cm}^{-1}$ at room temperature on the basis of ab initio MD simulations with the potential to further enhance the conductivity by aliovalent doping of Ca^{2+} or Zr^{4+} in the Yttrium site.^[159] Nevertheless, to date, no report exists on the successful formation of that specific phase. As part of this thesis, the Na-Y-P-S glass and heat-treated materials were studied as a potential solid electrolyte, but the targeted compositions exhibited low ionic conductivities ($10^{-7} - 10^{-5} \text{ S}\cdot\text{cm}^{-1}$, see **Table 6.1**).

6.2.4 Summary

New lithium- and sodium-based glassy materials were systematically targeted and investigated in depth. Among the lithium-based glasses, $\text{LiAl}_{0.33}\text{S}$ exhibited the best conductivity of $\sigma = 0.08 \text{ mS}\cdot\text{cm}^{-1}$. Different compositions of $\text{Na}_{1+4x}\text{Zr}_{2-x}(\text{PS}_4)_3$ ($x = 0, 0.5, 1, 1.25$) glasses were prepared through mechanochemical reaction of the relevant precursors. In addition, Al^{3+} doping for Zr^{4+} , was explored. However, these materials exhibited poor ionic conductivity which makes them not viable for practical solid electrolyte applications.

Thesis Perspective

One of the head winds facing the progress of solid-state batteries is the lack of solid electrolytes with excellent Li ion transport properties. Throughout this thesis, various methods were implemented to enhance the ionic conductivity of solid electrolyte materials at room temperature among other research topics. These methods include aliovalent doping or substitution, changing distribution of halide (site disorder), optimizing synthesis approach (temperature, holding time, cooling rate), densification and post treatments (sintering cold pressed pellets and optimizing grain boundary conductivity).

For superionic argyrodites, aliovalent cation (Ca, Al, Ga) doping for Li^+ was studied as a means of increasing the vacancy population. Various amounts of dopants $\text{Li}_{6-2y}\text{Ca}_y\text{PS}_5\text{Cl}$ ($y = 0.05, 0.1, 0.15, 0.2$) and $\text{Li}_{6-x-3y}\text{M}_y\text{PS}_{5-x}\text{Cl}_{1+x}$ (M: Al or Ga and $y = 0.05, 0.1, 0.15, 0.2$) were attempted. Additionally, effect of Substitution of S^{2-} for Cl^- in $\text{Li}_6\text{PS}_5\text{Cl}$ was systematically studied ($\text{Li}_{6-x}\text{PS}_{5-x}\text{Cl}_{1+x}$ where $x = 0, 0.25, 0.375, 0.5, 0.55, 0.6$). Furthermore, impact of dual modification (aliovalent cation doping for Li^+ and increasing the Cl^- content simultaneously) were investigated in this class of materials. Effect of anion (Se) substitution for sulfur was studied as well ($\text{Li}_6\text{PS}_{5-x}\text{Se}_x\text{Cl}$ where $x = 0.5, 0.75, 1, 2, 2.5, 4, 5$). While all the implemented strategies for the argyrodite materials had a positive impact on the ionic conductivity, it was observed that increasing the $\text{Cl}^-/\text{S}^{2-}$ ratio was individually most effective. Substitution of S^{2-} for Cl^- in $\text{Li}_6\text{PS}_5\text{Cl}$ results in an almost exponential increase of ionic conductivity vs x in $\text{Li}_{6-x}\text{PS}_{5-x}\text{Cl}_{1+x}$ and the Cl-rich phase $\text{Li}_{5.5}\text{PS}_{4.5}\text{Cl}_{1.5}$ ($\text{Cl}^-/\text{S}^{2-}$ ratio $\frac{1+x}{5-x} = 0.33$) exhibits almost quadrupled ionic conductivity of $9.4 \pm 0.1 \text{ mS}\cdot\text{cm}^{-1}$ compared to $\text{Li}_6\text{PS}_5\text{Cl}$ ($\sigma = 2.5 \pm 0.1 \text{ mS}\cdot\text{cm}^{-1}$). As previously mentioned, halogen disorder is advantageous for the intercalation jump which determines the long-range Li ion diffusion.

Nevertheless, when the most effective strategy (increasing the $\text{Cl}^-/\text{S}^{2-}$ ratio) was combined with aliovalent (Ca^{2+}) doping, the overall performance enhanced slightly ($\sigma = 10.2 \text{ mS cm}^{-1}$ for $\text{Li}_{5.35}\text{Ca}_{0.1}\text{PS}_{4.5}\text{Cl}_{1.55}$).

In this thesis, a deep understanding of lithium argyrodites and their composition-structure-property relationship was developed for solid-state batteries. Superionic electrolytes were designed and by tuning their structure, ionic conductivities up to 12 mS.cm^{-1} were achieved.

Future Perspective for the ASSB Field

Nowadays, the world is witnessing an electrification revolution. Energy storage research is greatly motivated by the need to decrease dependency on fossil fuels generation and enhancing sustainable transportation. Battery electric vehicles (EVs) indicate great potential for sustained mobility in the path to a clean energy future but their large-scale application hinges on safe chemistries such as solid-state batteries who are not plagued by leakage or flammability as they utilize solid electrolytes in lieu of organic liquid electrolytes. Designing practical solid-state batteries requires a holistic approach towards developing its several components from electrodes to interface to cell fabrication and pack level. Original Equipment Manufacturers (OEMs) are working meticulously on developing solid-state batteries either in-house or in collaboration with battery manufacturers. Toyota Motor Corporation as an example is an OEM working on developing solid-state batteries for their EVs which employ sulfide-based solid electrolytes. Sulfide and oxide solid electrolytes each have their own advantages and disadvantages and research is ongoing to select the best candidates. After achieving the optimal materials, there exists the scale-up challenge along with cost, safety, and long-term performance. There is indeed a long arduous way from laboratory materials to pilot-scale and industrial-scale products. However, with these concerted efforts across the globe, ASSBs that can ensure safety and long cycle life with minimal capacity fade seem to be the future of automotive applications.

References

- [1] Goodenough, J. B. & Kim, Y. Challenges for rechargeable Li batteries. *Chem. Mater.* **22**, 587–603 (2010).
- [2] Foundations for the future. *Nat. Energy* **1**, 16147 (2016).
- [3] Goodenough, J. B. & Park, K. S. The Li-ion rechargeable battery: A perspective. *J. Am. Chem. Soc.* **135**, 1167–1176 (2013).
- [4] Li, W., Song, B. & Manthiram, A. High-voltage positive electrode materials for lithium-ion batteries. *Chem. Soc. Rev.* **46**, 3006–3059 (2017).
- [5] Andre, D., Hain, H., Lamp, P., Maglia, F. & Stiaszny, B. Future high-energy density anode materials from an automotive application perspective. *J. Mater. Chem. A* **5**, 17174–17198 (2017).
- [6] Masaki Yoshio, H. N. *Lithium-Ion Batteries, Chapter 2. A Review of Positive Electrode Materials for Lithium-Ion Batteries* (Springer, 2009).
- [7] Norman Shiau, C. S. *et al.* Optimal plug-in hybrid electric vehicle design and allocation for minimum life cycle cost, petroleum consumption, and greenhouse gas emissions. *J. Mech. Des. Trans. ASME* **132**, 091013 (2010).
- [8] Hoffert, M. I. *et al.* Engineering: Advanced technology paths to global climate stability: Energy for a greenhouse planet. *Science* **298**, 981–987 (2002).
- [9] Jung, Y. S., Oh, D. Y., Nam, Y. J. & Park, K. H. Issues and challenges for bulk-type all-solid-state rechargeable lithium batteries using sulfide solid electrolytes. *Isr. J. Chem.* **55**, 472–485 (2015).
- [10] S. Gallagher, Boeing’s Dreamliner batteries ‘inherently unsafe’—and yours may be too. *Ars Technica* (January, 2013); <http://arstechnica.com/business/2013/01/boeings-dreamliner-batteries-inherently-unsafe-and-yours-may-be-too>
- [11] F. Meier & C. Woodyard, Feds review third Tesla fire as shares fall again. *USA Today* (November, 2013); <http://www.usatoday.com/story/money/cars/2013/11/07/third-fire-in-tesla-model-s-reported/3465717>
- [12] Janek, J. & Zeier, W. G. A solid future for battery development. *Nat. Energy* **1**, 1–4 (2016).

-
- [13] Wang, Q. *et al.* A New Lithium-Ion Conductor LiTaSiO₅: Theoretical Prediction, Materials Synthesis, and Ionic Conductivity. *Adv. Funct. Mater.* **29**, 1904232 (2019).
- [14] Kitaura, H., Hayashi, A., Ohtomo, T., Hama, S. & Tatsumisago, M. Fabrication of electrode-electrolyte interfaces in all-solid-state rechargeable lithium batteries by using a supercooled liquid state of the glassy electrolytes. *J. Mater. Chem.* **21**, 118–124 (2011).
- [15] Tatsumisago, M., Nagao, M. & Hayashi, A. Recent development of sulfide solid electrolytes and interfacial modification for all-solid-state rechargeable lithium batteries. *J. Asian Ceram. Soc.* **1**, 17–25 (2013).
- [16] Maekawa, H. *et al.* Halide-stabilized LiBH₄, a room-temperature lithium fast-ion conductor. *J. Am. Chem. Soc.* **131**, 894–895 (2009).
- [17] Goodenough, J. B. & Singh, P. Review—Solid Electrolytes in Rechargeable Electrochemical Cells. *J. Electrochem. Soc.* **162**, A2387–A2392 (2015).
- [18] Park, K. H. *et al.* Design Strategies, Practical Considerations, and New Solution Processes of Sulfide Solid Electrolytes for All-Solid-State Batteries. *Adv. Energy Mater.* **8**, 1800035 (2018).
- [19] Robertson, A., West, A. & Ritchie, A. Review of crystalline lithium-ion conductors suitable for high temperature battery applications. *Solid State Ionics* **104**, 1–11 (1997).
- [20] Li, Y. *et al.* A Perovskite Electrolyte That Is Stable in Moist Air for Lithium-Ion Batteries. *Angew. Chemie - Int. Ed.* **57**, 8587–8591 (2018).
- [21] Dawson, J. A. *et al.* Elucidating lithium-ion and proton dynamics in anti-perovskite solid electrolytes. *Energy Environ. Sci.* **11**, 2993–3002 (2018).
- [22] Li, Y. *et al.* Hybrid Polymer/Garnet Electrolyte with a Small Interfacial Resistance for Lithium-Ion Batteries. *Angew. Chemie - Int. Ed.* **56**, 753–756 (2017).
- [23] Cao, C., Li, Z. Bin, Wang, X. L., Zhao, X. B. & Han, W. Q. Recent advances in inorganic solid electrolytes for lithium batteries. *Front. Energy Res.* **2**, 1–10 (2014).
- [24] Hong, H. Y. P. Crystal structure and ionic conductivity of Li₁₄Zn(GeO₄)₄ and other new Li⁺ superionic conductors. *Mater. Res. Bull.* **13**, 117–124 (1978).
- [25] Thangadurai, V. & Weppner, W. Recent progress in solid oxide and lithium ion conducting electrolytes research. *Ionics (Kiel)*. **12**, 81–92 (2006).
- [26] Stramare, S., Thangadurai, V. & Weppner, W. Lithium Lanthanum Titanates: A Review. *Chem. Mater.* **15**, 3974–3990 (2003).

-
- [27] Thangadurai, V., Kaack, H. & Weppner, W. J. F. Novel fast lithium ion conduction in garnet-type $\text{Li}_5\text{La}_3\text{M}_2\text{O}_{12}$ (M = Nb, Ta). *J. Am. Ceram. Soc.* **86**, 437–440 (2003).
- [28] Murugan, R., Thangadurai, V. & Weppner, W. Fast lithium ion conduction in garnet-type $\text{Li}_7\text{La}_3\text{Zr}_2\text{O}_{12}$. *Angew. Chemie - Int. Ed.* **46**, 7778–7781 (2007).
- [29] Bachman, J. C. *et al.* Inorganic Solid-State Electrolytes for Lithium Batteries: Mechanisms and Properties Governing Ion Conduction. *Chem. Rev.* **116**, 140–162 (2016).
- [30] Kumazaki, S. *et al.* High lithium ion conductive $\text{Li}_7\text{La}_3\text{Zr}_2\text{O}_{12}$ by inclusion of both Al and Si. *Electrochem. commun.* **13**, 509–512 (2011).
- [31] Bernuy-Lopez, C. *et al.* Atmosphere controlled processing of ga-substituted garnets for high li-ion conductivity ceramics. *Chem. Mater.* **26**, 3610–3617 (2014).
- [32] Rettenwander, D. *et al.* Site occupation of Ga and Al in stabilized cubic $\text{Li}_{7-3(x+y)}\text{Ga}_x\text{Al}_y\text{La}_3\text{Zr}_2\text{O}_{12}$ garnets as deduced from ^{27}Al and ^{71}Ga MAS NMR at ultrahigh magnetic fields. *Chem. Mater.* **27**, 3135–3142 (2015).
- [33] Bottke, P., Rettenwander, D., Schmidt, W., Amthauer, G. & Wilkening, M. Ion Dynamics in Solid Electrolytes: NMR Reveals the Elementary Steps of Li^+ Hopping in the Garnet $\text{Li}_{6.5}\text{La}_3\text{Zr}_{1.75}\text{Mo}_{0.25}\text{O}_{12}$. *Chem. Mater.* **27**, 6571–6582 (2015).
- [34] Rettenwander, D. *et al.* Structural and Electrochemical Consequences of Al and Ga Cosubstitution in $\text{Li}_7\text{La}_3\text{Zr}_2\text{O}_{12}$ Solid Electrolytes. *Chem. Mater.* **28**, 2384–2392 (2016).
- [35] Rettenwander, D., Geiger, C. A., Tribus, M., Tropper, P. & Amthauer, G. A synthesis and crystal chemical study of the fast ion conductor $\text{Li}_{7-3x}\text{Ga}_x\text{La}_3\text{Zr}_2\text{O}_{12}$ with $x = 0.08$ to 0.84 . *Inorg. Chem.* **53**, 6264–6269 (2014).
- [36] Wagner, R. *et al.* Crystal Structure of Garnet-Related Li-Ion Conductor $\text{Li}_{7-3x}\text{Ga}_x\text{La}_3\text{Zr}_2\text{O}_{12}$: Fast Li-Ion Conduction Caused by a Different Cubic Modification? *Chem. Mater.* **28**, 1861–1871 (2016).
- [37] Awaka, J., Kijima, N., Hayakawa, H. & Akimoto, J. Synthesis and structure analysis of tetragonal $\text{Li}_7\text{La}_3\text{Zr}_2\text{O}_{12}$ with the garnet-related type structure. *J. Solid State Chem.* **182**, 2046–2052 (2009).
- [38] Raskovalov, A., Il'Ina, E. & Antonov, B. Short communication Structure and transport properties of $\text{Li}_7\text{La}_3\text{Zr}_{2-0.75x}\text{Al}_x\text{O}_{12}$ superionic solid electrolytes. *J. Power Sources* **238**, 48–52 (2013).

-
- [39] Fu, J. Superionic conductivity of glass-ceramics in the system $\text{Li}_2\text{O}-\text{Al}_2\text{O}_3-\text{TiO}_2-\text{P}_2\text{O}_5$. *Solid State Ionics* **96**, 195–200 (1997).
- [40] Fu, J. Fast Li^+ ion conducting glass-ceramics in the system $\text{Li}_2\text{O}-\text{Al}_2\text{O}_3-\text{GeO}_2-\text{P}_2\text{O}_5$. *Solid State Ionics* **104**, 191–194 (1997).
- [41] Aono, H., Sugimoto, E., Sadaoka, Y., Imanaka, N. & Adachi, G. Ionic Conductivity of Solid Electrolytes Based on Lithium Titanium Phosphate. *J. Electrochem. Soc.* **137**, 1023–1027 (1990).
- [42] Perthuis, H. & Colomban, P. Sol-gel routes leading to nasicon ceramics. *Ceram. Int.* **12**, 39–52 (1986).
- [43] Boilot, J. P., Salanié, J. P., Desplanches, G. & Le Potier, D. Phase transformation in $\text{Na}_{1+x}\text{Si}_x\text{Zr}_2\text{P}_{3-x}\text{O}_{12}$ compounds. *Mater. Res. Bull.* **14**, 1469–1477 (1979).
- [44] Gordon, R. S., Miller, G. R., McEntire, B. J., Beck, E. D. & Rasmussen, J. R. Fabrication and characterization of Nasicon electrolytes. *Solid State Ionics* **3–4**, 243–248 (1981).
- [45] Tuller, H. L. *Solid State Batteries: Materials Design and Optimization*. Springer Science+Business Media, Llc (Springer Science & Business Media, 1994).
- [46] Bukun, N. G. Superionic transitions in NASICON-type solid electrolytes. *Ionics (Kiel)*. **2**, 63–68 (1996).
- [47] Hueso, K. B., Armand, M. & Rojo, T. High temperature sodium batteries: Status, challenges and future trends. *Energy Environ. Sci.* **6**, 734–749 (2013).
- [48] Jolley, A. G., Cohn, G., Hitz, G. T. & Wachsman, E. D. Improving the ionic conductivity of NASICON through aliovalent cation substitution of $\text{Na}_3\text{Zr}_2\text{Si}_2\text{PO}_{12}$. *Ionics (Kiel)*. **21**, 3031–3038 (2015).
- [49] Li, D. *et al.* A designer fast Li-ion conductor $\text{Li}_6.25\text{PS}_5.25\text{Cl}_{0.75}$ and its contribution to the polyethylene oxide based electrolyte. *Appl. Surf. Sci.* **493**, 1326–1333 (2019).
- [50] Long, L., Wang, S., Xiao, M. & Meng, Y. Polymer electrolytes for lithium polymer batteries. *J. Mater. Chem. A* **4**, 10038–10039 (2016).
- [51] Teragawa, S., Aso, K., Tadanaga, K., Hayashi, A. & Tatsumisago, M. Preparation of $\text{Li}_2\text{S}-\text{P}_2\text{S}_5$ solid electrolyte from N-methylformamide solution and application for all-solid-state lithium battery. *J. Power Sources* **248**, 939–942 (2014).
- [52] Kanno, R. & Murayama, M. Lithium Ionic Conductor Thio-LISICON: The $\text{Li}_2\text{S}-\text{GeS}_2-\text{P}_2\text{S}_5$ System. *J. Electrochem. Soc.* **148**, A742 (2001).

-
- [53] Mizuno, F., Hayashi, A., Tadanaga, K. & Tatsumisago, M. New, highly ion-conductive crystals precipitated from Li_2S - P_2S_5 glasses. *Adv. Mater.* **17**, 918–921 (2005).
- [54] Kamaya, N. *et al.* A lithium superionic conductor. *Nat. Mater.* **10**, 682–686 (2011).
- [55] Kato, Y. *et al.* High-power all-solid-state batteries using sulfide superionic conductors. *Nat. Energy* **1**, 1–7 (2016).
- [56] Deiseroth, H. J. *et al.* $\text{Li}_6\text{PS}_5\text{X}$: A class of crystalline Li-rich solids with an unusually high Li^+ mobility. *Angew. Chemie - Int. Ed.* **47**, 755–758 (2008).
- [57] Muramatsu, H., Hayashi, A., Ohtomo, T., Hama, S. & Tatsumisago, M. Structural change of Li_2S - P_2S_5 sulfide solid electrolytes in the atmosphere. *Solid State Ionics* **182**, 116–119 (2011).
- [58] Morimoto, H., Yamashita, H., Tatsumisago, M. & Minami, T. Mechanochemical synthesis of new amorphous materials of $60\text{Li}_2\text{S}\cdot 40\text{SiS}_2$ with high lithium ion conductivity. *J. Am. Ceram. Soc.* **54**, 1352–1354 (1999).
- [59] Kennedy, J. H. & Zhang, Z. Further Characterization of SiS_2 - Li_2S Glasses Doped with Lithium Halide. *J. Electrochem. Soc.* **135**, 859–862 (1988).
- [60] Kennedy, J. & Zhang, Z. Improved stability for the SiS_2 - P_2S_5 - Li_2S - LiI glass system. *Solid State Ionics* **30**, 726–728 (1988).
- [61] Mercier, R., Malugani, J.P., Fahys, B. & Robert, G. Superionic conduction in Li_2S - P_2S_5 - LiI -glasses. *Solid State Ionics* **5**, 663–666 (1981).
- [62] Ribes, M., Barrau, B. & Souquet, J. L. Sulfide glasses: Glass forming region, structure and ionic conduction of glasses in Na_2 - XS_2 ($\text{X} = \text{Si}$; Ge), Na_2S - P_2S_5 and Li_2S - GeS_2 systems. *J. Non. Cryst. Solids* **38–39**, 271–276 (1980).
- [63] Zhang, Z. & Kennedy, J. H. Synthesis and characterization of the B_2S_3 - Li_2S , the P_2S_5 - Li_2S and the B_2S_3 - P_2S_5 - Li_2S glass systems. *Solid State Ionics* **38**, 217–224 (1990).
- [64] Shin, B. R. *et al.* Comparative study of TiS_2/Li -In all-solid-state lithium batteries using glass-ceramic Li_3PS_4 and $\text{Li}_{10}\text{GeP}_2\text{S}_{12}$ solid electrolytes. *Electrochim. Acta* **146**, 395–402 (2014).
- [65] Bron, P. *et al.* $\text{Li}_{10}\text{SnP}_2\text{S}_{12}$: An affordable lithium superionic conductor. *J. Am. Chem. Soc.* **135**, 15694–15697 (2013).
- [66] Whiteley, J. M., Woo, J. H., Hu, E., Nam, K.-W. & Lee, S.-H. Empowering the lithium metal battery through a silicon-based superionic conductor. *J. Electrochem. Soc.* **161**, A1812–A1817 (2014).

-
- [67] Wang, S. *et al.* High-conductivity argyrodite $\text{Li}_6\text{PS}_5\text{Cl}$ solid electrolytes prepared via optimized sintering processes for all-solid-state lithium-sulfur batteries. *ACS Appl. Mater. Interfaces* **10**, 42279–42285 (2018).
- [68] Yu, C. *et al.* Unravelling Li-ion transport from picoseconds to seconds: bulk versus interfaces in an argyrodite $\text{Li}_6\text{PS}_5\text{Cl}$ - Li_2S all-solid-state Li-ion battery. *J. Am. Chem. Soc.* **138**, 11192–11201 (2016).
- [69] Rao, R. P., Sharma, N., Peterson, V. K. & Adams, S. Formation and conductivity studies of lithium argyrodite solid electrolytes using in-situ neutron diffraction. *Solid State Ionics* **230**, 72–76 (2013).
- [70] Chen, M., Yin, X., Reddy, M. V. & Adams, S. All-solid-state $\text{MoS}_2/\text{Li}_6\text{PS}_5\text{Br}/\text{In-Li}$ batteries as a novel type of Li/S battery. *J. Mater. Chem. A* **3**, 10698–10702 (2015).
- [71] Kim, D. H. *et al.* Infiltration of solution-processable solid electrolytes into conventional Li-Ion-battery electrodes for all-solid-state Li-ion batteries. *Nano Lett.* **17**, 3013–3020 (2017).
- [72] Auvergniot, J. *et al.* Interface stability of argyrodite $\text{Li}_6\text{PS}_5\text{Cl}$ toward LiCoO_2 , $\text{LiNi}_{1/3}\text{Co}_{1/3}\text{Mn}_{1/3}\text{O}_2$, and LiMn_2O_4 in bulk all-solid-state batteries. *Chem. Mater.* **29**, 3883–3890 (2017).
- [73] Evain, M., Gaudin, E., Boucher, F., Petricek, V. & Taulelle, F. Structures and Phase Transitions of the A_7PSe_6 (A = Ag, Cu) Argyrodite-Type Ionic Conductors. I. Ag_7PSe_6 . *Acta Crystallogr. Sect. B Struct. Sci.* **54**, 376–383 (1998).
- [74] Kong, S. T. *et al.* Structural characterisation of the Li argyrodites Li_7PS_6 and Li_7PSe_6 and their solid Solutions: Quantification of Site Preferences by MAS-NMR Spectroscopy. *Chem. - Eur. J.* **16**, 5138–5147 (2010).
- [75] Kraft, M. A. *et al.* Influence of Lattice Polarizability on the Ionic Conductivity in the Lithium Superionic Argyrodites $\text{Li}_6\text{PS}_5\text{X}$ (X = Cl, Br, I). *J. Am. Chem. Soc.* **139**, 10909–10918 (2017).
- [76] De Klerk, N. J. J., Rosłoń, I. & Wagemaker, M. Diffusion Mechanism of Li Argyrodite Solid Electrolytes for Li-Ion Batteries and Prediction of Optimized Halogen Doping: The Effect of Li Vacancies, Halogens, and Halogen Disorder. *Chem. Mater.* **28**, 7955–7963 (2016).
- [77] Deng, Z., Zhu, Z., Chu, I. H. & Ong, S. P. Data-driven first-principles methods for the study and design of alkali superionic conductors. *Chem. Mater.* **29**, 281–288 (2017).
- [78] He, X., Zhu, Y. & Mo, Y. Origin of fast ion diffusion in super-ionic conductors. *Nat. Commun.* **8**, 1–7 (2017).

-
- [79] Park, K. H. *et al.* Solution-Processable Glass LiI - Li₄SnS₄ Superionic Conductors for All-Solid-State Li-Ion Batteries. *Adv. Mater.* **28**, 1874–1883 (2016).
- [80] Yu, C. *et al.* Facile Synthesis toward the Optimal Structure-Conductivity Characteristics of the Argyrodite Li₆PS₅Cl Solid-State Electrolyte. *ACS Appl. Mater. Interfaces* **10**, 33296–33306 (2018).
- [81] Murphy, D. *Fundamentals of Light Microscopy and Electronic Imaging*. Wiley-Liss (Wiley Online, 2012).
- [82] Leong, S. S., Ng, W. M., Lim, J. K. & Yeap, S. P. *Handbook of Materials Characterization*. Chapter authors: Akhtar K., Khan S.A., Khan S.B., Asiri A.M. *Scanning Electron Microscopy: Principle and Applications in Nanomaterials Characterization*. (Springer, 2018).
- [83] Fields, A., Cullity, B. D. & Stock, S. R. *Elements of X-Ray Diffraction*. (Prentice-Hall, 2001).
- [84] Girolami, G. S. *X-ray Crystallography*. (University Science Books, 2016).
- [85] Pecharsky, V. & Zavalij, P. *Fundamentals of Powder Diffraction and Structural Characterization of Materials*. (Springer, 2009).
- [86] Rao, R. P. & Adams, S. Studies of lithium argyrodite solid electrolytes for all-solid-state batteries. *Phys. Status Solidi Appl. Mater. Sci.* **208**, 1804–1807 (2011).
- [87] Rayavarapu, P. R., Sharma, N., Peterson, V. K. & Adams, S. Variation in structure and Li⁺-ion migration in argyrodite-type Li₆PS₅X (X = Cl, Br, I) solid electrolytes. *J. Solid State Electrochem.* **16**, 1807–1813 (2012).
- [88] Yu, C. *et al.* Revealing the relation between the structure, Li-ion conductivity and solid-state battery performance of the argyrodite Li₆PS₅Br solid electrolyte. *J. Mater. Chem. A* **5**, 21178–21188 (2017).
- [89] Wang, S. *et al.* High-conductivity argyrodite Li₆PS₅Cl solid electrolytes prepared via optimized sintering processes for all-solid-state lithium-sulfur batteries. *ACS Appl. Mater. Interfaces* **10**, 42279–42285 (2018).
- [90] Gautam, A. *et al.* Rapid Crystallization and Kinetic Freezing of Site-Disorder in the Lithium Superionic Argyrodite Li₆PS₅Br. *Chem. Mater.* **31**, 10178–10185 (2019).
- [91] Montes, J. M., Cuevas, F. G. & Cintas, J. Porosity effect on the electrical conductivity of sintered powder compacts. *Appl. Phys. A Mater. Sci. Process.* **92**, 375–380 (2008).
- [92] Kraft, M. A. *et al.* Inducing High Ionic Conductivity in the Lithium Superionic Argyrodites Li_{6+x}P_{1-x}Ge_xS₅I for All-Solid-State Batteries. *J. Am. Chem. Soc.* **140**, 16330–16339 (2018).

-
- [93] Yubuchi, S. *et al.* Preparation of high lithium-ion conducting $\text{Li}_6\text{PS}_5\text{Cl}$ solid electrolyte from ethanol solution for all-solid-state lithium batteries. *J. Power Sources* **293**, 941–945 (2015).
- [94] Rosero-Navarro, N. C., Miura, A. & Tadanaga, K. Preparation of lithium ion conductive $\text{Li}_6\text{PS}_5\text{Cl}$ solid electrolyte from solution for the fabrication of composite cathode of all-solid-state lithium battery. *J. Sol-Gel Sci. Technol.* **89**, 303–309 (2019).
- [95] Chida, S. *et al.* Liquid-phase synthesis of $\text{Li}_6\text{PS}_5\text{Br}$ using ultrasonication and application to cathode composite electrodes in all-solid-state batteries. *Ceram. Int.* **44**, 742–746 (2018).
- [96] Yubuchi, S. *et al.* An argyrodite sulfide-based superionic conductor synthesized by a liquid-phase technique with tetrahydrofuran and ethanol. *J. Mater. Chem. A* **7**, 558–566 (2019).
- [97] Zhou, L. *et al.* Solvent-Engineered Design of Argyrodite $\text{Li}_6\text{PS}_5\text{X}$ (X = Cl, Br, I) Solid Electrolytes with High Ionic Conductivity. *ACS Energy Lett.* **4**, 265–270 (2019).
- [98] Kuhn, A., Duppel, V. & Lotsch, B. V. Tetragonal $\text{Li}_{10}\text{GeP}_2\text{S}_{12}$ and Li_7GePS_8 - exploring the Li ion dynamics in LGPS Li electrolytes. *Energy Environ. Sci.* **6**, 3548–3552 (2013).
- [99] Kaus, M. *et al.* Local Structures and Li Ion Dynamics in a $\text{Li}_{10}\text{SnP}_2\text{S}_{12}$ -Based Composite Observed by Multinuclear Solid-State NMR Spectroscopy. *J. Phys. Chem. C* **121**, 23370–23376 (2017).
- [100] Griffith, K. J., Wiaderek, K. M., Cibir, G., Marbella, L. E. & Grey, C. P. Niobium tungsten oxides for high-rate lithium-ion energy storage. *Nature* **559**, 556–563 (2018).
- [101] Dorai, A. *et al.* Diffusion coefficient of lithium ions in garnet-type $\text{Li}_{6.5}\text{La}_3\text{Zr}_{1.5}\text{Ta}_{0.5}\text{O}_{12}$ single crystal probed by ^7Li pulsed field gradient-NMR spectroscopy. *Solid State Ionics* **327**, 18–26 (2018).
- [102] Chu, I. H. *et al.* Room-Temperature All-solid-state Rechargeable Sodium-ion Batteries with a Cl-doped Na_3PS_4 Superionic Conductor. *Sci. Rep.* **6**, 1–10 (2016).
- [103] Brug, G. J., van den Eeden, A. L. G., Sluyters-Rehbach, M. & Sluyters, J. H. The analysis of electrode impedances complicated by the presence of a constant phase element. *J. Electroanal. Chem.* **176**, 275–295 (1984).
- [104] Schlenker, R. *et al.* Structure and Diffusion Pathways in $\text{Li}_6\text{PS}_5\text{Cl}$ Argyrodite from Neutron Diffraction, Pair-Distribution Function Analysis, and NMR. *Chem. Mater.* **32**, 8420–8430 (2020).

-
- [105] Wenzel, S., Sedlmaier, S. J., Dietrich, C., Zeier, W. G. & Janek, J. Interfacial reactivity and interphase growth of argyrodite solid electrolytes at lithium metal electrodes. *Solid State Ionics* **318**, 102–112 (2018).
- [106] Kuhn, A. *et al.* A new ultrafast superionic Li-conductor: Ion dynamics in $\text{Li}_{11}\text{Si}_2\text{PS}_{12}$ and comparison with other tetragonal LGPS-type electrolytes. *Phys. Chem. Chem. Phys.* **16**, 14669–14674 (2014).
- [107] Abu-Lebdeh, Y. & Davidson, I. *Nanotechnology for Lithium-Ion Batteries*. (Springer, 2013).
- [108] Ganapathy, S., Yu, C., Van Eck, E. R. H. & Wagemaker, M. Peeking across Grain Boundaries in a Solid-State Ionic Conductor. *ACS Energy Lett.* **4**, 1092–1097 (2019).
- [109] Adeli, P. *et al.* Boosting Solid-State Diffusivity and Conductivity in Lithium Superionic Argyrodites by Halide Substitution. *Angew. Chemie - Int. Ed.* **58**, 8681–8686 (2019).
- [110] Adeli, P., Bazak, J. D., Huq, A., Goward, G. R. & Nazar, L. F. Influence of Aliovalent Cation Substitution and Mechanical Compression on Li-Ion Conductivity and Diffusivity in Argyrodite Solid Electrolytes. *Chem. Mater.* **33**, 146–157 (2021).
- [111] Krauskopf, T. *et al.* Comparing the Descriptors for Investigating the Influence of Lattice Dynamics on Ionic Transport Using the Superionic Conductor $\text{Na}_3\text{PS}_{4-x}\text{Se}_x$. *J. Am. Chem. Soc.* **140**, 14464–14473 (2018).
- [112] Bernges, T., Culver, S. P., Minafra, N., Koerver, R. & Zeier, W. G. Competing Structural Influences in the Li Superionic Conducting Argyrodites $\text{Li}_6\text{PS}_{5-x}\text{Se}_x\text{Br}$ ($0 \leq x \leq 1$) upon Se Substitution. *Inorg. Chem.* **57**, 13920–13928 (2018).
- [113] Wang, Z. & Shao, G. Theoretical design of solid electrolytes with superb ionic conductivity: Alloying effect on Li^+ transportation in cubic $\text{Li}_6\text{PA}_5\text{X}$ chalcogenides. *J. Mater. Chem. A* **5**, 21846–21857 (2017).
- [114] Schlem, R., Ghidui, M., Culver, S. P., Hansen, A. L. & Zeier, W. G. Changing the Static and Dynamic Lattice Effects for the Improvement of the Ionic Transport Properties within the Argyrodite $\text{Li}_6\text{PS}_{5-x}\text{Se}_x\text{I}$. *ACS Appl. Energy Mater.* **3**, 9–18 (2020).
- [115] Wu, Z. *et al.* Novel SeS_2 doped $\text{Li}_2\text{S-P}_2\text{S}_5$ solid electrolyte with high ionic conductivity for all-solid-state lithium sulfur batteries. *Chem. Eng. J.* **380**, 122419 (2020).
- [116] Song, S., Yan, Z., Wu, F., Zhang, X. & Xiang, Y. Electrochemical stability and ionic conductivity of solid electrolytes based on $\text{Li}_{10}\text{GeP}_2\text{S}_{12-x}\text{A}_x$ ($\text{A} = \text{O}, \text{Se}$, $x = 0, 0.2, 0.4, 0.6, 0.8, 1$). *IOP Conf. Ser. Earth Environ. Sci.* **461**, 1–8 (2020).

-
- [117] Yang, K., Dong, J., Zhang, L., Li, Y. & Wang, L. Dual Doping: An Effective Method to Enhance the Electrochemical Properties of $\text{Li}_{10}\text{GeP}_2\text{S}_{12}$ -Based Solid Electrolytes. *J. Am. Ceram. Soc.* **98**, 3831–3835 (2015).
- [118] Zhang, L. *et al.* Na_3PSe_4 : A Novel Chalcogenide Solid Electrolyte with High Ionic Conductivity. *Adv. Energy Mater.* **5**, 2–6 (2015).
- [119] Bo, S. H., Wang, Y., Kim, J. C., Richards, W. D. & Ceder, G. Computational and Experimental Investigations of Na-Ion Conduction in Cubic Na_3PSe_4 . *Chem. Mater.* **28**, 252–258 (2016).
- [120] Duchardt, M. *et al.* Superior conductor $\text{Na}_{11.1}\text{Sn}_{2.1}\text{P}_{0.9}\text{Se}_{12}$: Lowering the activation barrier of Na^+ conduction in quaternary 1-4-5-6 electrolytes. *Chem. Mater.* **30**, 4134–4139 (2018).
- [121] Krauskopf, T., Pompe, C., Kraft, M. A. & Zeier, W. G. Influence of Lattice Dynamics on Na^+ Transport in the Solid Electrolyte $\text{Na}_3\text{PS}_{4-x}\text{Se}_x$. *Chem. Mater.* **29**, 8859–8869 (2017).
- [122] Bo, S. H., Wang, Y. & Ceder, G. Structural and Na-ion conduction characteristics of $\text{Na}_3\text{PS}_x\text{Se}_{4-x}$. *J. Mater. Chem. A* **4**, 9044–9053 (2016).
- [123] Wang, N. *et al.* Improvement in ion transport in Na_3PSe_4 – Na_3SbSe_4 by Sb substitution. *J. Mater. Sci.* **53**, 1987–1994 (2018).
- [124] Wan, H. *et al.* Grain-boundary-resistance-less $\text{Na}_3\text{SbS}_{4-x}\text{Se}_x$ solid electrolytes for all-solid-state sodium batteries. *Nano Energy* **66**, 104109 (2019).
- [125] Brice, J. F. *C. R. Seances Acad. Sci. Ser. C* **283**, 581–584 (1976).
- [126] Epp, V., Gun, O., Deiseroth, H. J. & Wilkening, M. Long-range Li^+ dynamics in the lithium argyrodite Li_7PSe_6 as probed by rotating-frame spin-lattice relaxation NMR. *Phys. Chem. Chem. Phys.* **15**, 7123–7132 (2013).
- [127] Harm, S. *et al.* Lesson learned from NMR: characterization and ionic conductivity of LGPS-like Li_7SiPS_8 . *Chem. Mater.* **31**, 1280–1288 (2019).
- [128] Morgan, B. J. Mechanistic origin of superionic lithium diffusion in anion-disordered $\text{Li}_6\text{PS}_5\text{X}$ argyrodites. *Chem. Mater.* **33**, 2004–2018 (2021).
- [129] Schneider, H. *et al.* Stabilization of Highly Conductive Lithium Argyrodites by Means of Lithium Substitution: The Case of $\text{Li}_6\text{Fe}_{0.5}\text{PS}_6$. *ChemistrySelect* **4**, 3351–3354 (2019).
- [130] Zhang, Z. *et al.* Enhancing ionic conductivity of solid electrolyte by lithium substitution in halogenated Li-Argyrodite. *J. Power Sources* **450**, 227601 (2020).
- [131] Hikima, K. *et al.* High ionic conductivity of multivalent cation doped $\text{Li}_6\text{PS}_5\text{Cl}$ solid electrolytes synthesized by mechanical milling. *RSC Adv.* **10**, 22304–22310 (2020).

-
- [132] Tsujimura, T., Suzuki, N. & Aihara, Y. Samsung Inc. *Solid Electrolyte And Lithium Battery Including the Same*. United States of America, US2017/0187066 (June 29, 2017).
- [133] Yu, C., van Eijck, L., Ganapathy, S. & Wagemaker, M. Synthesis, structure and electrochemical performance of the argyrodite $\text{Li}_6\text{PS}_5\text{Cl}$ solid electrolyte for Li-ion solid state batteries. *Electrochim. Acta* **215**, 93–99 (2016).
- [134] Boulineau, S., Courty, M., Tarascon, J. M. & Viallet, V. Mechanochemical synthesis of Li-argyrodite $\text{Li}_6\text{PS}_5\text{X}$ (X = Cl, Br, I) as sulfur-based solid electrolytes for all solid state batteries application. *Solid State Ionics* **221**, 1–5 (2012).
- [135] Boulineau, S., Tarascon, J. M., Leriche, J. B. & Viallet, V. Electrochemical properties of all-solid-state lithium secondary batteries using Li-argyrodite $\text{Li}_6\text{PS}_5\text{Cl}$ as solid electrolyte. *Solid State Ionics* **242**, 45–48 (2013).
- [136] Moon, C. K. *et al.* Vacancy-Driven Na^+ Superionic Conduction in New Ca-Doped Na_3PS_4 for All-Solid-State Na-Ion Batteries. *ACS Energy Lett.* **3**, 2504–2512 (2018).
- [137] Zhou, L., Assoud, A., Zhang, Q., Wu, X. & Nazar, L. F. New Family of Argyrodite Thioantimonate Lithium Superionic Conductors. *J. Am. Chem. Soc.* **141**, 19002–19013 (2019).
- [138] Minafra, N. *et al.* Local Charge Inhomogeneity and Lithium Distribution in the Superionic Argyrodites $\text{Li}_6\text{PS}_5\text{X}$ (X = Cl, Br, I). *Inorg. Chem.* **59**, 11009–11019 (2020).
- [139] Israel Science and Technology Directory. List of Periodic Table Elements Sorted by: Abundance in Earth's Crust. <https://www.science.co.il/elements/?s=Earth> (accessed 2019-07-15).
- [140] Shin, B. R. *et al.* Comparative study of TiS_2/Li -In all-solid-state lithium batteries using glass-ceramic Li_3PS_4 and $\text{Li}_{10}\text{GeP}_2\text{S}_{12}$ solid electrolytes. *Electrochim. Acta* **146**, 395–402 (2014).
- [141] Wang, Y., Richards, W. D., Bo, S. H., Miara, L. J. & Ceder, G. Computational Prediction and Evaluation of Solid-State Sodium Superionic Conductors $\text{Na}_7\text{P}_3\text{X}_{11}$ (X = O, S, Se). *Chem. Mater.* **29**, 7475–7482 (2017).
- [142] Houtarde, D. Synthesis of Sulfide-based Solid Electrolytes for Application to All-Solid-State Lithium-Sulfur Batteries. (University of Waterloo, 2015).
- [143] Studenyak, I. P. *et al.* Synthesis and characterization of new potassium-containing argyrodite-type compounds. *Semicond. Physics, Quantum Electron. Optoelectron.* **22**, 26–33 (2019).
- [144] Chen, H. M., Maohua, C. & Adams, S. Stability and ionic mobility in argyrodite-related lithium-ion solid electrolytes. *Phys. Chem. Chem. Phys.* **17**, 16494–16506 (2015).







-
- [145] Xie, J., Sun, Y., Zhang, Z., Jia, H. Argyrodite Inspired Exploration of Sulfide Lithium/Sodium Superionic Conductors. *22nd International Conference on Solid State Ionics, PyeongChang, Korea* (2019-06).
- [146] Minami, T. Recent Progress in Superionic Conducting Glasses. *J. Non. Cryst. Solids* **95**, 107–118 (1987).
- [147] Hayashi, A., Noi, K., Sakuda, A. & Tatsumisago, M. Superionic glass-ceramic electrolytes for room-temperature rechargeable sodium batteries. *Nat. Commun.* **3**, 1–5 (2012).
- [148] Tatsumisago, M. Glassy materials based on Li_2S for all-solid-state lithium secondary batteries. *Solid State Ionics* **175**, 13–18 (2004).
- [149] Elam, J. W. & Meng, Z. *Materials for Solid State Electrolytes and Protective Electrode Coatings for Lithium Batteries*. United States of America, US2015/0364747A1 (2015).
- [150] Cao, Y., Meng, X. & Elam, J. W. Atomic Layer Deposition of $\text{Li}_x\text{Al}_y\text{S}$ Solid-State Electrolytes for Stabilizing Lithium-Metal Anodes. *ChemElectroChem* **3**, 858–863 (2016).
- [151] Ellis, B. L. & Nazar, L. F. Sodium and sodium-ion energy storage batteries. *Curr. Opin. Solid State Mater. Sci.* **16**, 168–177 (2012).
- [152] Uematsu, M. *et al.* Suspension synthesis of $\text{Na}_{3-x}\text{PS}_{4-x}\text{Cl}_x$ solid electrolytes. *J. Power Sources* **428**, 131–135 (2019).
- [153] Yu, Y. *et al.* A carbon coated NASICON structure material embedded in porous carbon enabling superior sodium storage performance: $\text{NaTi}_2(\text{PO}_4)_3$ as an example. *Nanoscale* **7**, 14723–14729 (2015).
- [154] Hueso, K. B., Armand, M. & Rojo, T. High temperature sodium batteries: Status, challenges and future trends. *Energy Environ. Sci.* **6**, 734–749 (2013).
- [155] Zhou, C., Bag, S. & Thangadurai, V. Engineering Materials for Progressive All-Solid-State Na Batteries. *ACS Energy Lett.* **3**, 2181–2198 (2018).
- [156] Wong, H. V., Evans, J. S. O., Barlow, S. & O'Hare, D. Structural characterisation of organometallic intercalates of SnSe_2 and ZrS_2 by neutron and X-ray diffraction. *J. Chem. Soc. Chem. Commun.* **20**, 1589–1591 (1993).
- [157] Coste, S. *et al.* $\text{Na}_3\text{Cr}_2\text{P}_3\text{S}_{12}$ and $\text{K}_3\text{Cr}_2\text{P}_3\text{S}_{12}$: Two new one-dimensional thiophosphate compounds with a novel structure. *J. Solid State Chem.* **162**, 195–203 (2001).
- [158] Müller, C., Jörgens, S. & Mewis, A. New Thiophosphates: The Compounds $\text{Li}_6\text{Ln}_3(\text{PS}_4)_5$ (Ln: Y, Gd, Dy, Yb, Lu) und $\text{Ag}_3\text{Y}(\text{PS}_4)_2$. *Z. Anorg. Allg. Chem.* **633**, 1633–1638 (2007).

[159] Deng, Z., Zhu, Z., Chu, I. H. & Ong, S. P. Data-driven first-principles methods for the study and design of alkali superionic conductors. *Chem. Mater.* **29**, 281–288 (2017).

Appendix A - Data Use Permissions

← Reply | ▾ Delete Junk Block ...

Data Use Permissions

 David Bazak <bazakjd@mcmaster.ca>      ...
Wed 2020-03-04 11:13 PM
To: Parvin Adeli

To whom it may concern,

I, J. David Bazak, do hereby grant Parvin Adeli full permission to use data that I acquired for the completion of her doctoral dissertation, free of any and all restrictions.

Sincerely,

--
J. David Bazak
PhD Candidate
McMaster University
Department of Chemistry/MARC
A.N. Bourns Science Building, Room 264
Hamilton, ON, Canada, L8S 4M1

[Reply](#) | [Forward](#)

Appendix B - Supplementary Information for Chapter 5

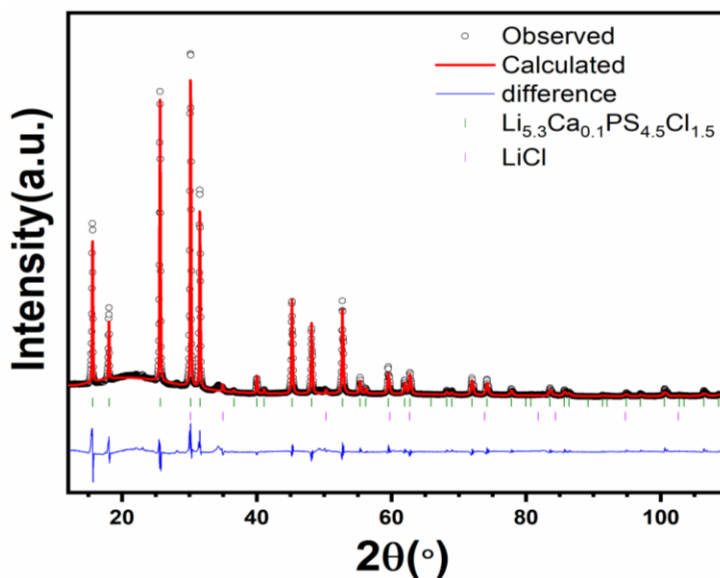


Figure B.1 Rietveld refinement of XRD pattern of $\text{Li}_{5.3}\text{Ca}_{0.1}\text{PS}_{4.5}\text{Cl}_{1.5}$, GOF = 1.51, Rwp = 8.88.

Table B.1 Atomic coordinates, occupation factor and isotropic displacement parameters of the targeted $\text{Li}_{5.3}\text{Ca}_{0.1}\text{PS}_{4.5}\text{Cl}_{1.5}$ obtained from Rietveld refinement against X-ray diffraction data (space group $F\bar{4}3m$) $a = 9.8132(1)$ Å, and volume = $945.02(4)$ Å³. Since X-rays are not able to resolve the Li occupancy, the Occupancies for the $48h$ site were fixed to the nominal values and occupancies for the $4a$ site were fixed to the values obtained from NDP of $\text{Li}_{5.5}\text{PS}_{4.5}\text{Cl}_{1.5}$.

Atom	Wyckoff Site	x	y	z	SOF	$U_{\text{iso}}(\text{Å}^2)$
Li	$48h$	0.329(1)	-0.001(2)	0.671(1)	0.440	0.114(9)
Ca	$48h$	0.329(1)	-0.001(2)	0.671(1)	0.010	0.114(9)
Cl1	$4a$	0	0	0	0.615	0.043(2)
S1	$4a$	0	0	0	0.385	0.043(2)
Cl2	$4c$	1/4	1/4	1/4	0.83(12)	0.040(2)
S2	$4c$	1/4	1/4	1/4	0.17(12)	0.040(2)
P1	$4b$	0	0	0.5	1	0.038(1)
S3	$16e$	0.1211(2)	-0.1211(2)	0.6211(2)	1	0.063

Appendix C - Supplementary Information for Chapter 6

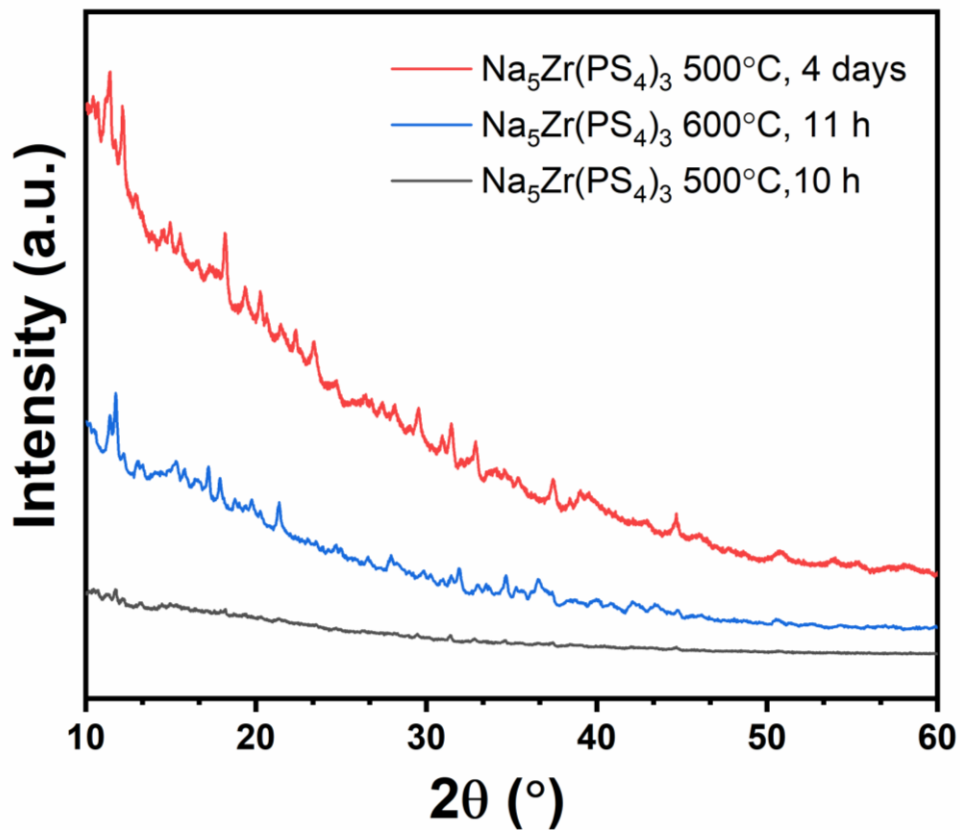


Figure C.1 Comparison of XRD patterns of Na₅Zr(PS₄)₃ for three different heat treatment procedures (500°C, hold 10 h; 500°C, hold 4 days and 600°C, hold 11 h).